

Snow Avalanche Research Programme SIP-6

**Ryggfonn. Full scale avalanche test site and
the effect of the catching dam**

581200-35

28 February 2002

Client: Norwegian Geotechnical Institute

Contact person: Karstein Lied
Contract reference: SIP-6

For the Norwegian Geotechnical Institute

Project Manager:

A handwritten signature in blue ink, appearing to read 'Karstein Lied', is written over the printed name.

Karstein Lied

Report prepared by:

Karstein Lied, Arne Moe,
Kristen Kristensen, Dieter Issler

Summary

The effect of the 16 m high retaining dam in Ryggfonn has been analysed by using data from 12 dry snow avalanches. Except for one avalanche, which was stopped by the dam, all of these avalanches overtopped it and ran beyond the dam. Avalanche speeds were inferred from the arrival times at sensors 320 m and 230 m upstream of the dam. Based on these observations, the avalanche speed at the site of the dam and the run-out were simulated with the NIS model and compared to the observed run-out. The run-out of the observed avalanches is closely correlated to the avalanche velocity. The volume of the avalanches has a weaker correlation with the run-out.

Analysis of the deposit profiles, although fraught with large uncertainties, suggests that an extra 0 % to 70% of the total avalanche mass were stopped upstream of the dam thanks to its presence. Low values result for very slow and very fast avalanches and if the free board was reduced by preceding avalanches.

The simulations by the NIS model indicate that the average energy loss from the base of the dam to the top is 23% with a freeboard of 16 m. Calculations based on comparisons between the observed run-out and the simulated velocity head $v^2/(2g)$ at the upstream base of the dam indicate a loss of 31% induced by the dam, which corresponds to $\lambda = 1.46$ in the expression $h = v^2/(2g \lambda)$.

From an analysis of the sources of energy dissipation in avalanche impact on a dam we draw tentative conclusions concerning avalanches that overrun a dam: (i) The retention capacity of a dam is mostly determined by the difference between the inclination angle of shear planes and the deflection angle at the dam. It may become very low if the dam is not as steep as possible on its upstream side. (ii) The dam mitigates the effect of overrunning avalanches directly through increased friction at its foot and indirectly by stopping snow predominantly from the more energetic avalanche head.

Application of methods from supersonic gas dynamics to avalanche flow over dams is briefly discussed. Simple considerations lead to interesting results, but the applicability of the basic principles to flowing snow needs to be established experimentally as well as theoretically.



Contents

1	INTRODUCTION	4
2	THE CATCHING DAM.....	8
	2.1 Tradition design criteria for catching dams	8
	2.2 The NIS model	11
	2.3 The simulations with the NIS model	15
3	AVALANCHES ANALYSED IN THE PRESENT STUDY.....	17
	3.1 Selection criteria.....	17
	3.2 Properties of analyzed avalanches.....	18
	3.3 Spread-out ratio	21
	3.4 Compression of the avalanche snow.....	22
4	RESULTS OF THE SIMULATIONS BY THE NIS MODEL.....	22
5	TRANSFORMING RUN-OUT DISTANCE INTO LACKING DAM HEIGHT	26
	5.1 Description of the approach	27
	5.2 Dry friction dissipation of energy in the bend.....	29
	5.3 Overrun length.....	29
	5.4 Results and discussion	31
6	THEORETICAL CONSIDERATIONS ON DAM EFFECTIVENESS ..	33
	6.1 Mitigating effect of an overflowed dam	33
	6.2 Analysis of dam-induced avalanche mass loss from the deposition profiles	36
	6.3 Scaling behaviour	38
	6.4 Factors determining the deposit shape.....	39
7	CONCLUSIONS	48
8	REFERENCES	49

Review and reference document

1 INTRODUCTION

The Ryggfonn full-scale avalanche test site has been in operation since 1980. During a period of 22 years, an average of 2–3 avalanches per year has been released in the path. The Ryggfonn avalanche has a vertical drop of about 900 m and a horizontal length of 2100 m. The avalanches range in magnitude from 10,000 m³ to 500,000 m³, with maximum velocities up to 60 m/s, see Figure 1 and Figure 3. The Ryggfonn project has previously been described in several NGI reports and papers, e.g. (Kristensen, 2001; Lied, 1985, 1999; Kristensen and Larsen, 1996; Norem et al., 1982-1990).



Figure 1 The Ryggfonn avalanche



Figure 2 Dry snow avalanche hitting the dam

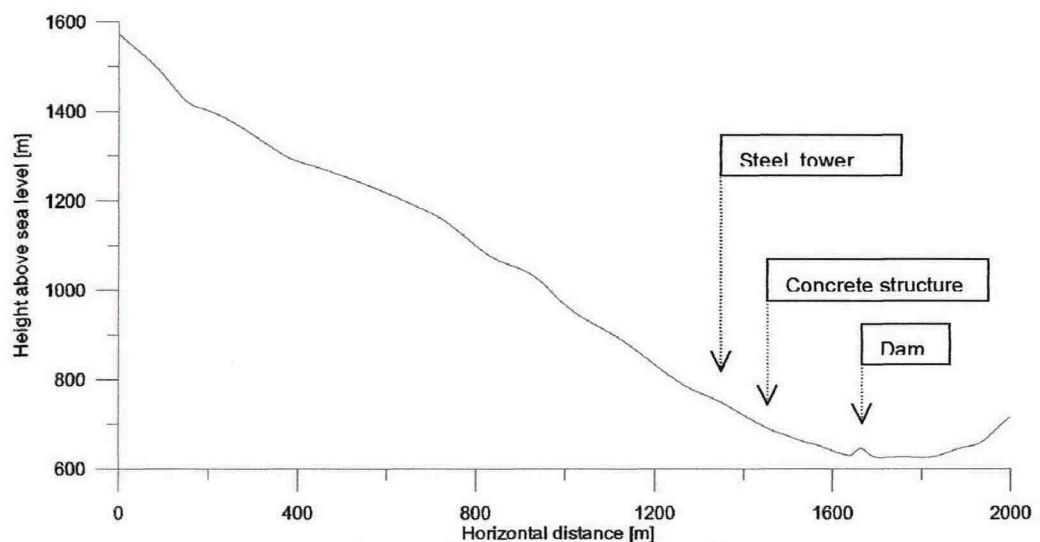


Figure 3 Terrain profile of the path with the catching dam

The avalanches are released in two ways, (1) naturally triggered, mainly because of intense snow accumulation in the starting zone, or (2) by pre-placed explosives. Dynamite is placed on the ground at the upper part of the starting zone where a cornice builds up. Three individual series, consisting of 5 charges of 25 kg of dynamite each, can be remotely triggered by radio signals.



The installations in the lower part of the avalanche path have varied from time to time, but at present they consist of the following:

- A 16–17 m high and 100 m long catching dam is located at the lower end of the path. The dam is built from stones, gravel and sand taken from the fan in the run-out zone. The width of the horizontal crown is 3 m, the inclination of the dam side towards the avalanches is 40° (1:1.2), see Figure 4.
- On the top of the dam, a 6.5 m high steel mast, instrumented with strain gauges in two sections.
- 230 m up-slope from the dam, a 4.5 m high concrete structure instrumented with three load plates, see Figure 5. The dimensions of each plate are 120 cm \times 60 cm. Three load cells with a capacity of 200 kN support each of the load plates. The total capacity of each load plate is 833 kPa.
- 320 m up-slope from the dam, a 5.5 m high cylindrical steel mast, diameter 1.3 m, reinforced with concrete and steel bars. Two load plates, identical to the load plates at the concrete structure, are mounted to the mast, with centres 2.2 m and 4.2 m above the ground respectively, see Figure 6.
- 5 geophones placed in the ground, 3 at the dam and 2 up-slope of the dam at a distance of 18 and 65 m.
- An instrument shelter near the run-out area with recording equipment. The data acquisition system has been changed twice during these years. Since 1998 the system consists of an IOTech Logbook with a strain gauge module DBK43A and a geophone module. The instruments record the avalanche passage continuously. The monitoring system is remotely controlled from NGI via ISDN telephone line.



Figure 4 *The catching dam with the steel mast on top*



Figure 5 *The concrete structure with load plates*



Figure 6 The steel mast

2 THE CATCHING DAM

2.1 Tradition design criteria for catching dams

Catching dams are widely used to stop avalanches for the purpose of protecting different kinds of infrastructure, and they are one of the most common constructions for avalanche defence works in Norway. Nevertheless, there exists no comprehensive and validated theory that describes how catching dams work, and in what way avalanche speed, volume and density influence the ascending height as the avalanche moves upward along the dam side.

The large catching dam is what sets Ryggfonn apart from other avalanche dynamics test sites. With this infrastructure, there is the potential to obtain detailed information on the interaction of large avalanches with a full-size catching dam. It should be noted, however, that comprehensive measurements of the relevant avalanche processes (such as formation of shear bands and energy dissipation due to snow compression) are difficult and costly: At the dam, flow depths may be above 10 m, velocities may exceed 40 m/s, and the relevant parameters change over very short distances. Furthermore, the

presence of the dam precludes measurements of the run-out behaviour of an undisturbed avalanche. The discussion below will show that the effectiveness of the dam can be assessed only indirectly.

In designing catching dams it is most important to make them high enough, so avalanches will not over-top them. This is especially true if the dams are built to protect housing areas, where the consequences of an over-topping avalanche may be disastrous.

Catching dams are usually built of loose deposits such as gravel, sand and rocks. The inclination of the sides of the dam is usually set as steep as the stability of the dam allows. In addition, a steep dam side is thought to be more effective than a gentle dam side, as the avalanche loses more energy in the collision with a steep dam. As the height of the dam increases, the volume increases considerably. For a dam with inclination 1:1.5 on both sides, a 10 m high dam has a volume of 150 m³ per length meter, whereas the volume of a 20 m high dam is 600 m³ per length meter. Because of rapidly increasing volume with height, the construction costs also increase rapidly with increasing height.

For both these reasons it is important to calculate the necessary dam height as accurately as possible, the dam must be sufficiently high to prevent over-topping by the avalanche, but on the other hand an unnecessarily high dam will be uneconomic.

One simple way to estimate the possible ascending height of an avalanche is to use the relation between the kinetic and the potential energy:

$$\frac{mv^2}{2} = mgh \quad (1)$$

from where the commonly used expression is derived:

$$h = \frac{v^2}{2g} \quad (2)$$

where:

v = avalanche velocity at the foot of the dam

m = avalanche mass

h = avalanche ascending height

g = constant of gravity

The main scope of the present paper is to analyse the full-scale tests in Ryggfonn with a view towards developing design criteria for the height of the catching dam based on avalanche velocity. From the tests it is clear that nearly all the observed dry avalanches have run over the dam. The important question arises: Is it possible to infer the maximum ascending height from the overrun

lengths, and based on this, to calculate the dam height necessary for stopping the avalanche?

Assume first a situation without any dam. Denoting the horizontal run-out length by l and assuming that the reduction of the velocity is caused by dry friction only, one has:

$$\frac{mv^2}{2} = mgl(\mu + \tan \alpha) \quad (3)$$

where l is the horizontal distance travelled, μ is the effective coefficient of dry friction, and α is the terrain inclination, with positive α indicating an ascending slope.

Combining (1) and (3) gives

$$h = l(\mu + \tan \alpha) \quad (4)$$

This method of calculation is clearly a simplification of what goes on as an avalanche interacts with a catching dam. In reality, friction consists not only of dry friction, but also of a velocity dependent component. The effective friction coefficient entering (4) refers to the run-out zone and may differ significantly from the friction coefficient in the track, and one also has to expect considerable variation from one site to another. Furthermore, this method disregards the friction along the dam side and the sideways spreading of the avalanche, treating the avalanche as a mass point. How the different parts of the avalanche affect each other and how the gradual build-up of avalanche debris may alter the ascending height is also neglected.

How can the presently available data from Ryggfonn be used for assessing the validity of (4) and for improving on it? One is confronted with two serious difficulties:

- The avalanche velocity just in front of the dam is not known. The only generally available velocity information is the time lag between front arrival at the tower and at the concrete structure. In some of the cases, the strain measurements at the mast on the dam also allow to infer the average front velocity between the concrete structure and the dam, but this signal is often masked by the effects of the powder snow cloud arriving ahead of the dense core.
- The dam significantly influences the recorded run-out length; there are no measurements of the undisturbed run-out length entering (4).

In this paper, an attempt is made to circumvent these difficulties by applying a dynamical model, the NIS model, that is described in the following section.

2.2 The NIS model

In the NIS model (Norem et al., 1987, 1989) the avalanche mass is modelled as a non-linear visco-elastic continuum. The model is based on the following variable parameters: Avalanche flow height, avalanche length, dry friction parameter, viscosity, and viscoelasticity.

The mathematical deformable-body model describes a quasi two-dimensional, non-steady shear flow of varying height with zero slip velocity (Harbitz, 1998). The shear flow moves along an arbitrary path, the curvature of which generates centrifugal forces that increase or diminish the friction forces. The constitutive relations comprise the viscosity and visco-elasticity of a CEF fluid (Criminale et al., 1958), combined with plasticity for a cohesive material, yield (as depicted in Figure 7) for the normal stresses σ_x and σ_y parallel and normal to the slope respectively, and for the shear stress τ_{xy} :

$$\sigma_x = p_e + p_u - \rho(v_1 - v_2) \left(\frac{\partial v_x(y)}{\partial y} \right)^r \quad (5)$$

$$\sigma_y = p_e + p_u + \rho v_2 \left(\frac{\partial v_x(y)}{\partial y} \right)^r \quad (6)$$

$$\tau_{xy} = a + p_e \tan \phi + \rho m \left(\frac{\partial v_x(y)}{\partial y} \right)^r \quad (7)$$

where p_e is the effective pressure (all normal compressive stresses have a positive sign according to soil mechanics practice), p_u is the pore pressure, ρ is the average density of the flowing material, v_1 and v_2 are the normal stress viscosities, $\partial v_x(y)/\partial y$ is the shear velocity parallel to the slope at a height y above the bed, a is the cohesion, ϕ is the internal friction angle, m is the shear stress viscosity and r is an exponent preliminarily suggested equal to 2 for avalanches.

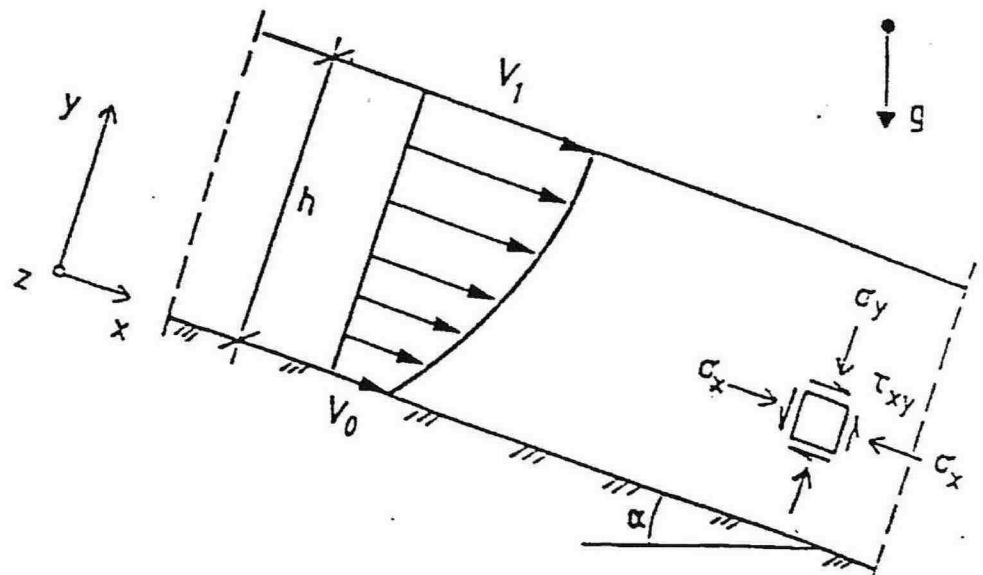


Figure 7 Definition of steady flow geometry (after Norem, Locat and Schieldrop, 1989)

As power laws represent the viscometric functions, they express flow-induced dispersive pressure and dynamic shear, as described by Bagnold (1954). The model is quasi two-dimensional as the vertical velocity profile is assumed to be identical in form to the steady shear flow profile. Cohesion induce a plug flow velocity profile, as opposed to the power-law flow profile of a non-cohesive material with zero shear stress along the upper surface.

Cohesion, upper surface shear stress and erosion are omitted in the numerical model. The resulting partial differential equations for balance of mass and linear momentum are solved by an Eulerian finite difference mid-point scheme in space and a fourth-order Runge-Kutta procedure in time. The input path profile is interpolated with cubic splines, and centrifugal forces resulting from path curvature in the vertical plane are taken into account, leading to increased or decreased friction where the slope changes.

The model has been calibrated on the run-out distances of extreme avalanche events contained in NGI's avalanche database as well as on run-out and velocity measurements from Ryggfonn. The parameter values recommended for use in consulting work are $a = 0$, $\tan \phi = 0.3-0.4$, $m = 0.001-0.01 \text{ m}^2$, $v_2 = (1.0-1.25) m$, $v_1 = 10 v_2$. As is exemplified by the Ryggfonn event of February 2000, more extreme values, especially for $\tan \phi$, may be needed occasionally to reproduce the run-out distances of very strongly fluidised avalanches. However, in such cases the distinction between the dense-flow part and the saltation layer becomes virtually impossible.

In Section 5, effective dry-friction parameters are obtained from the observed



run-out distance and the simulated velocities just after the avalanche has cleared the dam. It is instructive to analyse the constitutive equations of the NIS model, given above, for a better understanding of the relationship between the model parameters and this effective dry-friction parameter. In the following, we will assume vanishing pore pressure, $p_u = 0$, and cohesion (yield strength), $a = 0$, and hydrostatic pressure distribution. Another important simplification—always made in the NIS model—is that the velocity profile at any given instant is the one obtained in a steady-state flow with the same (local) flow velocity and flow height. In this situation, the normal stress in the y -direction is $\sigma_y(y) = -\rho g(h - y) \cos \alpha$, and the shear stress is $\tau_{xy}(y) = \rho g(h - y) \sin \alpha$. The effective pressure, p_e , is the overburden pressure, σ_y , minus the dispersive pressure. Inserting this into the expression for the shear stress leads to

$$\begin{aligned} \tau_{xy}(y) &= \rho g(h - y) \cos \alpha \tan \phi + \rho(m - \nu_2 \tan \phi) \left(\frac{\partial u_x(y)}{\partial y} \right)^2 \\ &= \rho g(h - y) \sin \alpha. \end{aligned} \quad (8)$$

The shear rate can now readily be obtained and integrated in the y -direction.

With the abbreviations $\eta := y/h$ and $A := \sqrt{\frac{g}{m - b\nu_2} (\sin \alpha - \tan \phi \cos \alpha)}$, the velocity profile, the velocity at the surface (at $\eta = 1$), the height-averaged velocity, U , and the shear rate at the bottom are found to be

$$\begin{aligned} u(\eta) &= \frac{2}{3} Ah^{3/2} \left(1 - (1 - \eta)^{3/2} \right), \\ u(1) &= \frac{2}{3} Ah^{3/2}, \\ U &= \frac{3}{5} u(1), \\ \frac{\partial u}{\partial y}(0) &= A\sqrt{h} = \frac{5}{2} \cdot \frac{U}{h}. \end{aligned}$$

The bed shear stress is now easily evaluated. We compare it to the corresponding expressions for the Voellmy (Voellmy, 1955; Bartelt et al., 1999) and PCM (Perla et al., 1980) models, scaling by the avalanche mass per unit footprint area:

$$\frac{\tau_{xy}(0)}{\sigma_y(0)} = \begin{cases} \tan \phi + Fr^2 \cdot \frac{25}{4} \cdot \frac{m - v_2 \tan \phi}{h^2} & (9) \quad \text{NIS model} \\ \mu + Fr^2 \cdot \frac{g}{\xi} & (10) \quad \text{Voellmy model} \\ \mu + Fr^2 \cdot \frac{D}{M} h & (11) \quad \text{PCM model} \end{cases}$$

Here, the Froude number is defined as $Fr = U / (gh \cos \alpha)^{1/2}$; note the occurrence of h in the denominator of this definition. The first term on the right-hand side is the dry friction; it operates in the same way in all three models, even though the values chosen in avalanche hazard mapping differ somewhat. The drag terms proportional to the square of the velocity show significant differences, however: The drag is independent of the flow height in the PCM model, inversely proportional to h in the Voellmy model, and inversely proportional to the *cube* of h in the NIS model. Thus the NIS model predicts much higher velocities for deep avalanches than for shallow ones, while the PCM model gives equal results for both.

In situations where the flow depth changes little along the path, the model parameters can be chosen such that the retarding forces are nearly the same in the three models. Typical values for extreme avalanches are $\mu = 0.15$ and $M/D = 750$ m in the PCM model. If the flow height is 2 m, say, the corresponding values are $\mu = 0.15$, $\xi = 3750$ m/s² in the Voellmy model and $\tan \phi = 0.15$, $m = v_2 = 0.002$ m² in the NIS model.

However, even if corresponding values are chosen for the model parameters, differences in the simulated velocities and run-out distances are to be expected in a direct comparison of the three models. The NIS model takes into account the centrifugal contribution to the normal stress (and thus to the dry-friction force) due to slope changes. As shown in Section 5, these losses can be considerable, especially in fast avalanches. In their present implementations as computer codes, neither the Voellmy model nor the PCM model contain this effect, which can be derived from depth averaging the equations of motion (Eglit, 1983). The avalanche path is treated as a sequence of straight segments, at the corners of which the velocity changes direction without losses in the Voellmy model (Bartelt et al., 1999), whereas the PCM model reduces the speed by a factor $\cos(\Delta\alpha)$ if the path is concave at that point, with a change of slope angle $\Delta\alpha$.

Another significant difference between the models is in the treatment of forces between different parts of the avalanche. The PCM model is a pure lumped-mass model and therefore neglects these effects altogether. In applications to run-up problems, a simplified one-dimensional continuum model (leading-edge model) therefore supersedes it (Hungri and McClung, 1987; McClung and

Mears, 1995); here, the main body of the avalanche pushes the head forward. The Voellmy model in its continuum-model implementation (Bartelt et al., 1999) achieves this effect similarly by means of the so-called earth-pressure term. A functionally similar term emerges in the NIS model from vertical integration of the longitudinal normal stress, σ_x . Contrary to what the constitutive equation suggests, it turns out to be independent of the shear rate, and it does not differentiate between 'active' ($\partial u_x / \partial x > 0$) and 'passive' ($\partial u_x / \partial x < 0$) earth pressure.

In Section 5, the effective friction parameters μ_{eff} of the analysed Ryggfonn avalanche events are determined from the observed run-out distances and the simulated velocities after the avalanches have passed the dam. The expression for the retarding forces given above can be used for a rough estimate of μ_{eff} as follows. With velocities behind the dam typically in the range 20–40 m/s, flow depths of 1–1.5 m, and average slope angles of 0–20°, the Froude number averaged over the run-out distance is in the range 4–7. With the parameter ranges indicated earlier, the shear-rate dependent contribution to μ_{eff} can be as high as 0.4–0.5 for small and slow avalanches (moderate Froude number, but relatively large values of m and ν_2). In fast avalanches, the larger flow depth and low values of m and ν_2 win over the higher Froude number, resulting in a contribution to μ_{eff} as low as about 0.08. With $\tan \phi$ varying from 0.4 down to 0.15 in extreme avalanches, μ_{eff} is expected to lie in the range 0.23–0.9.

2.3 The simulations with the NIS model

In order to quantify the unmeasured dynamical properties of the avalanches, the NIS simulation model was applied. The procedure consisted of the following steps:

- Several combinations of fracture height, viscosity and dry friction were tested in the model. In these simulations, the dam was reproduced in the path profile.
- Avalanches with unrealistic simulated run-out lengths compared to the observed run-out lengths were omitted.
- The velocity measurements from the time lag from the upper mast to the concrete construction and to the top of the dam were used as the basis for the velocity calculations.
- The corresponding computed velocities at the upper mast, concrete construction, upper base of the dam, top of the dam and lower base of the dam were registered.
- The parameter sets that correspond to the observed data were used for further simulations without the dam, in which the velocities at the base of the dam and at the point of observed run-out were calculated.

In most of the simulations, several sets of parameters give a good fit to the observed data, and the average values of the simulations were used for further studies.

To examine the effect of the dam, the velocity data can be used for the following alternatives:

1. Comparison of the observed run-out (in presence of the dam) with the simulated run-out *without* dam, to find the reduction in run-out length induced by the dam. This length can be transformed into an ascending height.
2. The velocity of the simulated avalanche without dam at the run-out position of the observed avalanche is a measure of the energy loss caused by the dam. This velocity can be transformed into a potential ascending height.
3. The computed velocity at the top of the dam can be transformed into a potential ascending height.
4. Calculation of the energy loss in the NIS-simulation by comparing the velocities before the dam, at the dam and after the dam. Centrifugal forces cause a substantial increase of friction in the concave bends at the foot of the dam due to the increased normal force against the dam, and a corresponding, but smaller decrease of friction in the convex bends at the crown.

For terrain that is not too complex, which is the case for the Ryggfonn avalanche, the NIS model has been shown to compute the velocity evolution along the path to a high accuracy (Irgens 2000, Bartelt and Salm 1998). Therefore we believe that the simulations of the Ryggfonn avalanches are realistic, when they are calibrated with the help of the monitored velocities and observed run-out lengths. The simulated avalanches stop fairly close to the observed run-out when they are calibrated to match the observed velocities and time intervals. This indicates that the total energy loss caused by the dam is also of a realistic magnitude.

The model to some extent takes the 'chain effect' into account, i.e. parts of the avalanche that undergo severe retardation are pushed by the masses behind, and vice versa. Usually, when the avalanche is retarded, the cross section increases as the flow height increases.

The model is two-dimensional, and does not include the effects of lateral spreading. For the centre of the avalanche, however, this effect is probably not essential in most avalanches.

In the observed data, and the simulations with the NIS model, there exist possible errors:

- The exact time of impact of the dense core may sometimes be difficult to determine due to a gradual increase of the forces on the load cells.



- The measured time lag between the constructions may be influenced by the fact that the sensitivity of the instrumentation is different for the different constructions.
- Parts of the avalanche front may pass to the side of the constructions without hitting the transducers.
- The dam may stop the front of the avalanche, and later parts of the avalanche may trigger the sensors in the mast at the top of the dam.
- The run-out length may be difficult to determine as the deposit of the dense core sometimes gradually thins out and is mixed with snow particles from the saltation layer.
- There is no instrumentation specifically for measuring the flow height, but snow deposits on the upper mast are an indication of the flow height. They can be used to constrain the simulations, but this data is not available for all the avalanches.
- Deposition of avalanche debris up-stream of the dam and the formation of shear layers are not included.
- The freeboard observed before the event will probably not represent the correct geometry for the biggest avalanches, since they gradually will fill up the dam and pass over it with less freeboard.
- Lateral spreading is not accounted for, and the spreading varies considerably between the avalanches, as can be seen from Table 1 and the maps in Figures 20-43.
- After passing the top of the dam, the avalanche mass will partly be thrown out in the air before it hits the ground beyond the dam. In this process the energy dissipation probably is different from the simulation with the NIS model, where the avalanche follows the contours of the dam as it passes over it.

3 AVALANCHES ANALYSED IN THE PRESENT STUDY

3.1 Selection criteria

To study the effect of the dam, 12 avalanches are analysed. The criteria for selecting the avalanches are the following:

- The avalanche consisted of dry snow.
- The avalanche must have hit the dam, and either been stopped by the dam or have overtopped it.
- Data from the recording instruments were collected faultlessly.

Avalanches of dry snow.

For the design of catching dams, avalanches consisting of dry snow are most important. Dry snow avalanches move with less friction than wet avalanches,



and the speeds are generally higher. Because of lower friction and higher speeds they attain greater run-up heights than wet avalanches.

Avalanche–dam interaction

In order to be useful in this study, avalanches must either have hit the dam and have been stopped, or overtopped the dam. Most of the dry avalanches that have hit the dam have in fact overflowed it. The physical processes that occur when an avalanche hits the dam are complex. As the avalanche front hits the dam side, the avalanche loses energy, as it is led into a new direction of movement. This process goes on in three dimensions, the avalanche partly is directed uphill along the dam side, and partly sideways along the dam. Avalanche mass also builds up at the base of the dam as shear planes are created when the following part of the avalanche runs over these deposits. In addition to this redistribution of the avalanche mass, the avalanche snow is compacted due to the impact at the dam.

Data recordings

The data recordings from the avalanche events show impact forces and tension in the steel constructions versus time, on the uppermost mast 320 m above the dam, at the concrete construction 230 m above the dam, and at the mast on the dam. The most important parameter for the study of the catching dam is the velocity of the avalanche as it hits the dam. By comparing the impact force recordings from the uppermost steel mast and the concrete structure, the average front velocity between the two constructions is obtained for each avalanche. Unfortunately, there are no similar constructions closer to the dam for the measurements of the velocity at the base of the dam¹, but for some of the test avalanches the time lag between the front arrival at the concrete structure and at the mast on the dam has been recorded.

3.2 Properties of analyzed avalanches

The avalanches presented in Table 1 below are used in the calculations of the effect of the catching dam. The content of the table is as follows:

Avalanche date, observed run-out (x_2), over-run length measured from the downstream base of the dam, the vertical freeboard when the avalanche occurred, calculated velocity at the base of the dam, avalanche volume, the spread-out ratio of the avalanche at the dam site compared to the width of the avalanche in the track at 660 m a.s.l. (100 m above the dam along the horizontal), and a short description of the avalanche.

¹An attempt was made to use geophones buried in the ground in front of the dam and at the dam side for obtaining velocity data. This method does not work for several reasons, however: (i) The acoustic energy emitted by the avalanche is transmitted through the ground at speeds in the range of 2–5 km/s over large distances. The recordings at the different geophones thus exhibit a time lag of a few milliseconds determined, not by the avalanche speed, but by the distance between the geophones. (ii) Experience from several experiments in Spain (Suriñach et al., 2001) and Japan shows that the main sources of acoustic emissions during avalanche flow are obstacles in the path or abrupt slope changes. The seismic signals thus mainly contain information on the passage of the avalanche over such points.



In this last column there is a distinction between 'dry avalanches' and 'powder avalanches'. None of the avalanches in Ryggfonn are true 'powder' avalanches, as all of them are a combination of a flowing part and a dust cloud. For some avalanches, the dust cloud was predominant compared to the flowing part. These avalanches consisted of very loose dry snow in the whole track, and are named 'powder avalanches' here.

Table 1 Analysed avalanches

Avalanche date	Over-run length (m)	Free-board (m)	Avalanche volume (103 m ³)	Spread-out ratio	Release	Type
830110	148	14	100	1.1	Nat.	Dry
830308	-22	13	45	1.5	Nat.	Dry
850213	48	16	20	2.3	Art.	Powder.
870128	203	14	70	3.8	Nat.	Dry.
880411	23	16	40	2.4	Art.	Dry.
881223	38	15	75	1.5	Nat.	Dry
900307	48	15	30	1.8	Nat.	Powder
930327	151	6	20	1.5	Art.	Powder
940124	29	16	40	3.0	Nat.	Dry
950303	58	15	20	2.0	Art.	Powder
970208	173	5	100	1.9	Nat.	Dry
000217	311	5	80	2.2	Art.	Powder

As can be seen from the table, the observed over-run lengths range from -22 m to 311 m when measured from the downstream base of the dam. Most of the avalanches occurred when the freeboard was close to its maximum, 16 m, only 3 of the avalanches have considerably lower freeboard, at 5 m, 5 m and 6 m respectively. The computed velocities at the base of the dam vary from 17 m/s to 49 m/s. The observed velocities at the location of the concrete construction 230 m uphill from the dam vary from 34 m/s to 49 m/s. The avalanche volume varies between 20,000 m³ and 100,000 m³.

The correlation between the kinetic energy at the base of the dam and the over-run length is presented in Figure 8. There is a positive correlation between the two variables as $R^2 = 0.77$ for all of the twelve avalanches. Excluding the three avalanches where the freeboard was only 5–6 m the correlation improves to $R^2 = 0.79$.

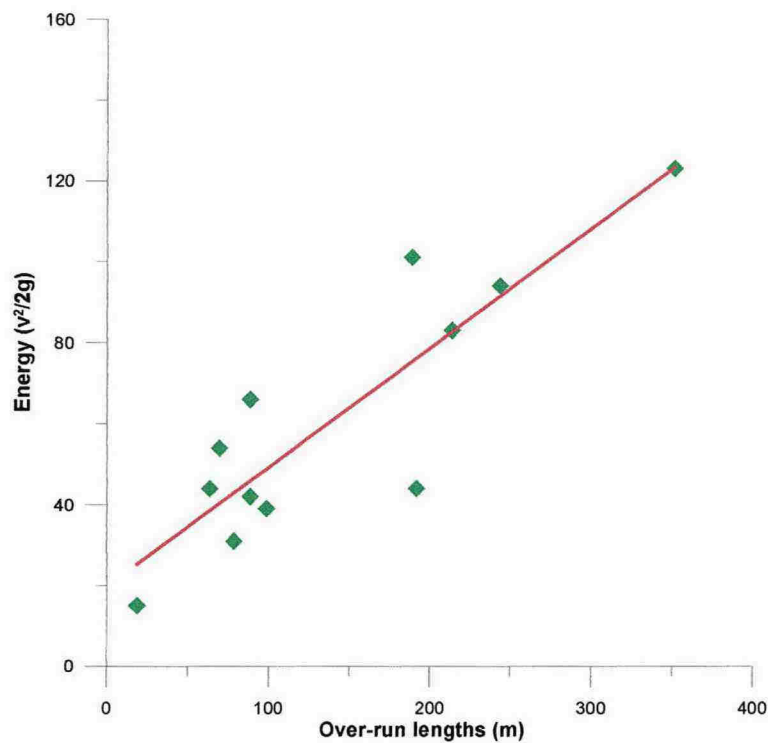


Figure 8 Correlation between avalanche energy ($v^2/(2g)$) and over-run length. Velocity is measured at the base, prior to the dam, and this point is also the basis of these over-run lengths.

The volume of the avalanche and the over-run length are correlated also, as avalanches with big volumes, not unexpectedly, give longer run-out distances, see Figure 9. The correlation is a little weaker than for the kinetic energy, with $R^2 = 0.71$.

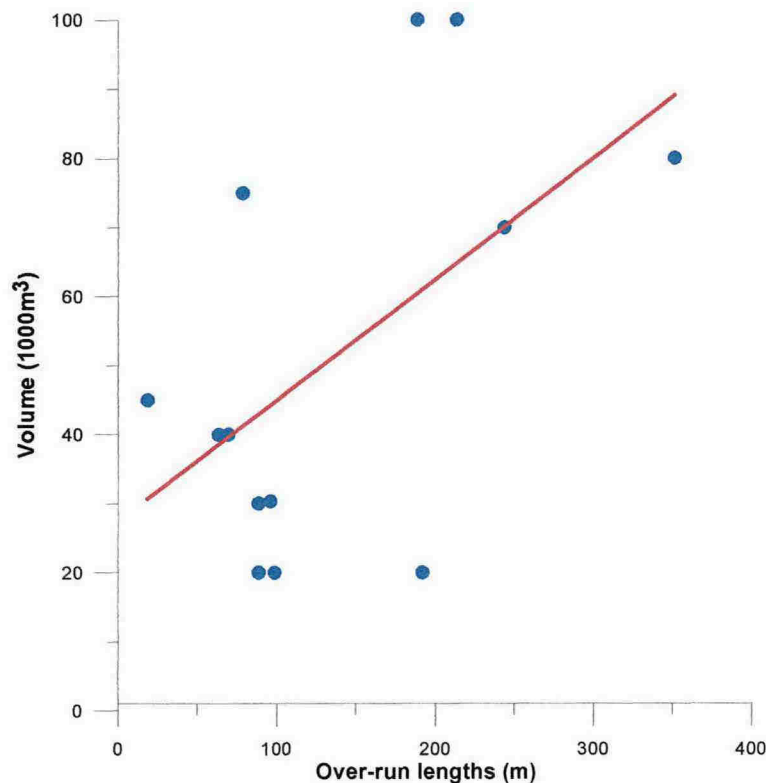


Figure 9 Correlation between avalanche volume and over-run length.

But, as can be seen from Table 1, it is not the two biggest avalanches with volumes of 100,000 m³ each that have the longest run-outs. The longest is the 80,000 m³ avalanche of 2000/02/17, the 'powder' avalanche that destroyed the mast and had a run-out of 352 m, although the freeboard of the dam was only 5 m at the time of the avalanche release. This avalanche, at the same time, ascended about 90 m on the opposite side of the valley, beyond the dam. The longest run-out with a nearly full freeboard of the dam was the avalanche of 870128. It reached 244 m with a velocity at the base of the dam of 43 m/s and a volume of 70,000 m³. The spread-out of this avalanche was 3.8 times the width in the track, which is considerably more than for the other avalanches, see the maps in Figs 20-43.

3.3 Spread-out ratio

The lateral spread-out of the avalanche debris around the dam differs considerably. The spread-out caused by the dam is difficult to measure in an objective way, but the maps showing the outline of the avalanches give an indication of the spreading. The spread-out ratio in Table 1 is the ratio between the maximum width of the deposit in the run-out zone and the width of the avalanche at contour line 680 m a.s.l. (at horizontal position x=1540). This is the highest point in the track where the dam is assumed to have had any

influence on the avalanche movement. The ratio between the maximum width of the deposit and the width at contour line 680 m a.s.l. differs from 1.1 to 3.8 with an average of 2.1. As can be seen from the table, there is no clear relation between speed, volume, run-out and spread-out ratio. As an example, the 830110 avalanche with a spread-out ratio of 1.1 has a volume of 100,000 m³, velocity 44 m/s and over-run length of 189 m, but in the 970208 avalanche, which has about the same volume, over-run length and velocity, the spread out is 1.7 times greater. The relation between spread-out ratio and speed, volume and over-run length is seen in Figs. 20-43.

The effect of the spread-out on the run-out is difficult to assess except for the probable effect that a high spread-out ratio should result in a shorter run-out. A high spread-out ratio will probably also reduce the flow height and the accumulation height in the run-out zone. As the lateral spreading is a typical reaction for all the avalanches, it should be accounted for in future three-dimensional modelling of catching dams.

3.4 Compression of the avalanche snow

The avalanche snow is compressed as the avalanche hits the dam. A rough indication of this compression can be obtained by comparing the density of the snow in the starting zone with the density of the debris near the dam.

As the access to the starting zone usually is not possible, the density of the slab is estimated based on the snow profiles at the research station 4 km from Ryggfonn, and from the weather conditions prior to the release. Based on these observations, the average slab density in the starting zone is estimated at 300 kg/m³. The average density of the deposited snow near the dam (bulk density) is 430 kg/m³, which means a 43 % increase of the density from slab to deposit.

This is a rough estimate only, since no systematic measurements throughout the deposit have been performed and the variation of density with increasing distance from the dam is therefore not known. A calculation of the energy loss due to compression against the dam is therefore not possible. Densification of the snow will take place also because of the avalanche movement itself, whether the avalanche hits the dam or not.

4 RESULTS OF THE SIMULATIONS BY THE NIS MODEL

In Table 2 it can be seen that the simulated run-out distances match the observed ones fairly well. In the average, the simulated avalanches ran 12.5 m farther than observed, with a standard deviation of 28 m. These results were obtained with reasonable values of the fracture depth and length, and the basic model parameters were within the range determined earlier by simulating over



200 events from NGI's avalanche database. The values used were $\tan \phi = 0.20-0.38$ for the friction angle, $m = 0.0005-0.0014 \text{ m}^2$ for the shear stress viscosity, and $\nu_1 = 0.008-0.0132 \text{ m}^2$, $\nu_2 = 0.1 \nu_1$ for the normal stress viscosities.

Table 2 Simulation results for analysed avalanches. $v_{LC \text{ sim}}$: Simulated velocity at the load cells, $v_{LC \text{ obs}}$: Observed velocity at the load cells, $v_{\text{base upstream}}$: calculated velocity at the base of the dam, prior to the impact, $v_{\text{dam top}}$: calculated velocity at the top of the dam.

Date	Free board [m]	Velocities			$v_{LC \text{ sim}}$ [m/s]	$v_{LC \text{ obs}}$ [m/s]	$v_{\text{base upstream}}$ [m/s]	$v_{\text{dam top}}$ [m/s]
		hor. run out beyond base of dam	sim. over-run with dam	sim. over-run without dam				
830110	14	148	141	214	48	46	44	36
830308	13	-22	0	25	23	23	17	6
850213	16	48	72	111	34	34	29	19
870128	14	203	195	230	49	48	43	39
880411	16	23	80	127	35	38	29	21
881223	15	38	39	72	31	31	25	15
900307	15	48	60	140	44	43	36	28
930327	6	151	129	161	35	35	29	25
940124	16	29	84	126	37	33	33	22
950303	15	58	78	115	33	35	28	19
970208	5?	173	172	200	46	45	40	36
000217	5	311	307	338	52	49	49	45
avg. (5&6m free b.)			203		45	44		
avg. (>13m free b.)			83		36	36		
avg. not incl. 940124			116		39	39		

The computed velocities at the location of the load cells 200 m above the dam site correspond closely to the observed velocities. Based on this close relationship, it is anticipated that the correspondence between computed velocities and real velocities at the base of the dam are at the same level also. The last column of Table 2 shows the computed velocity at the top of the dam. Besides the reversible conversion of kinetic to potential energy, there is energy loss due to the transition between the terrain above the dam and the dam side, see (20), and due to the friction work as the avalanche travels uphill along the dam side, see (14).



This loss of energy is shown in Table 3, in meters and in percentage. The average loss of energy caused by the dissipation in the bend at the upper base of the dam and the friction work along the dam side is 23% for the dam when the freeboard is between 13 and 16 m, and 15% for a freeboard between 5 m and 6m. The total average is 20%. While the dam height ratio in these two cases is 2.7, the ratio of energy loss is 1.5, which means that the energy loss in the bend is more important than the energy loss due to friction along the dam side.

The run-out on an 'endless' dam side would, in principle, be a natural test to run for the purpose of simulating the total loss of energy as the avalanche travels uphill. The NIS model in its present state is not well suited for that purpose on such steep inclinations as 40° because numerical instabilities develop, leading to strong fluctuations in the flow variables and rendering the run-up values unreliable. This is a challenge for the further development of the model, which hopefully will be solved. Such simulations will result in a greater energy loss than the 23 % mentioned above, as the distance travelled along a dam side long enough to stop the avalanche will be greater than at the actual dam in Ryggfonn where the avalanches studied overflowed the dam.

When the avalanche overflows the dam it gains velocity and thereby kinetic energy on the way down. As the avalanche hits the ground beneath the dam, it loses energy in the transition to the terrain. The total frictional energy loss as the avalanche travels across the dam is $2\mu gl$ and thus equal to the energy loss if the avalanche were to travel along the base of the dam, see (14). The loss of energy caused by the dissipation in the bends at the upper and lower base is shown in the two last columns. Expressed as a percentage, the average loss is 41 % for the 13–16 m freeboards.



Table 3 *Energy dissipation induced by the dam. E_i is the mechanical energy at the point i , ΔE_{ij} is the mechanical energy difference between the points i and j . Superscripts i and e denote simulation paths including and excluding the dam, respectively. The different positions for which the energies are considered are illustrated in Figure 10. The energy loss in columns 4 and 5 does not include the energy transformed to potential energy.*

Date	Freebd. used in sim.	Energy considerations				
		Kinetic energy at dam top $v^2/(2g)[m]$	Energy lost from base to top of dam (friction loss $\mu mg(x_0-x_1)$ and dissipation in bend)		Energy difference betw. simulation with and without dam. Absolute [m] and relative [%].	
			$\Delta E_{01}/mg [m]$	$\Delta E_{01}/E_0 [%]$	$(E_2^e - E_2^i)/mg$	$(E_2^e - E_2^i)/E_2^e$
830110	14m	65	24	24%	17	27%
830308	13m	2	2	10%	8	98%
850213	16m	18	10	23%	7	39%
870128	5m	78	13	13%	15	22%
880411	16m	22	8	18%	7	33%
881223	14m	11	8	24%	6	56%
900307	14m	40	14	22%	17	39%
930327	5m	33	7	17%	7	23%
940124	16m	24	16	30%	20	55%
950303	15m	18	9	23%	6	35%
970208	5m	66	14	17%	15	26%
000217	5m	101	18	15%	15	13%
Avg. 5 and 6 m free board				15%	21%	
Avg. 13-16m free board				23%	41%	
Total avg.				20%	34%	

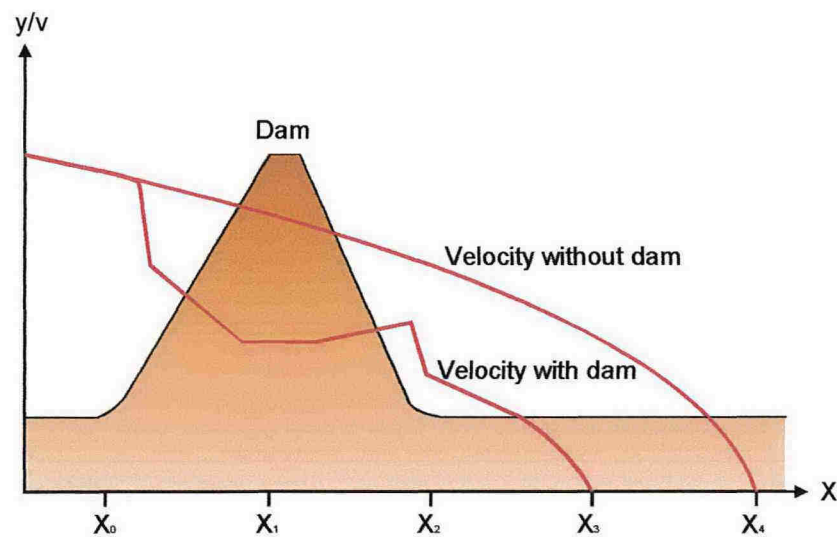


Figure 10 Evolution of velocity (and kinetic energy) as the avalanche passes the dam.

5 TRANSFORMING RUN-OUT DISTANCE INTO LACKING DAM HEIGHT

The following study is an attempt to establish a relationship between run-out distances on differently inclined planes. An application of such a relationship is to transform observed avalanche run-out to vertical ascending height on a retaining dam of given inclination. The study is simplified by treating the avalanche as a point mass, taking only dry friction and gravitational forces into consideration. This means that viscous friction, lateral spreading and rheological effects such as granularity, sintering and visco-elasticity are neglected. These effects more or less depend on velocity, acceleration, flow height and terrain, while the present treatment, as will be shown, only depends on horizontal and vertical distance travelled.

McClung and Mears (1995) present a more comprehensive study of this problem. They suggest that in the run-out area, where terrain inclination is less than 25° , locking takes place in the avalanching mass. Locking means that the avalanche mass assumes a uniform velocity profile, and slides like a plug. This implies that viscous and rheological effects are less significant and that the friction of the sliding mass is the major parameter controlling the motion in the run-out zone. Terrain inclination is probably not the most important parameter for the creation of a plug flow, but rather the velocity and the snow quality. Low velocities and dense, humid snow will more easily induce a plug flow, whereas dry, light snow will tend to move as a shear flow, also at inclinations lower than 25° . Beyond the catching dam in Ryggfonn, most of the avalanches

probably moved as plug flows, but one cannot disregard the possibility that the avalanches with the longest run-out partly moved as shear flows.

The study of McClung and Mears yields two expressions for the ascending height on retaining dams, and both are of the form $h = \frac{v^2}{2g\lambda}$, as is the one we obtain here. However, their λ includes the geometry of the dam and the terrain at the dam base (the difference in inclination between the dam wall and the upstream slope). A value for μ is also required. This gives a more general expression than ours, because our λ is specific to the Ryggfonn dam site and to dams with similar geometry.

5.1 Description of the approach

The relationship involves these parameters:

- μ dry friction coefficient
- e total specific mechanical energy (energy per mass; $e = v^2/2 + gh$)
- S distance travelled along path
- v particle velocity

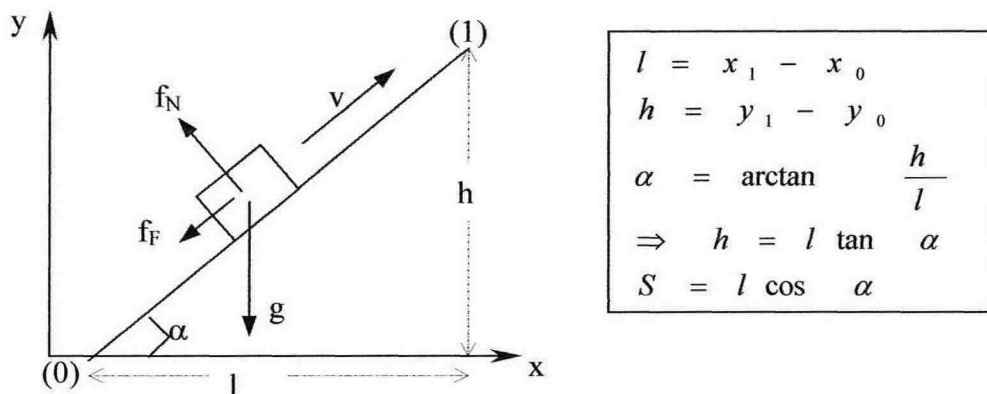


Figure 11 The simplified situation. (Note that an ascending slope has a positive α in this chapter!)

Choosing the reference point for the potential energy at the up-slope base of the dam, all energy is kinetic there by definition. At the rest point, the remaining total mechanical energy has been converted to potential energy.

$$e_0 = \frac{v_0^2}{2} \quad \text{and} \quad e_1 = gh = gl \tan \alpha \quad (12)$$

The work w_F done by friction forces must be equivalent to the difference in mechanical energy between the points 0 and 1:

$$\Delta e_{01} = e_0 - e_1 = w_F \quad (13)$$

where $w_F = f_F \cdot S$, $f_F = \mu f_N$ and $f_N = g \cos \alpha$.

Combining (12) and (13) gives the run-up height:

$$\Delta e_{01} = w_F = f_F \cdot S = \mu g \cos \alpha \cdot \frac{l}{\cos \alpha} = \mu gl \quad (14)$$

$$\frac{v_0^2}{2} - gl \tan \alpha = \mu gl \quad (15)$$

This equation can be solved for different parameters, depending on what is known a priori. Relevant to our task are the following possibilities:

1. Determination of the dry friction coefficient μ from observed run-out and velocity:

$$\mu = \frac{v_0^2}{2gl} - \tan \alpha \quad (16)$$

2. Applying this μ to calculate run-out l along a slope of known inclination α (e.g. a dam), given the velocity v_0 :

$$l = \frac{v_0^2}{2g(\mu + \tan \alpha)} \quad (17)$$

3. Combining this with the relation $h = l \tan \alpha$, one obtains the run-up height (e.g. for giving an estimate of the necessary dam height when designing a dam):

$$h = l \tan \alpha = \frac{v_0^2 \tan \alpha}{2g(\mu + \tan \alpha)} \quad (18)$$



For an avalanche with observed velocity in one point (0) and known run-out position (1) in the absence of a dam, the following equation applies for the vertical ascending height on a prospective dam, located at point 0:

$$h = \frac{v_0^2 \tan \alpha}{2g \left(\tan \alpha + \frac{v_0^2}{2g(x_1 - x_0)} - \frac{y_1 - y_0}{x_1 - x_0} \right)} \quad (19)$$

5.2 Dry friction dissipation of energy in the bend

The run-up height given by (19) is a conservative estimate, as it does not take into account any dissipation mechanisms other than the velocity independent dry friction. The magnitude of the increased friction work per unit mass due to centrifugal forces in the upstream bottom bend is approximately

$$\begin{aligned} \Delta w_{centrifugal} &= \mu f_{centrifugal} S_{bend} \\ &= \mu \frac{v^2}{r_{bend}} \Delta \phi_{bend} r_{bend} \\ &= \mu v^2 \Delta \phi \approx \mu v_0^2 \alpha \end{aligned} \quad (20)$$

where $\Delta \phi_{bend}$ is the increase in inclination from upstream of point (0) to the dam side (inclined at an angle α), μ is the effective friction coefficient in the bend and v^2 is the average squared velocity through the bend (always less than v_0^2). Typically, $v \approx 20$ m/s, $\mu \approx 0.2$ and $\Delta \phi \approx 1$, which corresponds to a lost theoretical ascending height of about 8 m—a considerable loss, even with modest values of v and $\Delta \phi$. Note that the loss grows with the square of the avalanche velocity. For avalanches that travel past the dam, these considerations have to be made for all three or four (depending on the shape of the dam crown) bends. Due to the velocity difference between the bottom and the crown, the net energy loss is approximately $4\mu g H_{dam} \Delta \theta$, with $\Delta \theta$ the slope change at the bends. Depending on the slope in the run-out zone, on the dam geometry and on the velocity dependence of the dry friction, this translates into a typical shortening of the run-out distance of $\Delta s \approx -(2-4) H_{dam}$. If avalanche impact pressure is estimated by means of the traditional formula $p \approx \rho u^2$ with $\rho \approx 300$ kg/m³, p is uniformly reduced in the run-out zone by $\Delta p \approx -8\mu \rho g H_{dam} \Delta \theta \approx -(6-12)$ kPa/m $\cdot H_{dam}$.

5.3 Overrun length

The overrun length is the basis of the friction coefficient evaluation. It would appear natural to select the dam crown as the starting point of the overrun distance. However, a significant dissipation of energy takes place as the



avalanche leaves the dam. This happens as the mass hits the ground after squirting through the air or as it runs through the bend at the lower base of the dam. Hence, if the dry friction is to be 'blamed' for this distinct dissipation of energy, the coefficient μ will be given an unreasonably high value, and the estimate of lacking dam height will be non-conservative. The best basis for calculating μ is therefore a point close to, but downstream of, the lower base of the dam. In our case, no observed velocity data are available for this point, only the simulated velocities. These, however, are probably relatively accurate, as the simulated run-out distances correspond well to the observed ones.

To develop a general equation for the lacking run-up height on the dam, the interval used for evaluating μ is called AB (with velocity v_A at A and zero at observed run-out at B). This is necessary for distinguishing between the velocity and the position used to compute μ , and the parameters used for evaluating run-up height with this μ . The dry friction coefficient is then:

$$\mu = \frac{v_A^2}{2g(x_B - x_A)} - \frac{y_B - y_A}{x_B - x_A} \quad (21)$$

Inserting (21) for μ into (18) gives the run-up height

$$h = \frac{v_0^2 \tan \alpha}{2g \left(\tan \alpha + \frac{v_A^2}{2g(x_B - x_A)} - \frac{y_B - y_A}{x_B - x_A} \right)} \quad (22)$$

Neglecting the dissipation of energy as the avalanche passes over the dam will result in a too high value of μ , giving a non-conservative estimate of the lacking dam height. The interval chosen for evaluating μ is therefore from the lower base to the run-out point. The velocities simulated by the NIS model are applied as v_A .

The additional run-up height can then be calculated by inserting the following expressions:

$$v_0 = v_{dam\ top}$$

$$\tan \alpha = \frac{\text{vertical extension of dam}}{\text{horizontal extension of dam}} = \frac{16m}{19m} = 0.84$$

$$v_A = v_{downstream\ base}$$

$$(x_A, y_A) = \text{downstream base}$$

$$(x_B, y_B) = \text{simulated runout}$$

This results in a series of potential run-up heights on prospective, large enough dams. The data are presented in Table 5. The ratio λ between the computed run-up height and the velocity head at the upstream dam base is also presented in the table. If at all such a simple relation captures reality, then the run-up height can be estimated from the basic expression:

$$h = \frac{v_{upstr.base}^2}{2g\lambda} \quad (23)$$

However, this is obviously a simplified way of estimating necessary dam height, as avalanches differ severely in several aspects: lateral size and spreading, volume, velocity (and velocity-dependent resistance) and rheological characterisation, as previously described.

5.4 Results and discussion

Table 5. Run-up heights based on dry friction consideration. Note that the values for μ given in the third column are not related to the friction parameters chosen in the simulations with the NIS model.

Date	α and μ computed from the downstream base of the dam to run-out.		h [m] including free board	$\frac{v_{upstream\ base}^2}{2g}$ [m]	λ in $h = \frac{v_{base}^2}{2g\lambda}$
	α [°]	μ_{eff}			
830110	1.1	0.38	57	101	1.78
850213	1.1	0.18	29	42	1.45
870128	6.3	0.19	67	94	1.41
880411	-2.3	0.28	30	44	1.45
881223	-1.7	0.26	21	31	1.49
900307	0.5	0.63	35	66	1.90
930327	1.3	0.18	31	44	1.43
940124	-0.2	0.25	32	54	1.67
950303	1.4	0.17	27	39	1.44
970208	3.5	0.22	56	83	1.49
000217	14.2	0.08	95	123	1.28
Average			44	66	1.53

As can be seen from the table, the λ -factor ranges from 1.28 to 1.90, with an average of 1.53, corresponding to a total energy loss of 35% caused by the dam. This loss includes both the energy dissipation at the upstream and downstream sides of the dam, plus the friction work at the dam. The result is



in good agreement with the energy loss presented in Table 2 where the calculated loss is 34%.

For some of the avalanches, the effective friction parameter, μ , listed in the third column of Table 5 takes extremely low values, especially for the most extreme event of 17/2/2000. These values were obtained by equating the simulated kinetic energy of the avalanche head at the downstream end of the dam with the potential energy gain (or loss) to the simulated run-out point plus the frictional work done over the distance. Readers familiar with the widely used Voellmy–Salm or Perla–Cheng–McClung (1980) models will object that the dynamical models can reproduce these observed run-out distances only if the dry-friction coefficient in the model is chosen even smaller than the μ listed in Table 5. The following considerations are relevant in resolving this enigma:

- As mentioned earlier, there are uncertainties in the evaluation of the average front velocity between the tower and the concrete structure. It is quite possible that the February 2000 avalanche was significantly faster than indicated in Table 2.
- For avalanches with a strongly developed powder-snow part, the run-out distance of the dense core is often very hard to determine. The value given in Table 1 may well refer to the deposit of highly fluidised material, i.e., to what might be termed the saltation layer of the avalanche. If so, very low values of the effective friction are to be expected.
- The dry friction parameter values of Table 5 are strongly influenced by the fact that the front is pushed by the tail. For the avalanches travelling far up onto the opposite valley slope, this effect is significant. Described below is an approach for a sounder determination of the dry friction coefficient for the simulations that allow it.

For the simulated avalanches that did not deposit any material above the dam, another approach may be chosen that gives more reasonable values of μ : Considering the avalanche like a particle, located at the avalanche centre of mass, with potential and kinetic energies averaged over the whole avalanche. This is done by inserting the following into (21):

$$x_A = \bar{x} = \frac{\sum_i x_i h_i}{\sum_i h_i}, \quad y_A = \bar{y} = \frac{\sum_i y_i h_i}{\sum_i h_i}, \quad v_A^2 = \bar{v}^2 = \frac{\sum_i v_i^2 h_i}{\sum_i h_i} \quad (24)$$

These equations are evaluated right after the tail of the simulated avalanche has cleared the dam. A similar evaluation of x_B and y_B is performed after the simulated avalanche has stopped. With this method we obtain more realistic dry friction parameters for the two avalanches listed in Table 6. For the rest of the avalanches, this evaluation method was not possible: Either the front of the

avalanche had stopped as the tail left the lower base of the dam, or the tail itself was stopped above the dam, both cases resulting in an inaccurate evaluation.

Table 6 Comparison between dry friction parameter used in NIS model simulations and the ones obtained with the methods described above.

Date	μ used in NIS-simulation	μ obtained from avalanche front consideration	λ corresponding to μ of column #3	μ obtained through particle consideration	λ corresponding to μ of column #5
870128	0.30	0.19	1.41	0.30	1.36
000217	0.16	0.08	1.28	0.23	1.27

The remarks above illustrate some of the difficulties encountered in such an analysis. We hope that the experimental equipment at Ryggfonn can be extended in the near future to obtain more definite answers to these and similar questions.

6 THEORETICAL CONSIDERATIONS ON DAM EFFECTIVENESS

The preceding sections used experimental data in combination with a dynamical model of avalanche motion to answer the two main questions with regard to dam design, i.e., (i) How high does a dam need to be in order to completely stop avalanches? (ii) To which degree does a dam of a given height reduce the effects of avalanches that overflow it? There are considerable uncertainties involved in the use of such a hybrid method, and it would be desirable to define a useful measure of dam effectiveness that is amenable to direct measurement. In this section, we discuss preliminary thoughts on the physical processes at work in avalanche-dam interactions, in view of the proposed EU project SATSIE (Issler and Lied, 2001).

6.1 Mitigating effect of an overflowed dam

If we consider the balance of kinetic and potential energies at the dam, we observe the following points, some of which were already noted in the preceding sections:

- If the kinetic energy is sufficient, the dam is overflowed. However, even if the kinetic energy of the front would be insufficient, the main body of the avalanche may still push the front over the dam.
- The kinetic energy lost to potential energy on the upstream side is regained descending on the downstream side.



- Specific energy dissipation at the dam due to dry friction with a constant friction coefficient is given by μgl where l is the length of the dam in the flow direction. It equals the frictional energy loss *without* the dam—the longer path $l / \cos \alpha$ over the dam is offset by the reduced normal force $\sim g \cos \alpha$ on the slopes.
- Centrifugal forces increase the friction in the bend at the foot of the dam and decrease it at the crown.
- In the presence of a dam, the energy loss due to the drag forces is slightly smaller for slow avalanches and somewhat larger for fast avalanches than it would be without a dam. This effect is not significant, however.

None of the effects considered thus far depends on the volume of snow retained by the dam. Intuitively, one expects the retention capacity of the dam to determine the degree of protection afforded by it, but what mechanisms beyond increased friction due to centrifugal forces may be responsible for such an effect? Consider a grossly oversimplified conceptual model representing the avalanche as a series of large blocks sliding down-slope without mutual interaction and the dam as a trench: After the first few blocks have filled the trench, all the following blocks pass over it unhindered. The run-out distance and the pressures would be virtually unchanged, only the deposit mass would be reduced. Hence, if the retention capacity of the dam indeed influences the effect of an overflowing avalanche, the interaction between stopped and overflowing snow masses, between front and rear of the avalanche must be the decisive factor.

Nevertheless, there is a secondary effect related to retention capacity that is worth mentioning: As will be argued below, it is mainly snow from the head of the avalanche that is stopped by the dam. The flow velocities in the rear of the avalanche are typically much lower than in the head, as evidenced by radar measurements (Schreiber et al., 2001). A dam is therefore all the more effective the more of the fastest parts of the avalanche it is able to stop.

The behaviour of a snow avalanche is in many respects intermediate between the behaviour of a fluid in open-channel flow and a plastic solid. Let us first examine to which degree we may exploit the analogy with open-channel flows. At low inflow velocities, the water will fill up the space behind the dam without forming appreciable waves. Once the water level has reached the dam crown, water flows over it at essentially the same rate as the inflow discharge. At intermediate velocities, a supercritical flow enters the pond behind the dam and becomes undercritical at a hydraulic jump; at some point on the downstream side of the dam, it may turn supercritical again. In both cases, the dam influences the entire pond, the front and the rear of the flow interacting through pressure gradients. Note, however, that energy is mainly dissipated in the hydraulic jump, the formation of the pond *per se* does not induce energy loss. The deposit shapes of the 19940124 and 19970208 avalanches are in rough agreement with such an interpretation, but only the 1994 event exhibits the short run-out associated with a relatively slow avalanche.



Fast open-channel flows, in contrast, stay supercritical all the way, flow heights are relatively small everywhere, and the effect of the dam is not felt upstream of it. The deposit profiles of the 1993/03/27, 1995/03/03 and 2000/02/17 events exhibit the long and relatively uniform, shallow deposits that would be expected in a comparable avalanche flow regime. However, in the 1993 and 2000 events, the freeboard was reduced to only about 5 m by preceding avalanches.

The analogy with open-channel flow of water must not be stressed too much for several reasons: Dense-flow avalanches operate at much lower Reynolds number than typical open-channel flows, i.e., viscous effects (and quasi-static friction) are very important in avalanche flow. At low velocities, locking takes place and the snow loses its fluid-like properties. Also, it is open to debate whether flow transitions in snow avalanches may be compared to hydraulic jumps. The limited usefulness of the comparison with open-channel flows is confirmed by the fact that more than half of the studied events exhibit a deposit shape that cannot be explained in hydraulic terms.

It has long been recognised that the impact of an extended mass of a compressible plastic material like snow on a stiff, not streamlined obstacle shows two distinct phases (Salm, 1964; Bozhinskiy and Losev, 1998, and references therein): During the first few milliseconds, some of the approaching material is compressed and stopped, forming a wedge-shaped 'cap' on the obstacle. The pressure is determined by the compressibility of the material and can be much larger than the stagnation pressure during this phase, of the order of $\rho u(u+c)$ where c is the propagation velocity of the compression wave travelling upstream. If the material is hard to compress, c is much larger than u . Once the stopped material has reached an equilibrium shape, the following masses flow around the obstacle and its 'cap', exerting a pressure that scales with the stagnation pressure, $\rho u^2/2$. It is chiefly this latter quasi-steady pressure that is relevant for the energy loss of the snow flowing over the dam.

The shape of the snow 'cap' on the obstacle is determined by the requirement that the local shear stresses are equal to the local shear strength. This problem is complicated because the shear stresses depend on the shape of the object, which changes as material is aggregating or being eroded again. Furthermore, the shear strength depends on the local normal stress, which also depends on the shape. Leaving an exploratory discussion of these issues to Sec. 6.4, we just note that the order of magnitude of the normal stress is given by the stagnation pressure. Assuming Coulomb-type dependence of the shear strength on the normal stress (possibly with a somewhat increased effective friction angle to account for cohesion), we conclude that the retarding effect of the dam is essentially given by the increased friction associated with the overpressure on the upstream side of the dam. (This is only partly offset by reduced friction on the downstream side since the flow is by no means inviscid.)

As discussed in Sec. 5, the NIS model simulations take into account the extra friction due to centrifugal forces. These may be considered as an approximation to the full shape-dependent pressure distribution over the obstacle and its 'cap'. Integrating the over-pressure over the modified obstacle surface and multiplying it by an appropriate effective friction coefficient μ , one obtains an energy loss $\Delta E = -\mu k \rho u^2 H_{\text{dam}}$, where $2k$ may be viewed as a drag coefficient for snow flow and for the object geometry modified by the snow 'cap', depending also on the ratio of flow height to dam height, h / H_{dam} .

We conclude that a dam mitigates the effects of an overflowing avalanche by completely stopping a fraction of the fastest avalanche parts and by reducing the speed of the overflowing masses by means of extra friction induced by the overpressure in the flow caused by the dam. This latter effect is approximately included in numerical models that include centrifugal effects.

6.2 Analysis of dam-induced avalanche mass loss from the deposition profiles

For most of the selected avalanches, deposition profiles along one or several lines in the flow direction are available for evaluating the deposited volume. Snow density in the deposit has sometimes been measured; typical values, confirmed by deposit analyses elsewhere, range from 450 to 600 kg/m³. An immediate difficulty encountered in the interpretation of the deposition profiles (see Figures 44-55 in the Appendix) is that a part of the snow found upstream of the dam would have been deposited there even without the dam present. At our present stage of knowledge and modelling, it is a matter of judgement to estimate the extra deposition induced by the dam.

In open-channel hydraulics it is well known that disturbances cannot propagate upstream if the flow is supercritical, i.e., if the Froude number $Fr = u / (gh)^{1/2}$ is larger than 1. Hydraulically, dense-flow avalanches with typical velocities above 10 m/s and flow depths below 10 m are always super-critical, except in the very first and very last phases of the flow. This argument has been used (albeit with some reservations) by Hungr and McClung (1987) and McClung and Mears (1995) to establish inflow boundary conditions for their leading-edge run-up models. One would then conclude that only the deposition right on the dam could have been due to the dam.

Table 7 Dam-induced deposit lengths (measured horizontally from the dam crown), total deposit volumes per unit width, deposit volumes per unit width downstream of the dam, estimated natural deposit volumes per unit width upstream of the dam (i.e., without the dam present), and extra volume per unit width retained by the dam. The retention efficiency is defined as the ratio of the extra snow volume retained by the dam to the snow volume that would have run beyond the dam location if the dam had not been present. See Figures 44-55 for a graphical representation of profiles and main text for an explanation of estimation assumptions and methods.

Avalanche date	Deposit length	Depth of natural deposit (m)	Natural deposit volume / width (m ²)	Observed deposit volume/width (m ²)	Difference	
	(m)				(m ²)	%
19830110	50	4,1	195	348	153	44
19830308	61	4	213	300	87	29
19850213	68	1,5	100	240	140	58
19870128	62	2,4	154	476	322	68
19880411	54	2,3	122	265	143	54
19881223	55	2,9	163	345	182	53
19900307	75	4,4	337	618	281	45
19930327	72	2,8	199	202	3	1,5
19940124	65	6,5	458	761	303	39,8
19950303	84	2	115	115	0	0,0
19970208	85	3,8	331	819	488	59,6
2000/02/17	120	2,5	283	311	28	9,0

The Froude-number argument, however, assumes the fluid to be incompressible and applies only to the propagation of gravity waves (or surges), but not to sound waves. The disturbance relevant to our problem is a shock front due to plastic compression of the snow masses. We will follow up on this line of thought in Section 6.4 and suggest here merely that the upstream boundary of the dam-induced deposit may be identified with a steep increase of the deposit depth (as seen in the downstream direction) that is not obviously due to local terrain features.

Table 7 summarises the beginning of the dam-induced deposits, their depth ranges, and the volumes per unit width stopped by the dam. Estimating these volumes required additional assumptions concerning the deposit depth that would have resulted without the dam; a value of 150% of the natural deposit depth just upstream of the zone of influence of the dam was adopted.

Some qualitative features are easily discerned from the maps, the deposit profiles and Table 7:

- The percentage of stopped mass is largest for those avalanches that came to a halt shortly after the dam. The fast, strongly fluidised avalanches



deposited a large fraction of their mass downstream of the dam, whereas slow avalanches began to deposit rapidly before reaching the zone of influence of the dam.

- Apparent deviations from the rule stated above are explainable by peculiarities of certain events: The dense core of the 19870128 avalanche, e.g., was narrowly channelled in the gully but widened enormously below 670 m a.s.l. The retention ratio calculated from a single profile line and reported in Table 7 thus does not correctly reflect the amount of snow deposited in the large fan beyond the dam. Similarly, the numbers for the 19970208 avalanche might change if the branch that passed to the south-west of the dam were taken into account. Finally, probably an even smaller fraction of the huge 2000/02/17 avalanche was stopped by the dam, considering the enormous width of the deposition fan and the difficulty of accounting for the powder snow deposits.
- Over two thirds of the deposits exhibit a typical shape like the crescent moon, with the largest depth near the foot of the dam. Exceptions are the events of 1993/03/27, 1995/03/03, and 2000/02/17. All these three avalanches are characterised by relatively shallow deposits. While the 1995 event belongs to the smallest specimens in our sample, the 2000 avalanche was the biggest and the most strongly fluidised.

6.3 Scaling behaviour

An important question in the design of catching dams is how the retaining capacity varies with the size and the shape of the dam, and how it depends on the avalanche parameters like flow depth, velocity, and snow properties. In Section 6.4 below, we will try to refine the crude concepts proposed in Section 6.1 to obtain an idea of the retaining capacity of a dam. But let us first consider some scaling properties that may be useful in applying laboratory measurements to dam design. Since the relevant intrinsic length scales in this problem are the dam height, H , and the flow height of the avalanche, h , it may be assumed on geometrical grounds that the retaining capacity per unit width of the dam, A , scales as H^2 :

$$A = k(h/H, \Delta\theta, Fr, \mu_{\text{eff}}, Ma, s/(\rho u^2)) H^2 . \quad (25)$$

(25) suggests that the constant of proportionality, k , in this scaling relation depends on h/H , on the Froude number, defined as $Fr = U / (gh)^{1/2}$, on the deflection angle, $\Delta\theta$, on the effective friction coefficient, μ_{eff} , on the Mach number, $Ma = (U/c)^2$, and on the ratio of material (shear) strength, s , to the dynamical stresses.

$\Delta\theta$ and h/H govern geometrical similarity, and some elementary considerations on the dependence of k on h/H and $\Delta\theta$ will be attempted below. The appearance of the Froude number implies that k should not change if we scale the avalanche flow height, the dam height and the *square* of the approach

velocity by the same factor while keeping the other dimensionless parameters constant. To the extent that Coulomb-like friction (independent of velocity and proportional to the flow height) and flow-height independent drag (proportional to u^2) are the dominant retarding forces in avalanche flow, Froude similarity is obeyed. If viscous forces are important, there is an additional dependence on the Reynolds number, which we will neglect here. The compressibility of the snow, parameterised by the Mach number, plays a central role in impact processes. The final parameter imposes dynamical similarity also in the failure process, i.e., when shear planes develop and a deposit is formed at the foot of the dam. If snow were a cohesionless granular material, the shear strength s would, in a first approximation, obey the Coulomb law, $s = \sigma_n \cdot \tan \phi$, where the normal stress, σ_n , scales with the flow depth, whereas the shear stresses generally scale with the square of the velocity. Once again, the Froude similarity condition ensures that they scale in the same way. While cohesion does not respect this scaling requirement, the deviations are expected to be moderate.

The discussion above suggests that laboratory experiments may be quite useful in dam design as they allow to map the parameter space of the coefficient k much more rapidly and economically than in full-scale experiments. However, particular attention must be paid to the scaling of the compressibility and the strength of the materials used in testing: If the linear dimensions are reduced by a factor 100 in the laboratory, the shear strength should also be diminished hundredfold. This may often be difficult to achieve in practice with cohesive materials, and tests with different materials of known strength should be used to establish the importance of the shear strength to shear stress ratio for, e.g., the deposit geometry and the energy loss of material crossing the dam.

6.4 Factors determining the deposit shape

In a sharp bend in an avalanche path, with the ratio of flow height to curvature radius, h/R , and the deflection angle, $\Delta\theta$ (measured in radians), both of order 1, the volumetric and shear strain in the snow mass becomes very large. In the situation of interest to us the velocities are high, and so very large stresses are generated. The density change occurs over a rather short distance and may thus be considered a compressive shock front (Figure 12). On a certain surface, the shear strength of the snow is exceeded and a shear surface develops, along which the material fails completely. The snow flowing above this surface is deflected, while it may be completely stopped below that surface.

The snow deposited in the bend tends to increase the radius of curvature and thus to make the change of direction more gradual. Once the bend has been smoothed enough, the stresses no longer exceed the shear strength of the snow, and the snow flows around the bend without further deposition. However, some compaction, shear and bulging still occur for geometrical reasons and due

to the pressure distribution in the flow. There is also increased dissipation due to the extra friction induced by the overpressure.

A full quantitative treatment of these processes is far beyond the scope of this paper: The problem is three-dimensional (two-dimensional in the middle of a sufficiently homogeneous and wide flow), time-dependent and highly non-linear. Moreover, the constitutive equation of snow under such conditions is still not very well understood. It may be possible to simulate the main processes with advanced numerical codes that can handle the strong advection effects due to the flow, the abrupt changes of the material properties, and singular surfaces like slip planes and shock fronts. However, the numerical problems will be extremely challenging, and a series of dedicated laboratory experiments will be needed to determine a suitable material model. We limit ourselves to discussing a few simplified situations that reveal some of the main effects.

Let us begin with the classical shock-tube problem (Figure 12), the application of which to snow impact problems has been discussed by several authors (e.g., Briukhanov et al., 1967; Mellor, 1977): Snow of density ρ_1 moves at a uniform velocity u_1 in a rigid, frictionless and evacuated tube until it impacts on the rigid lid. The snow is compacted to a density ρ_2 as it comes to rest. The interface between the moving and stopped snow moves upstream at a speed v . From the conservation of mass and momentum, one finds

$$v = u_1 \frac{\rho_1}{\rho_2 - \rho_1} \quad \text{and} \quad p_2 - p_1 = \rho_1 u_1 (v + u_1) = u_1^2 \frac{\rho_1 \rho_2}{\rho_2 - \rho_1}. \quad 19)$$

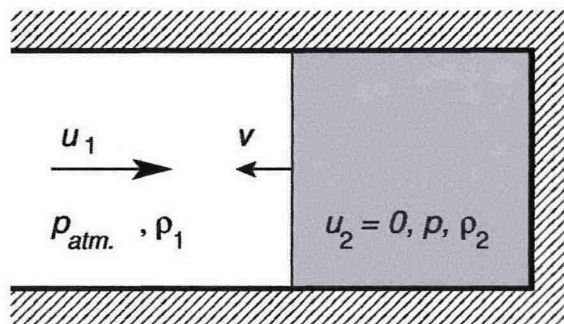


Figure 12 One-dimensional shock-tube problem. v is the velocity of the shock front between the avalanche snow arriving from the left and the stopped and compressed snow at the right.

Typical values for snow avalanches are believed to be $\rho_1 = 150\text{--}300 \text{ kg/m}^3$, $\rho_2 \approx (1.5\text{--}3)\rho_1$. Note that the flow is always ‘subsonic’ because the shock wave travels upstream. In order to solve this comparatively simple problem, a

constitutive equation relating p and ρ is required. If it is assumed of the form $\rho_2 = f(\Delta p, \rho_1)$, i.e., if rate-dependent effects are neglected, ρ_2 and Δp can be determined by iteration. One may further assume that the impacting snow consists of single ice grains and air (i.e., any originally existing bonds are broken down during avalanche flow or in the very first instants of impact) and that its permeability is low compared to the shock propagation velocity v . Then the equation of state with respect to an initial or reference state with $\rho = \rho_{ref}$, $T = T_{ref}$, $p = p_{ref}$, becomes

$$r = \frac{1}{\frac{\tau}{\pi} + c_{ref} \cdot \left(1 - \frac{\tau}{\pi}\right)} \quad (27)$$

where $r = \rho / \rho_{ref}$, $\tau = T / T_{ref}$, $\pi = p / p_{ref}$. We assume the compression of the air to be adiabatic, leading to $\tau / \pi = \pi^{-1/\kappa}$; in the temperature range of interest, $\kappa \cong 1.4$. (Briukhanov et al. (1967) consider the process to be isothermal due to the high heat capacity of ice.) Introducing these expressions in the equation for the pressure rise given above and solving for the initial (reference) density in terms of the pressure rise yields, after some algebra,

$$\frac{\rho_{ref}}{\hat{\rho}_{ice}} = \frac{1}{1 + \frac{(\hat{\rho}_{ice} - \hat{\rho}_{air})u_1^2}{p_{atm.}} \cdot \frac{1}{(\pi - 1)(1 - \pi^{-1/\kappa})}} \quad (28)$$

$\hat{\rho}_{ice}$ and $\hat{\rho}_{air}$ are the intrinsic densities of pure ice and air, respectively, at reference temperature and pressure. Figure 13 shows the rise of the peak pressure with initial snow density for different impact velocities. The values differ somewhat from the plot given in Briukhanov et al. (1967) for isothermal compression, but the trends are the same.

Experimental measurements testing the assumptions behind this simple theoretical approach would be very valuable because extensions to two-dimensional flows, to be discussed below, depend on the validity of the basic mechanism. However, the technical difficulties might be considerable: In order to make the setting essentially one-dimensional, an almost frictionless, rigid cylinder and a sufficiently large mass of snow would have to be used. Care has to be taken that the air between the snow sample and the rigid impact wall can easily escape before impact; the snow, however, must be radially confined from the moment of impact. If the snow sample is accelerated too rapidly, it might be compacted thereby; if the snow is kept at rest and the impact wall is in motion, inertial effects have to be accounted for.

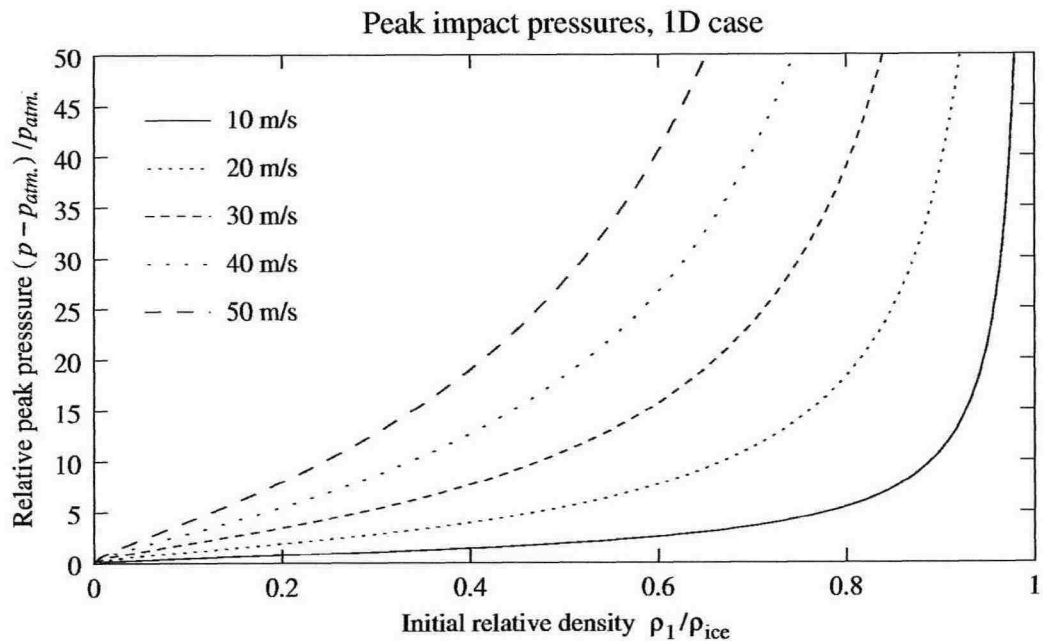


Figure 13: Pressure difference across compression shock front in the one-dimensional impact of snow on a rigid obstacle as a function of initial snow density, for different initial velocities. Adiabatic compression is assumed.

Briukhanov et al. (1967) discuss supersonic flow over a wedge (representing a dam). To the extent that gas dynamics is applicable and the approaching flow is truly supersonic, a compressive shock should develop from the foot of the dam (Figure 14). Whereas calculation of the velocity, density and temperature after the shock front is straightforward for an ideal gas because the angle $\alpha + \beta = \arcsin(c / u_0)$ of the Mach cone is known a priori, it must be determined together with all other variables in the case of a snow-air mixture, using the complicated equation of state stated above.

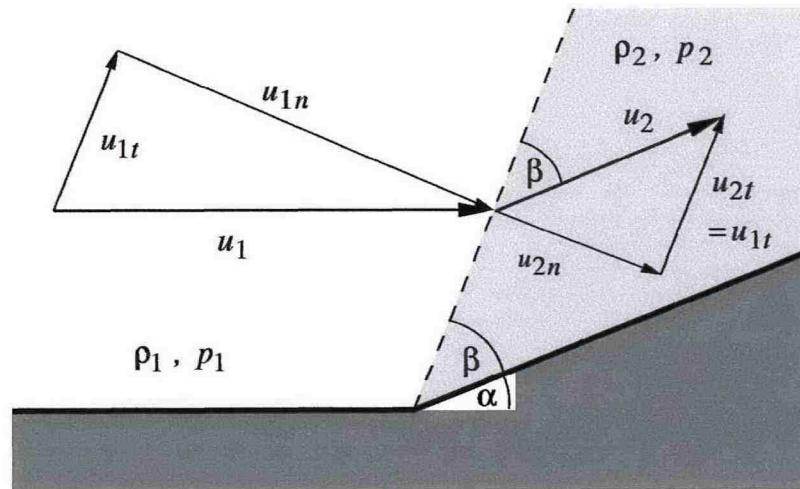


Figure 14: Supersonic flow over wedge as a model of avalanche-dam interaction at high velocities. After Briukhanov et al. (1967). Note that the velocity is reduced across the oblique shock front whereas the density increases. The inclination of the shock front depends on the approach velocity u_1 and the compressibility of the snow.

It is not completely clear how practically relevant this scenario is. Briukhanov et al. (1967) argue that the sound velocity inside an air-snow mixture is very low—lower than the flow velocities inside fast avalanches.² If we indeed assume $Ma > 1$, the consequence is that no snow is stopped in front of the dam if the deflection angle is not too large because no information on the presence of the dam propagates upstream through pressure. Along the dam slope, the snow is compacted under significant excess pressure, and the velocity is reduced. Even though this is not derivable from the equation of state, we may assume that the compression is quite dissipative at high densities, i.e., the compacted snow does not expand significantly after passing the dam. The work per unit mass, needed for compressing the snow is roughly $w \approx -(\Delta p / 2\rho_0) (dV / V) \approx 0.2 \Delta p / \rho_0$. At an impact velocity of 30 m/s and an initial density of 300 kg/m³, $w \approx 400$ (m/s)². The dissipation will be somewhat less than w , and we may guess that the velocity will be reduced from its initial value of 30 m/s to about 25 m/s by this effect alone.

The analogy with gas dynamics suggests that the shock front may be curved, located about one dam height upstream of the dam and detached from the latter

² Note, however, that their argument is based on the classical formula for sound velocity, $1/c^2 = (dp/d\rho)_s$, the derivation of which implicitly assumes a homogeneous medium. If the frequency of a pressure fluctuation is higher than the inverse response time of the snow grains, the latter no longer contribute to the inertia of the gas but act as essentially fixed but randomly distributed scattering centres and c will not be reduced as much as predicted by the classical formula.

if the deflection angle is large enough. It is expected that the main conclusions drawn above will not be altered, however.

The next step considers the two-dimensional problem of a uniform avalanche approaching a rigid vertical wall. Bozhinskiy and Losev (1998) summarise a calculation by Gonor and Pik-pichak (1983) where a non-linear equation of state was assumed for the snow and several simplifications were introduced. Peak pressures were found smaller by a factor of about 2 than in the one-dimensional case discussed above; this appears to be mainly due to the assumed equation of state, however. The time evolution of the vertical impact-pressure distribution and of the avalanche surface were also obtained with this essentially fluid-like material. Lang et al. (1979) modelled snow as a viscous Newtonian fluid and obtained fairly realistic impact pressure distributions from two-dimensional numerical simulations.

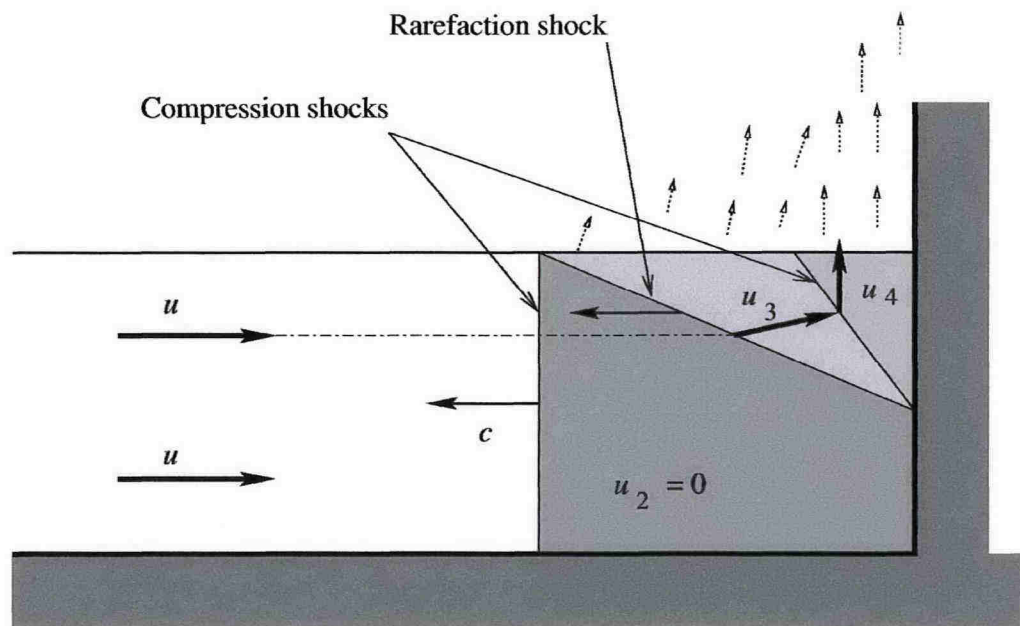


Figure 15: Scenario for the formation of compression and rarefaction shocks in the impact of an avalanche onto a rigid wall.

The main difference from the shock-tube problem is that the upper confining wall is no longer present so that the pressure at the upper surface is the atmospheric pressure. Inside the compressed snow, however, large normal stresses perpendicular to the flow direction are built up. As a consequence, the surface particles are ejected more or less vertically (see Figure 7 in (Salm, 1964) for an instructive photograph). This is the beginning of a rarefaction wave that propagates upstream and down into the compressed snow, as indicated in Figure 15. The speed of the rarefaction front and its inclination angle can in principle be calculated from the equation of state if the pressures on both sides of the shock are assumed known (namely, the pressure behind the

compressive shock front and atmospheric pressure, respectively). Across the rarefaction shock the snow particles are accelerated from rest in an oblique direction. It appears likely that another compression shock forms, starting out from the wall, across which the snow is decelerated again as it changes direction.

When the rarefaction front reaches the ground and moves away from the wall, the flow in the triangular area indicated in Figure 16 may cease and give rise to a growing deposit. If the avalanche flowed at constant discharge for a sufficiently long time, the deposit would grow until it reached the height of the wall. The volume of the deposit would then be determined by the properties of the rarefaction shock, more specifically by the deflection angle across the front. Detailed scrutiny of this rather speculative scenario must be left to future work.

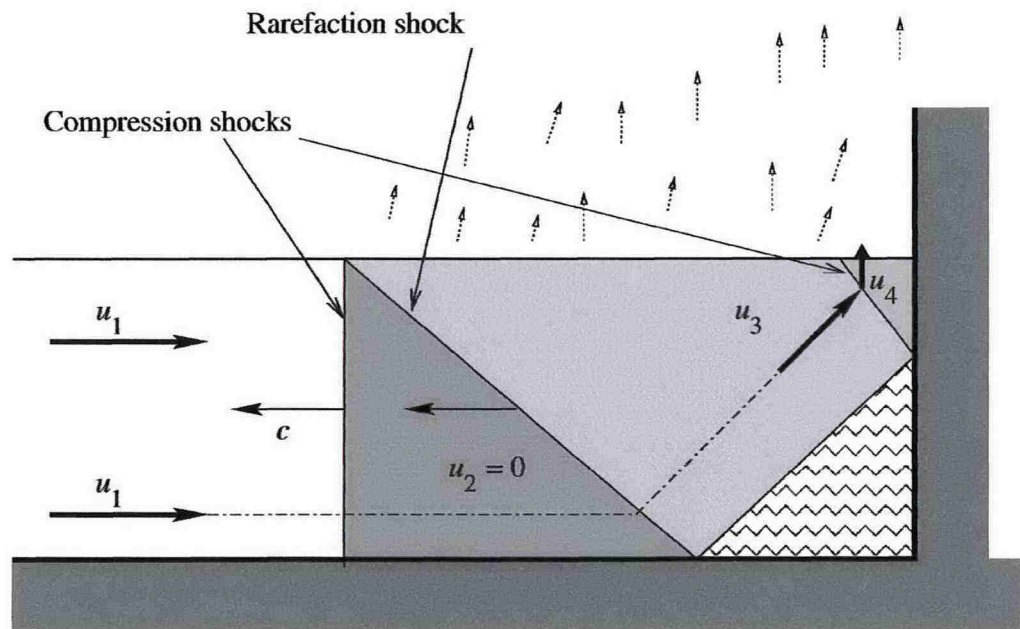


Figure 16: Later stage of avalanche impact on a rigid wall. The rarefaction shock front has reached the bottom of the avalanche. Snow crossing that front is deflected upward, leaving a growing area of stopped snow at the bottom of the wall. Secondary compression front (at the wall) is forced to move upwards.

To conclude this section, let us briefly explore a different approach, emphasising the solid-like properties of snow rather than its fluid-like behaviour. We consider this approach not as contradicting the fluid point of view, but rather as complementary to it. It is based on the observation that failure planes are often observed in avalanche deposits—snow possesses an inherent strength, due to cohesive and frictional forces. The impact of an

avalanche on a (vertical) dam is considered analogous to an essentially uniaxial, rapid compression test of a soil sample. (The avalanche represents only half of the sample, the ground can be considered a symmetry plane if gravitational forces are not important.)

As discussed above, the longitudinal normal stress becomes very large during compression, whereas the normal stress perpendicular to the ground, essentially given by the overburden weight, and the lateral normal stress are about two orders of magnitude smaller. From Mohr's circle of stress (Figure 17) one concludes that failure of the snow mass has to occur early on in the extremely short interval associated with the passage of the compressive shock. If the failure behaviour of snow may be approximated by the Mohr-Coulomb criterion even under such conditions, the failure plane is inclined at an angle of $\alpha = 45^\circ - \phi/2$ or about 30° to the flow direction. The cohesion of the snow is a few kilopascals at best and should not change the conclusion; however, this should be tested in experiments.

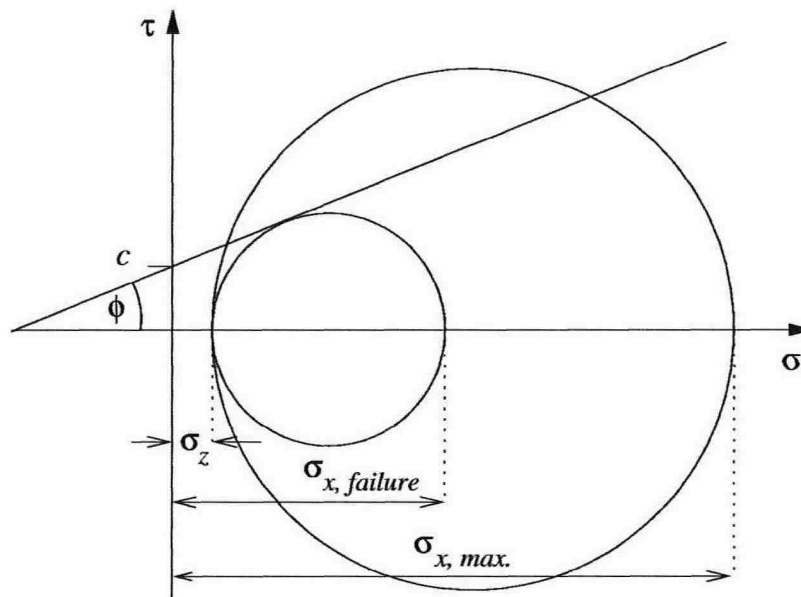


Figure 17 Mohr's circle for the impact of a material obeying the Coulomb friction law. ϕ is the friction angle, c the cohesion. The vertical normal stress, σ_z , due to the overburden load is much smaller than the maximal longitudinal stress, $\sigma_{x, \max}$, thus failure will occur at $\sigma_{x, \text{failure}}$ early during stress build-up.

Applying blindly the methods of soil mechanics, developed for quasi-static processes, one expects the deposit to form a wedge inclined at $\alpha = 45^\circ - \phi/2$ to the ground. This prediction is at least not in open contradiction with the observations at Ryggfonn, as evidenced by the recorded profiles—even the



crescent shape of the majority of profiles can be explained qualitatively through the change of the terrain slope upstream of the dam. Furthermore, the snow deposited farthest upstream of the dam was likely brought there by the tail of the avalanche, and thus at lower velocity where locking occurs and the effective friction angle might grow. If this is indeed the case, α is reduced.

An important consequence for dam design follows immediately if these considerations are true: The retention capacity per unit width of a dam, A , that deflects avalanches by an angle $\Delta\theta$ is approximately given by

$$A = \frac{1}{2} H_{dam}^2 \cdot (\cot(45^\circ - \phi/2) - \cot \Delta\theta). \quad (29)$$

This becomes rather small if ϕ happens to be below 30° in an avalanche and the dam was constructed with a β below 40° . Figure 18 illustrates how strongly the retaining capacity grows, according to (29) as the steepness of the dam front is changed.

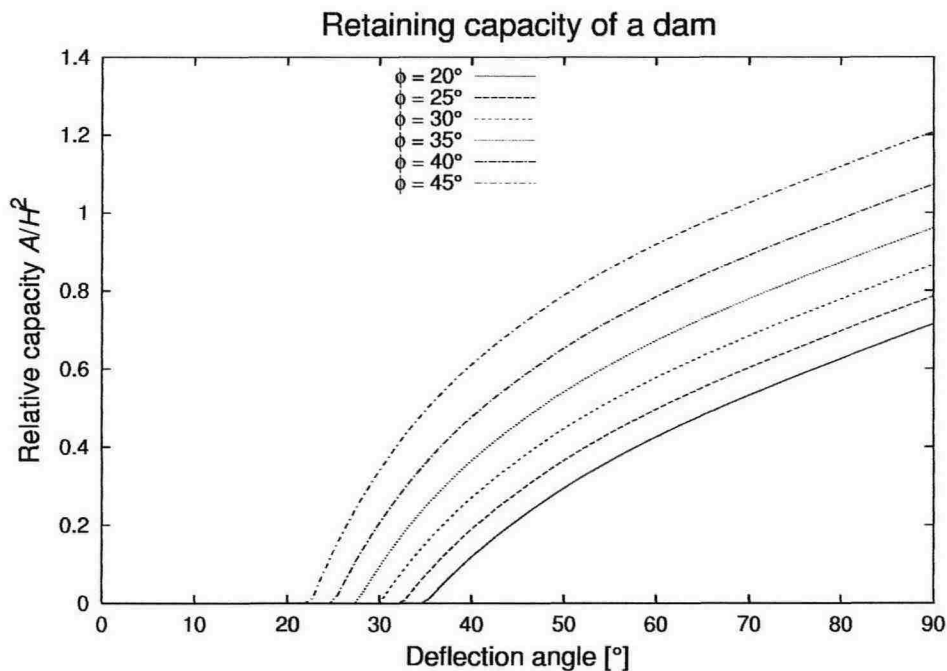


Figure 18: Approximate retaining capacity of a dam as a function of the deflecting angle, $\Delta\theta$, for different values of the static friction angle, ϕ , according to (29). The retaining capacity is scaled by the square of the dam height.



We stress again that these results are very preliminary and need to be backed up by a much more thorough study. The limits of applicability need to be carefully checked for both the gas dynamics and the soil mechanics approaches. In the first case, the viability of the presented scenario with compression and rarefaction shocks needs to be verified and more realistic equations of state developed and applied. On the other hand, the inertial forces have to be taken into account in the soil-mechanics approach. Imaginative experimental investigations at the laboratory scale with different materials—including snow—and at Ryggfonn will be very important for guiding future theoretical work.

7 CONCLUSIONS

It is underlined that the results presented above depend strongly on simulations with the NIS model, and in particular on the simulated avalanche velocity at the dam location. Given that this velocity has been measured neither upstream nor downstream of the dam, the figures obtained for the energy loss must be considered preliminary.

The average energy loss of 23 % presented in Table 2 is, in our opinion, a realistic number for the actual energy loss at the Ryggfonn dam. The λ -factor of 1.53 (35 % energy loss) described in Table 5 is a somewhat higher loss. This discrepancy between two different calculation methods may partly be explained by the 'chain' effect included in the NIS model, where the rear part of the avalanche pushes the front part upwards on the dam and tends to spread the energy loss to a larger part of the avalanche body. This effect is probably also found in nature. In the calculation of the λ -factor according to (22) and (23) no such effect is taken into account, which indicates that the λ -factor is somewhat high. Additionally, the calculations entering Table 2 involve avalanches flowing over the dam; the reduced frictional force in the bends at the dam crown offsets a significant part of the energy loss in the bend at the base. When calculating the ascending height on a sufficiently large dam, only the lower bend enters the energy balance.

An interesting result from our simplistic theoretical approach, based on the notion of an effective dry-friction coefficient, is that a major contribution to the energy dissipation at the dam is induced by the increased friction in the bottom bends (partly offset by reduced friction in the crown bends). The relative energy loss (in terms of the initial energy) due to this effect is proportional to the dam height and avalanche mass, and inversely proportional to the specific kinetic energy. The other major contribution to energy dissipation, due to the snow masses piling up in front of the dam, is proportional to the square of the



dam height and the specific kinetic energy, but largely independent of the avalanche mass.

Further studies based on more comprehensive measurements and on calculations including the effects of lateral spreading of the avalanche mass, compression of the avalanche snow against the dam and the volume of the avalanche snow are needed.

8 REFERENCES

- Bagnold, R. A. 1954. Experiments on a gravity free dispersion of large solid spheres in a Newtonian fluid under shear. *Proc. Royal Soc. (London)*, Ser. **A225**, 49–63.
- Bartelt, P. and Salm, B. 1998. A short comparison between Voellmy-fluid and Criminale-Ericksen-Filby fluid dense snow avalanche models. *Norwegian Geotechnical Institute, Publication No. 203*.
- Criminale, W. O. jr., Ericksen and Filby, G. L. 1958. Steady shear flow of non-Newtonian fluids. *Archive Rat. Mech. Anal.* **1**, 410–417.
- Harbitz, C. B. 1998. A survey of computational models for snow avalanche motion. *NGI report 581220-1, December 1998*.
- Irgens, F. 2000. Simplified simulation model of snow avalanches and landslides. *Technical report, 20th International Congress for Theoretical and Applied Mechanics, Chicago, USA, 2000*.
- Kristensen, K. and Larsen, J. O. 1996. The Ryggfonn avalanche dynamics project. *Proc. International Snow Science Workshop ISSW '96, Banff, Canada*.
- Kristensen, K. 1992–2000: The Ryggfonn project. Avalanche data from the winters 1991/92, 1992/93 and 1993/94. 1996/97, 1997/98, 1998/99 and 1999/200. *NGI reports 581200-33 2001*.
- Lied, E. 1999. Upgrading instrumentation in Ryggfonn. *Technical note. NGI 1998*.
- Lied, K. 1985. Earth dams for protection against snow avalanches. *NGI report 58120-4*.
- McClung, D. and Mears, A. 1995. Dry flowing avalanche run-up and run-out. *Journal of Glaciology* **41**(138), 359–372.
- Rammer, L., Schreiber, H., Randeu, W. L., Kristensen, K., and Lied, K. 1998. Radar measurements of snow avalanche full-scale experiment in Ryggfonn. *25 Years of Snow Avalanche Research, Conference Proceedings, Norwegian Geotechnical Institute, Publication no. 203*.



- Norem, H., Kvisterøy, T., and Evensen, B. D. 1985. Measurements of avalanche speeds and forces. Instrumentation and preliminary results of the Ryggfonn project. *Annals of Glaciology* **6**, 19–22.
- Norem, H. and Kristensen, K. Tronstad K.: The Ryggfonn project. Avalanche data from the winter 1982/83 – 1989/90. *NGI reports 58120-06-21*,
- Norem, H., Irgens, F. and Schieldrop, B. 1987. A continuum model for calculating snow avalanche velocities. In: *Avalanche Formation, Movements and Effects—Symposium at Davos 1986*, IAHS publication **162**, 363–378. Also in: Norwegian Geotechnical Institute, report 58120-9.
- Perla, R., Cheng, T. T., and McClung, D. M. 1980. A two-parameter model of snow-avalanche motion. *J. Glaciol.* **26**(94), 197–207.
- Bartelt, P., Salm, B. and Gruber, U. 1999 Calculating dense-snow avalanche runout using a Voellmy-fluid model with active/passive longitudinal straining. *Journal of Glaciology* **45**(150), pages 242-254.
- Eglit, E. M. 1983. Some mathematical models of snow avalanches. In: *Advances in the Mechanics and the Flow of Granular Materials*, Vol. II, M. Shahinpoor (ed.), 577–588. Trans Tech Publications, Clausthal-Zellerfeld, Germany.
- Hungr, O., and McClung, D. M. 1987. An equation for calculating snow avalanche run-up against barriers. *International Association of Hydrological Sciences Publication* **162** (Symposium at Davos 1986—*Avalanche Formation, Movements and Effects*), 475–508.
- Perla, R., Cheng, T. T., and McClung, D. M. 1980. A two-parameter model of snow-avalanche motion. *J. Glaciol.* **26** (94), 197–207.
- Briukhanov, A. V., Grigorian, S. S., Miagkov, S. M., Plam, M. Ya., Shurova, I. Ya., Eglit, M. E. and Yakimov, Yu. L. 1967. On some new approaches to the dynamics of snow avalanches. In: *Physics of Snow and Ice, Proc. of the Intl. Conf. on Low Temperature Science*, Sapporo, 1966. H. Ôura (ed.), Vol. 1, Part 2, 1223–1241. The Institute of Low Temperature Science, Hokkaido University, Sapporo, Japan.
- Bozhinskiy, A. N. and Losev, K. S. 1998. *The Fundamentals of Avalanche Science*. Translated by C.E. Bartelt. *Mitt. Eidgenöss. Inst. Schnee- Lawinenforsch.* **55**. Davos, Switzerland, 280 p.
- Gonor, A. L. and Pik-pichak, Ye. G. Numerical modeling of snow avalanche impact on a solid wall [in Russian]. *Izv. AN SSSR ser mekhanika zhidkosti i gaza* (1983) No 6 pages 86-91.
- Lang, T. E., Dawson, K. L. and Martinelli, Jr., M. 1979. Numerical simulation of snow avalanche flow. Research Paper RM-205, Rocky Mountains Forest and Range Experimental Station, Fort Collins, Colorado.
- Mellor, M. 1977. Engineering properties of snow. *J. Glaciol.* **19**(81), 15–66.
- Salm, B. 1964. Anlage zur Untersuchung dynamischer Wirkungen von bewegtem Schnee. *Z. angew. Math. Phys.* **15**, 357–375.



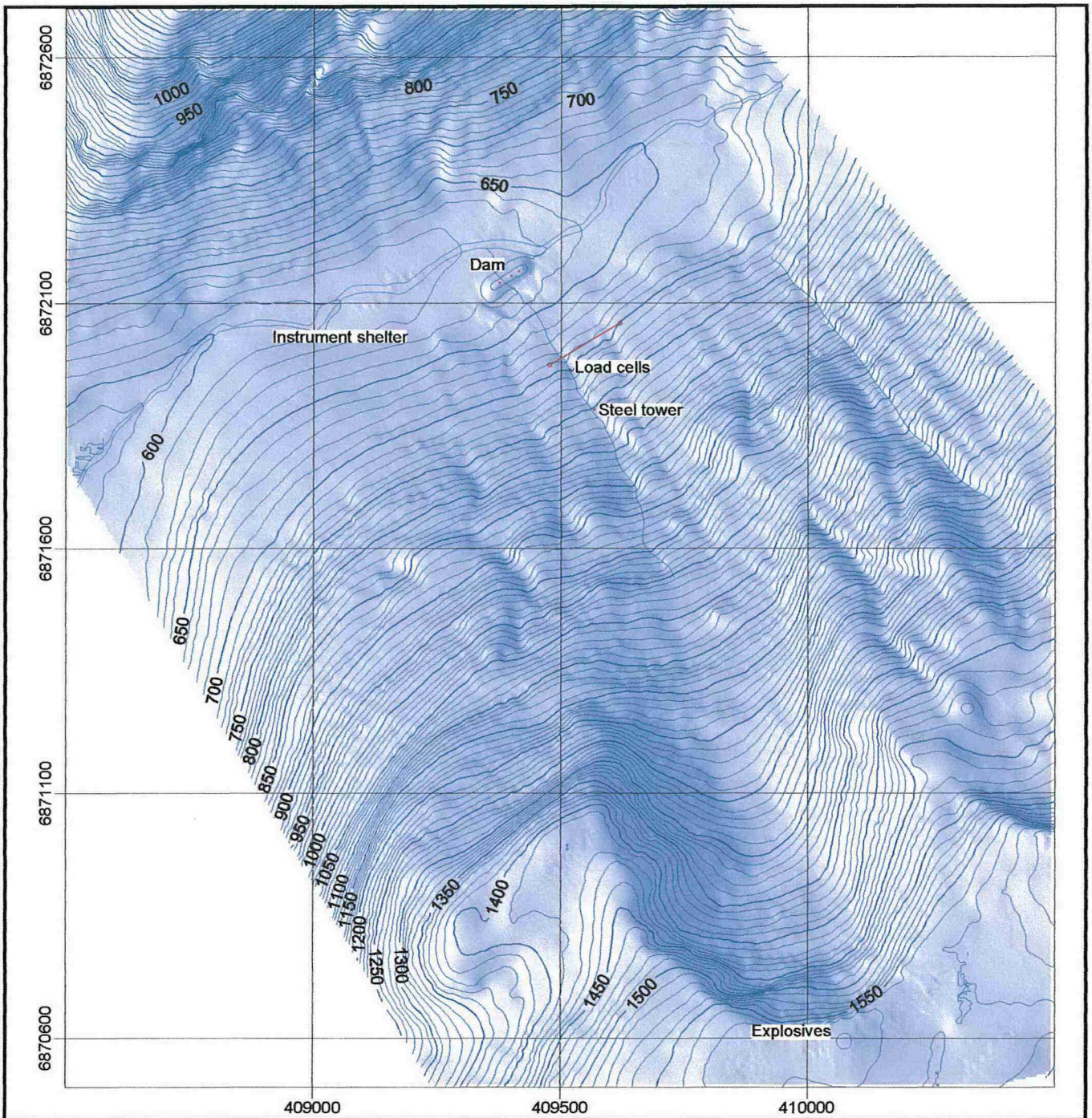
Schreiber, H., Randeu, W. L., Schaffhauser, H. and Rammer, L. 2001. Avalanche dynamics measurements by pulsed Doppler radar. *Annals Glaciol.* **32**, 275–280.


Issler, D. and Lied, K. 2001. EU-RTD proposal: SATSIE (Proposal submitted for financial support from the EC for shared-cost RTD actions: research and technological development projects, demonstration projects and combined projects). NGI report 20011001-4. Norges Geotekniske Institutt, Oslo, Norway, October 2001.

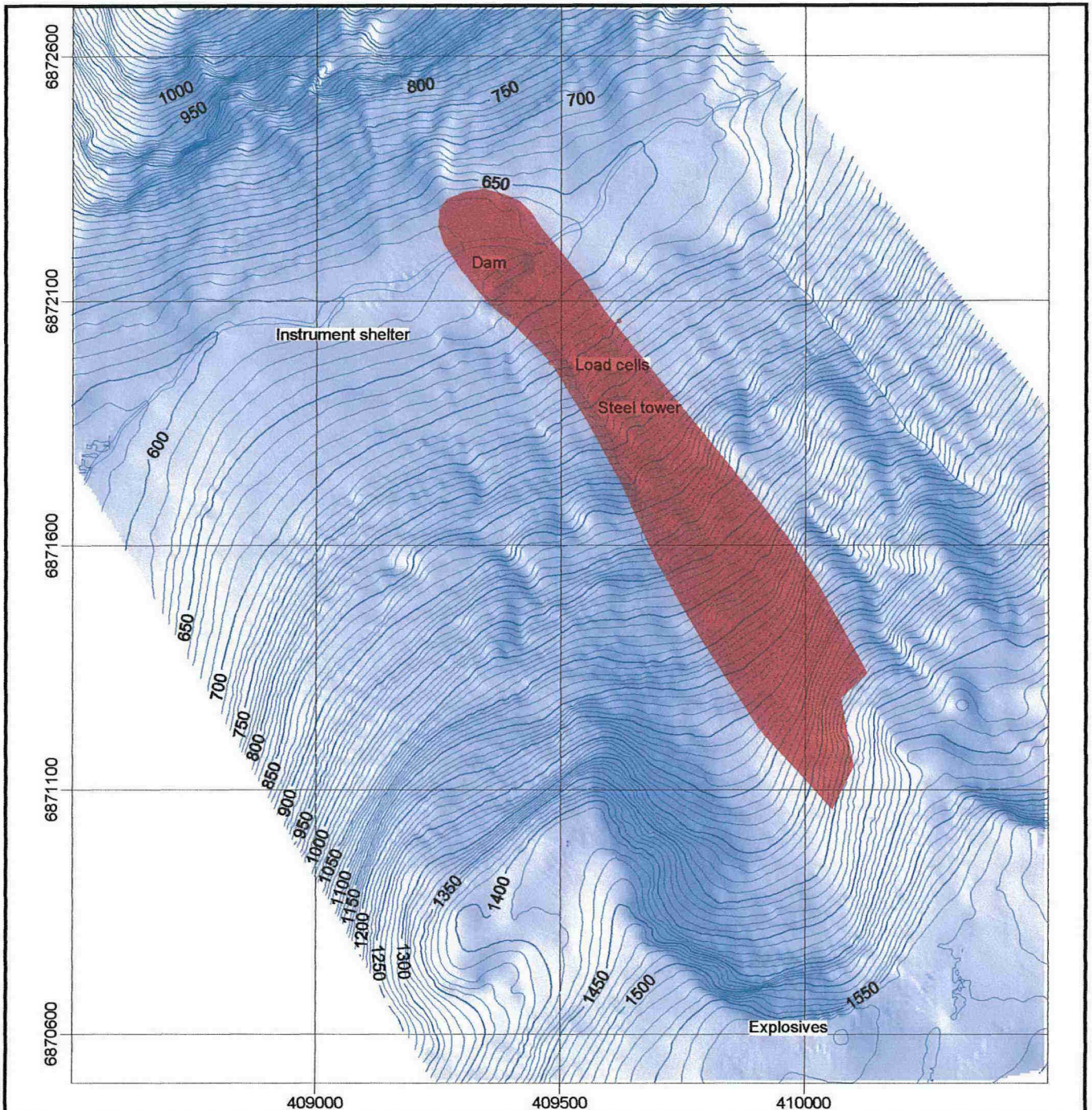



APPENDIX A

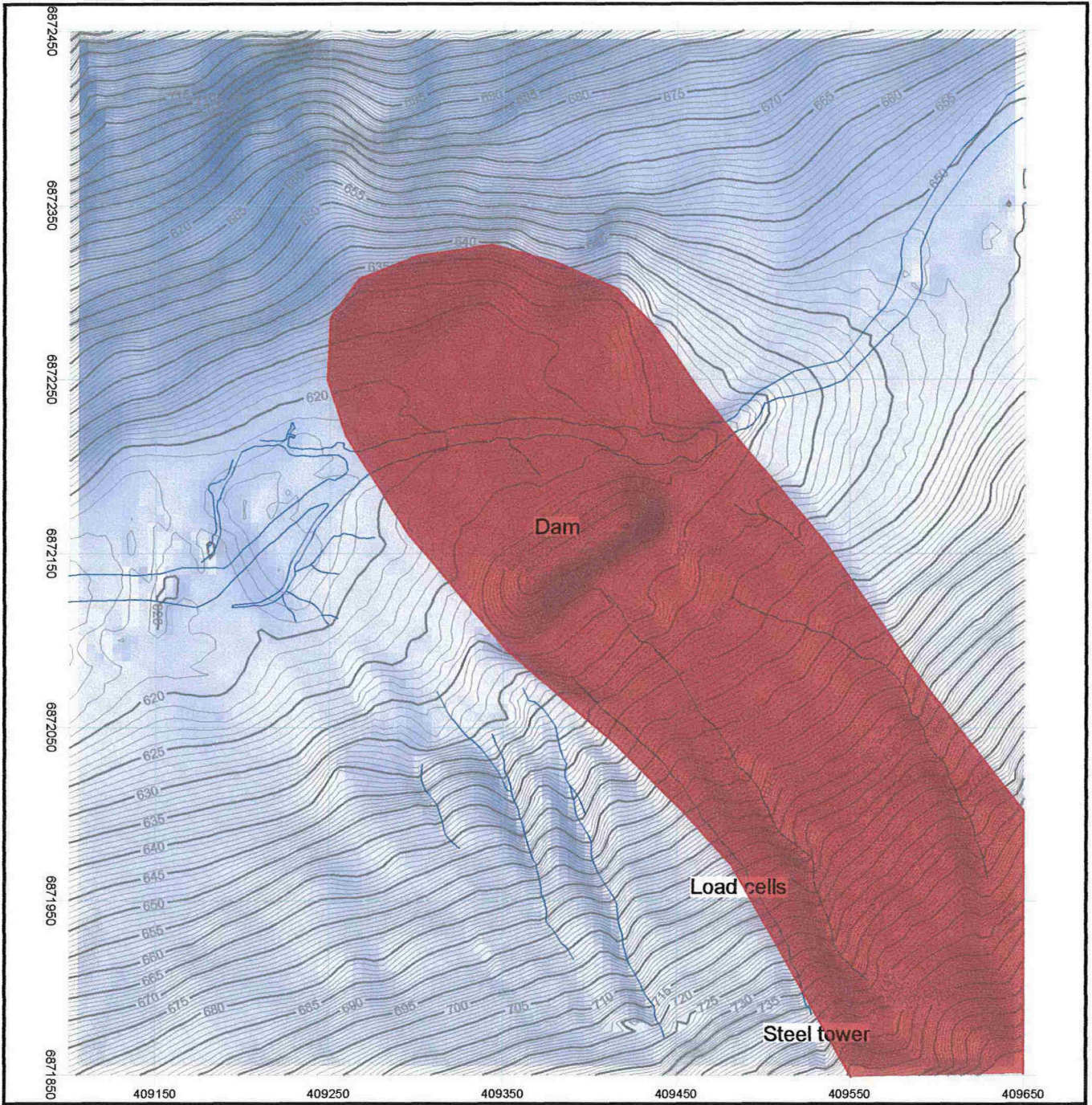
Figures 19-55




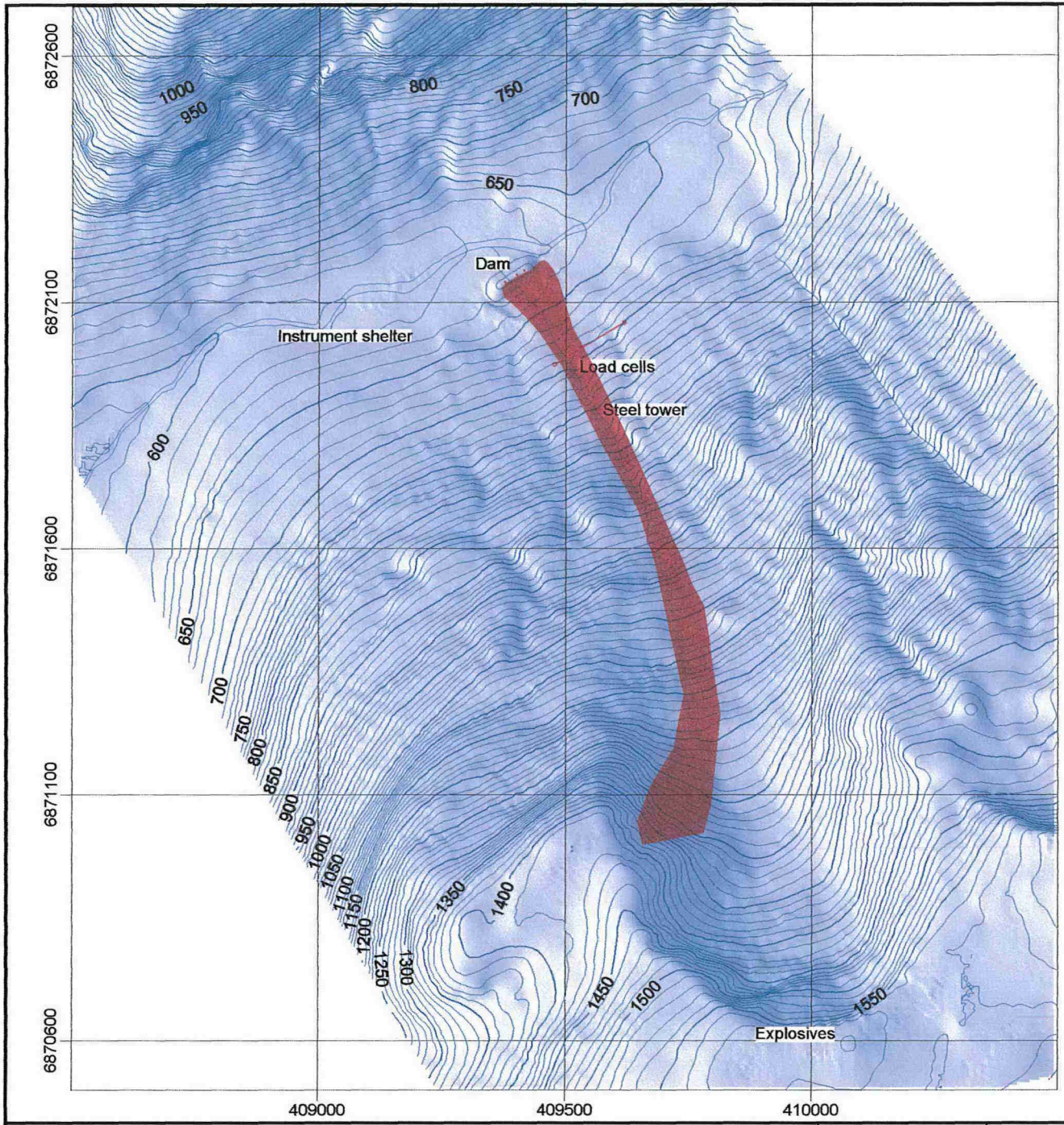
RYGGFONN	Report No. 581200-35	Figure 19
Overview map of the Ryggfonn avalanche area	Drawn by KKr/TG	Date 02-02-26
	Checked	
	Approved	




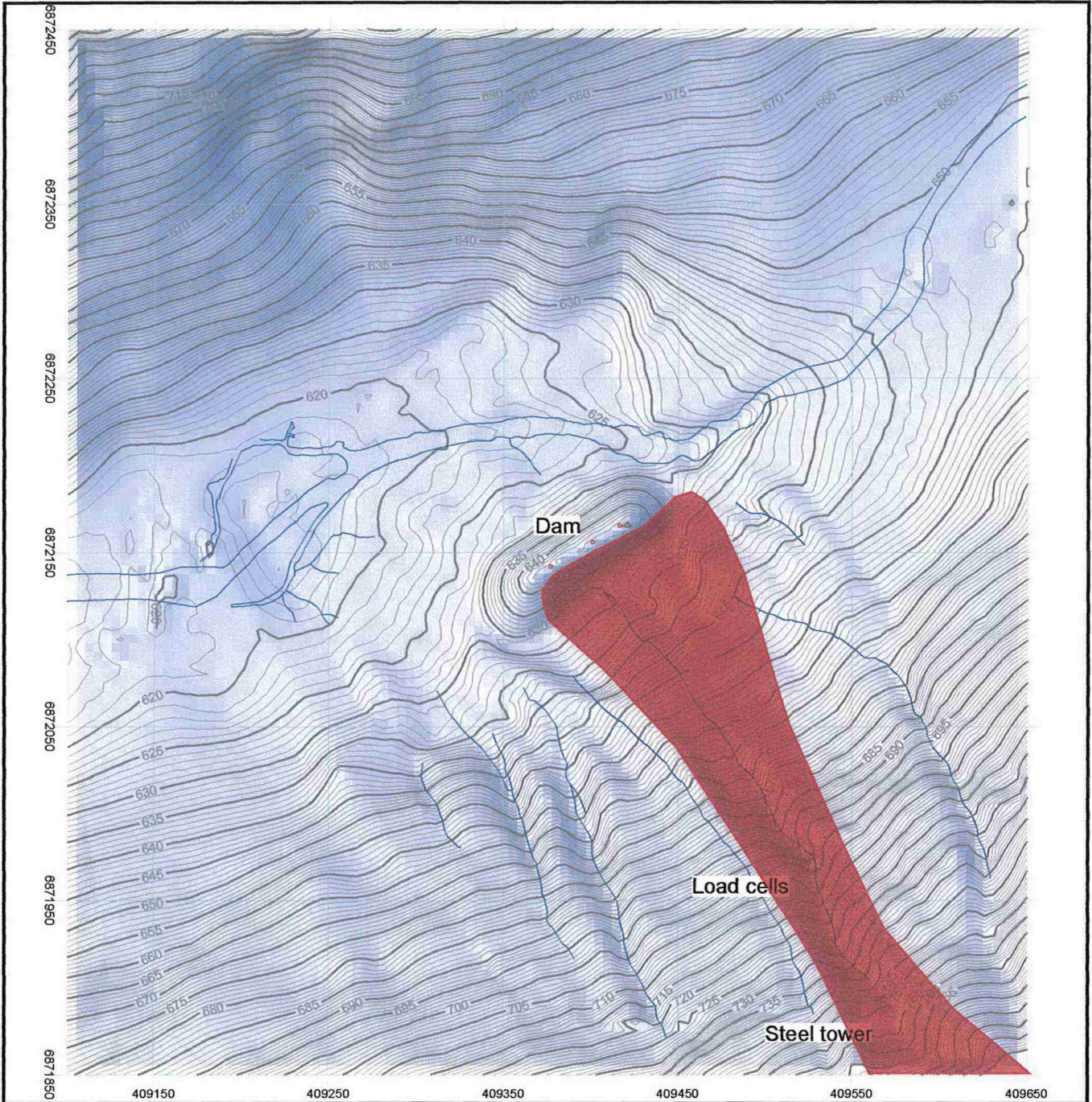
RYGGFONN	Report No. 581200-35	Figure 20
	Drawn by KKr/TG	Date 02-02-26
Overview map of avalanche 19830110	Checked	
	Approved	



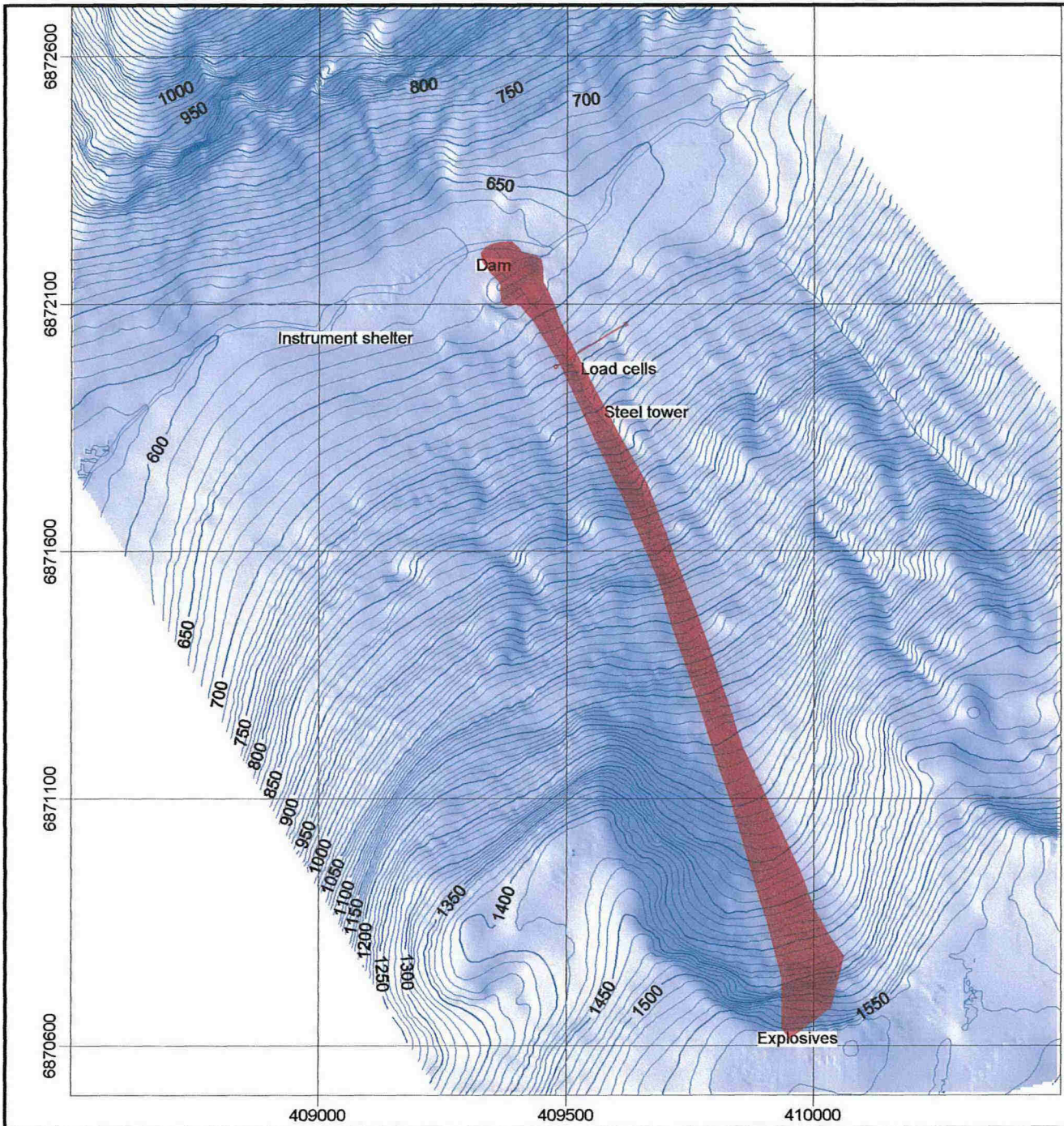
RYGGFONN	Report No. 581200-35	Figure 21
Detail map of avalanche 19830110	Drawn by KKr/TG	Date 02-02-26
	Checked	
	Approved	




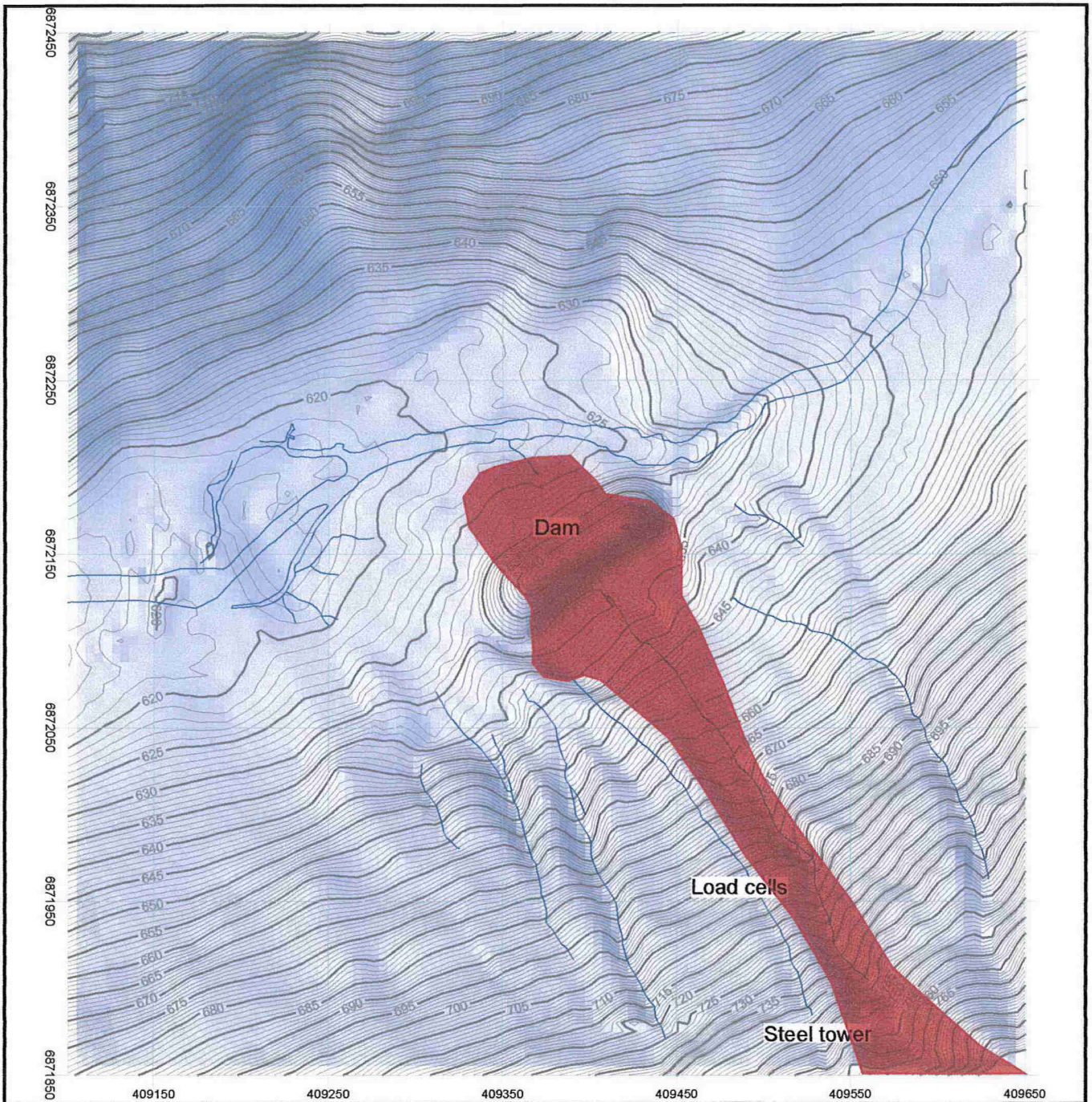
RYGGFONN	Report No. 581200-35	Figure 22
	Drawn by KKr/TG	Date 02-02-26
Overview map of avalanche 19830308	Checked	
	Approved	




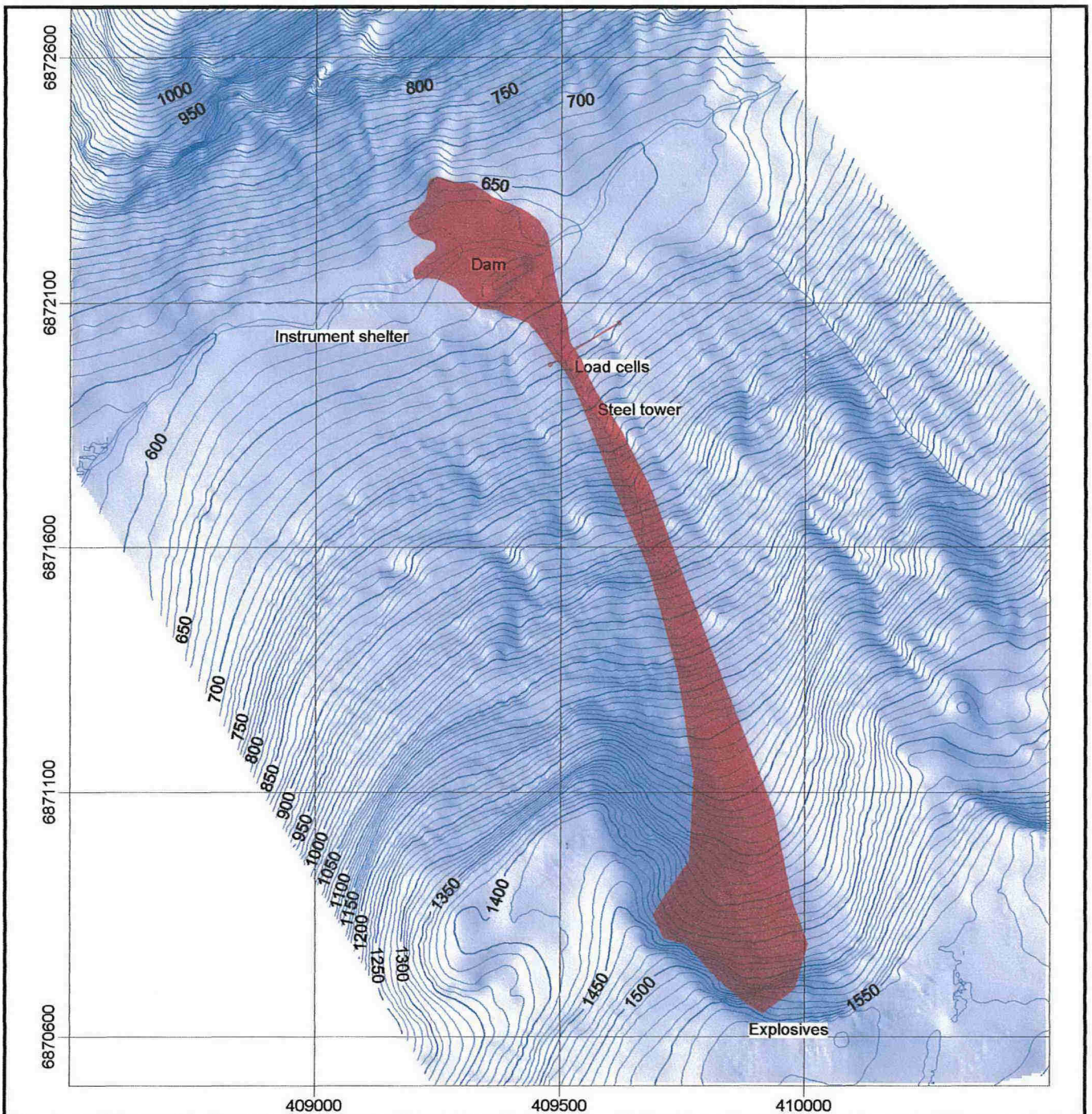
<p>RYGGFONN</p> <p>Detail map of avalanche 19830308</p>	Report No.	Figure
	581200-35	23
	Drawn by	Date
	KKr/TG	02-02-26
Checked		
Approved		




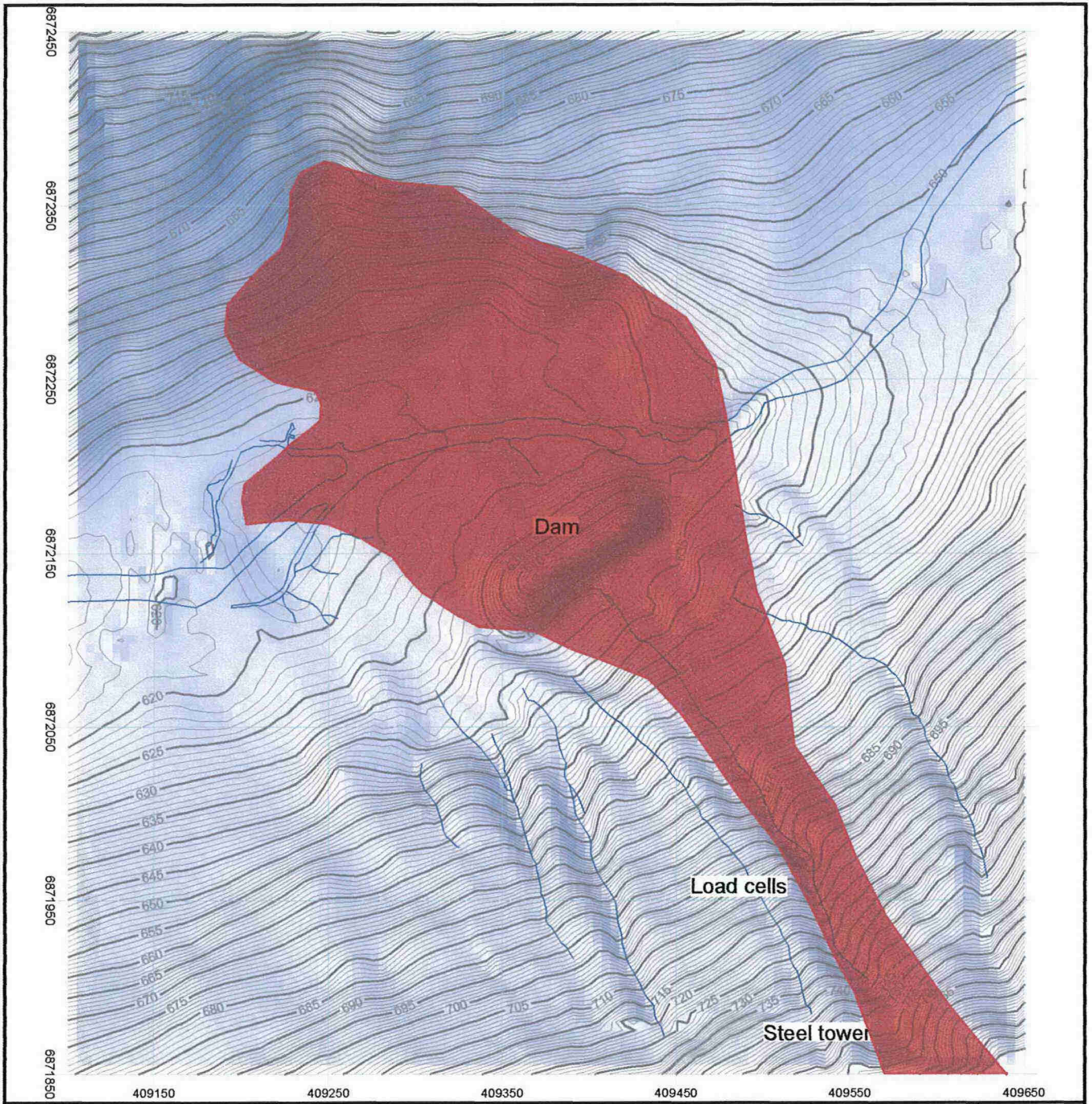
RYGGFONN	Report No. 581200-35	Figure 24
	Drawn by KKr/TG	Date 02-02-26
Overview map of avalanche 19850213	Checked	
	Approved	




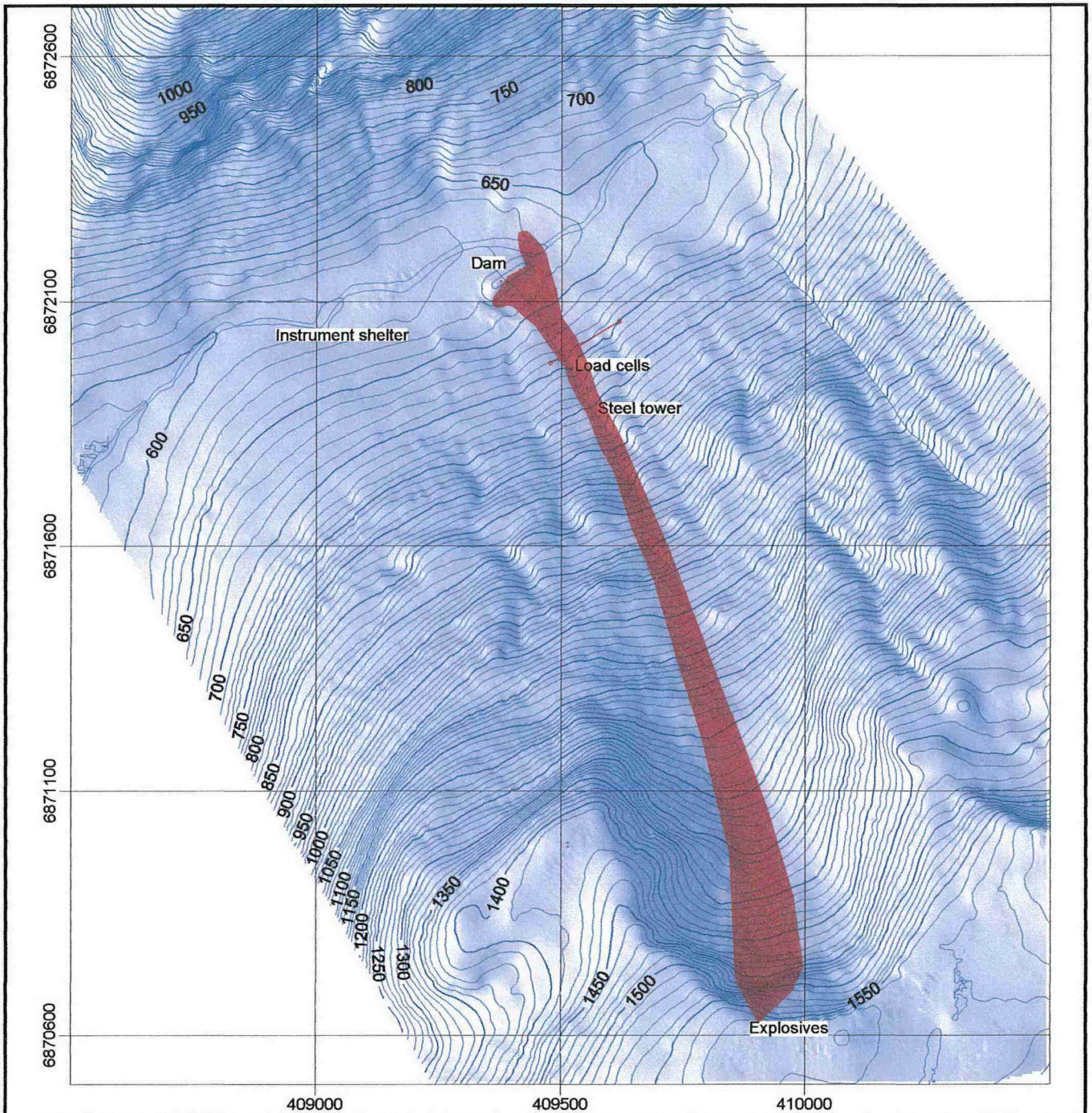
RYGGFONN	Report No. 581200-35	Figure 25
Detail map of avalanche 19850213	Drawn by KKr/TG	Date 02-02-26
	Checked	
	Approved	




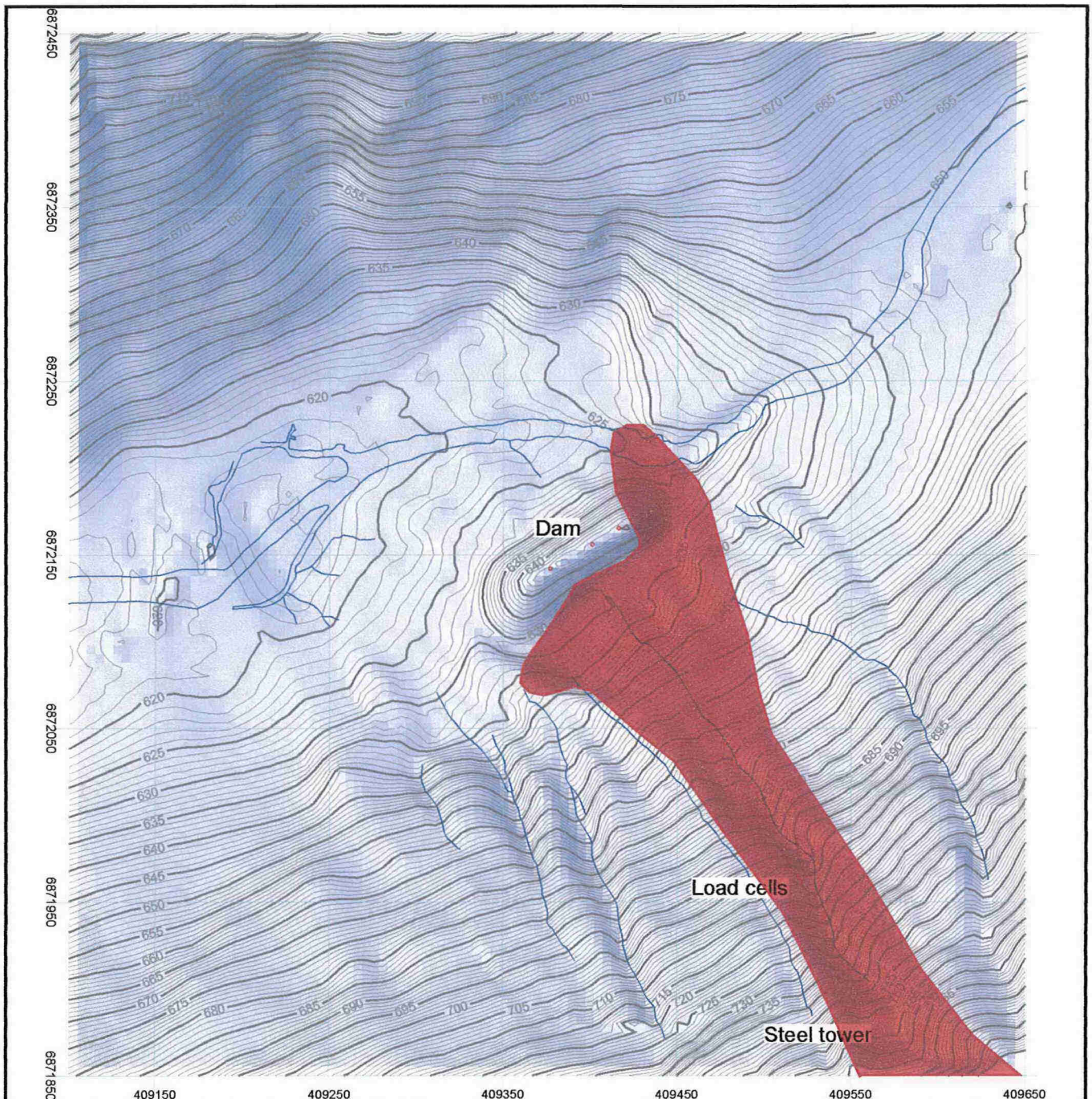
RYGGFONN	Report No. 581200-35	Figure 26
Overview map of avalanche 19870128	Drawn by KKr/TG	Date 02-02-26
	Checked	
	Approved	




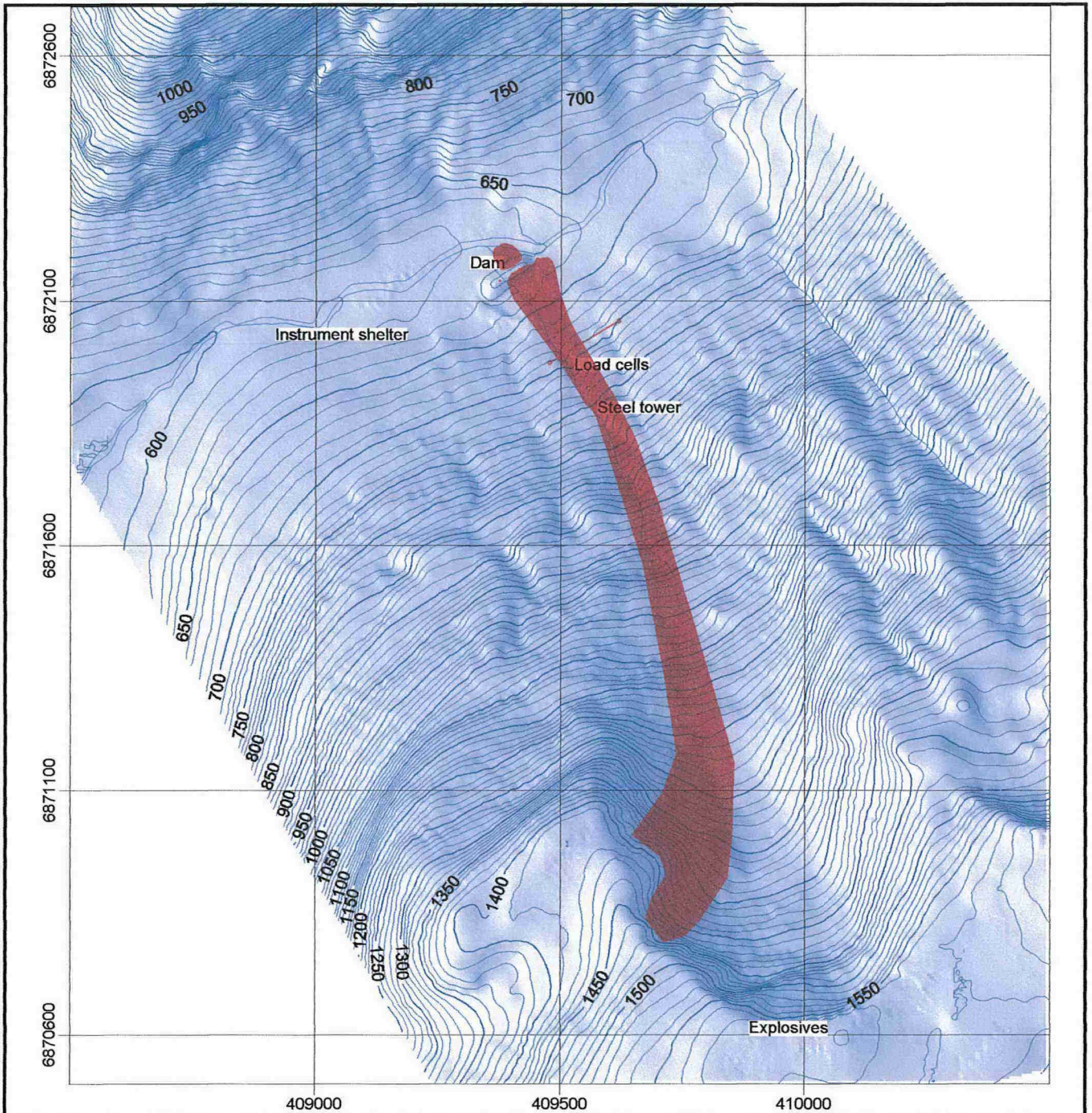
RYGGFONN	Report No. 581200-35	Figure 27
	Drawn by KKr/TG	Date 02-02-26
Detail map of avalanche 19870128	Checked	
	Approved	




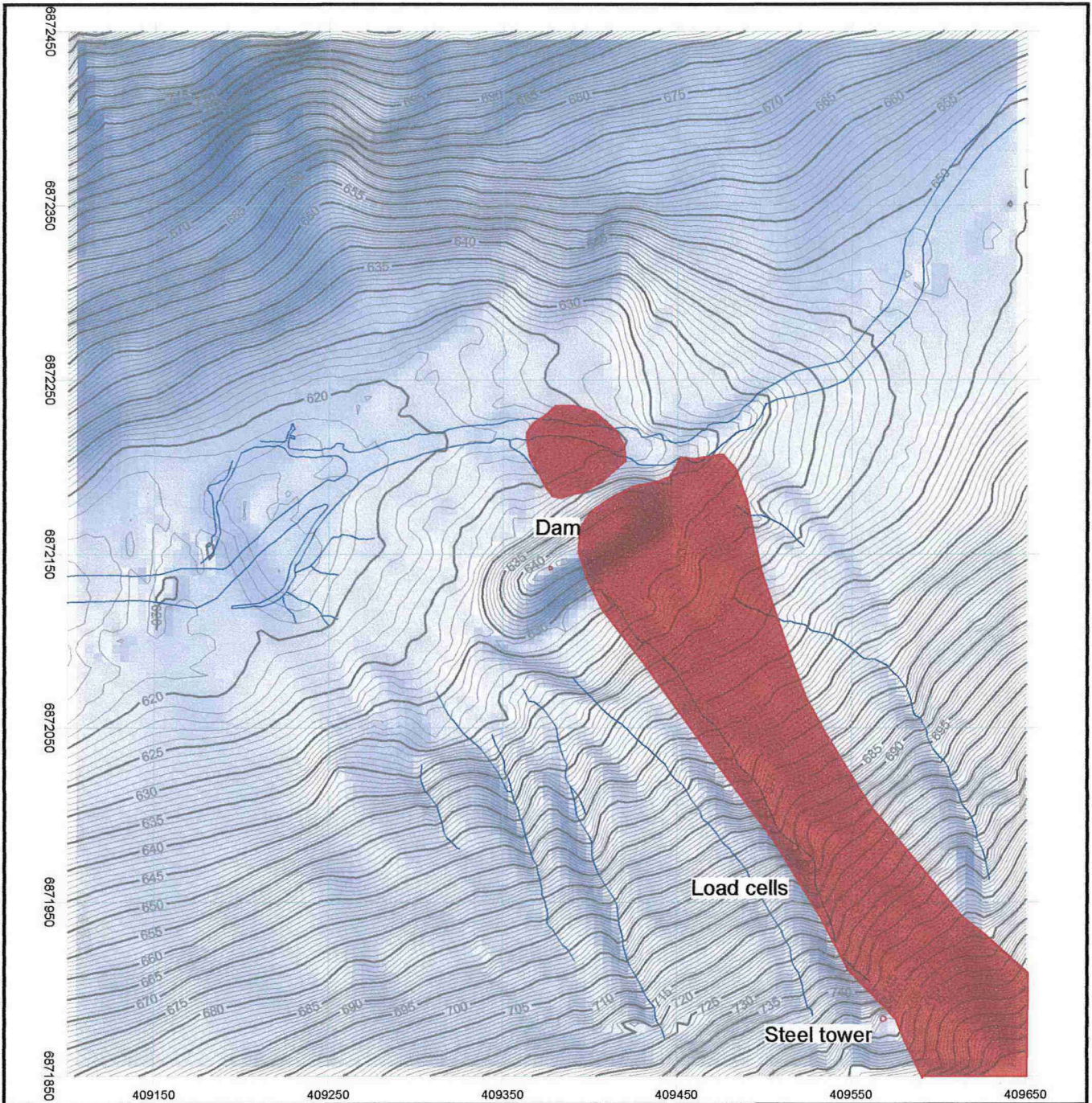
RYGGFONN	Report No. 581200-35	Figure 28
Overview map of avalanche 19880411	Drawn by KKr/TG	Date 02-02-26
	Checked	
	Approved	




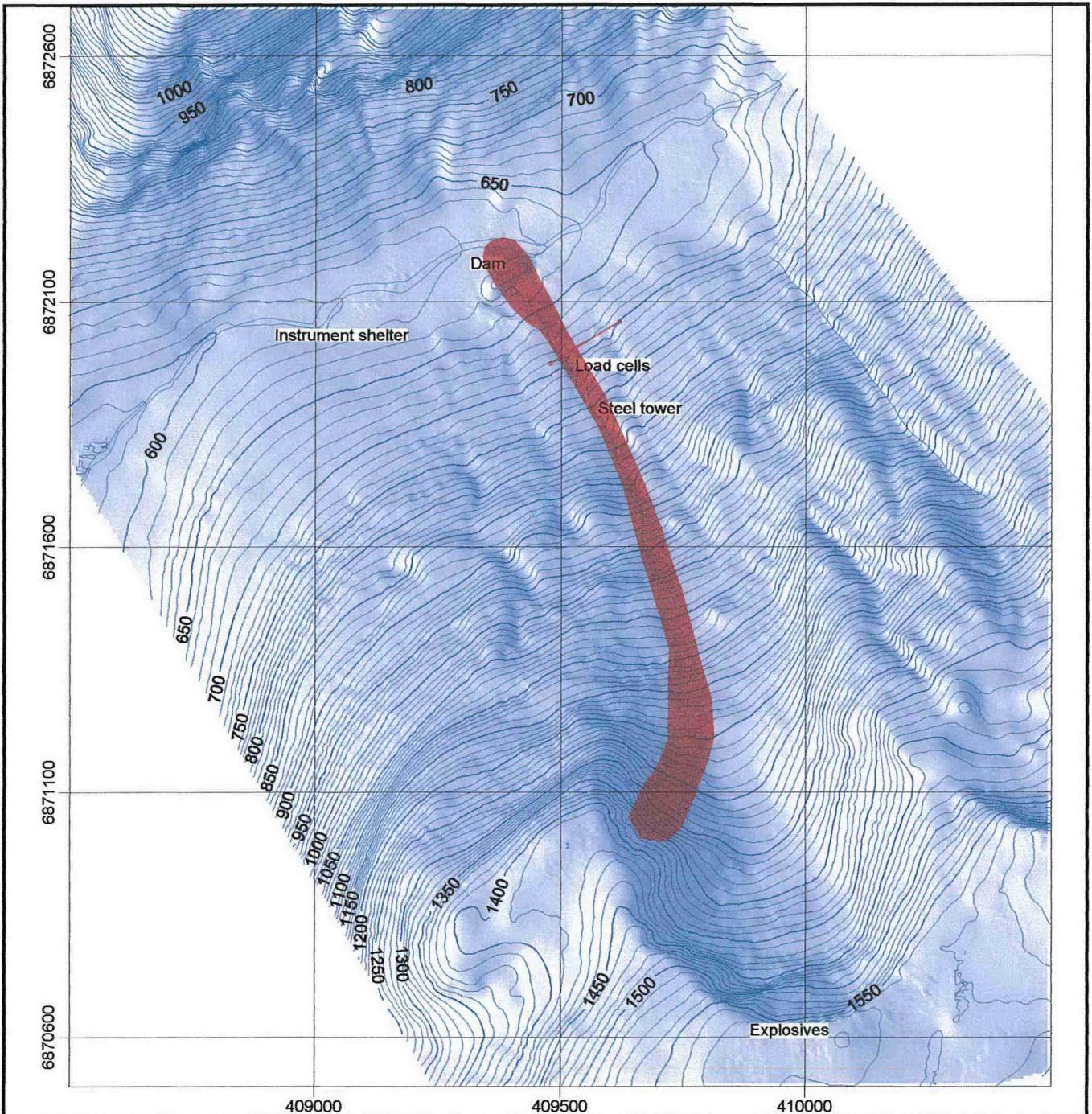
<p>RYGGFONN</p>	<p>Report No. 581200-35</p>	<p>Figure 29</p>
<p>Detail map of avalanche 19880411</p>	<p>Drawn by KKr/TG</p>	<p>Date 02-02-26</p>
	<p>Checked</p>	
<p>Approved</p>		




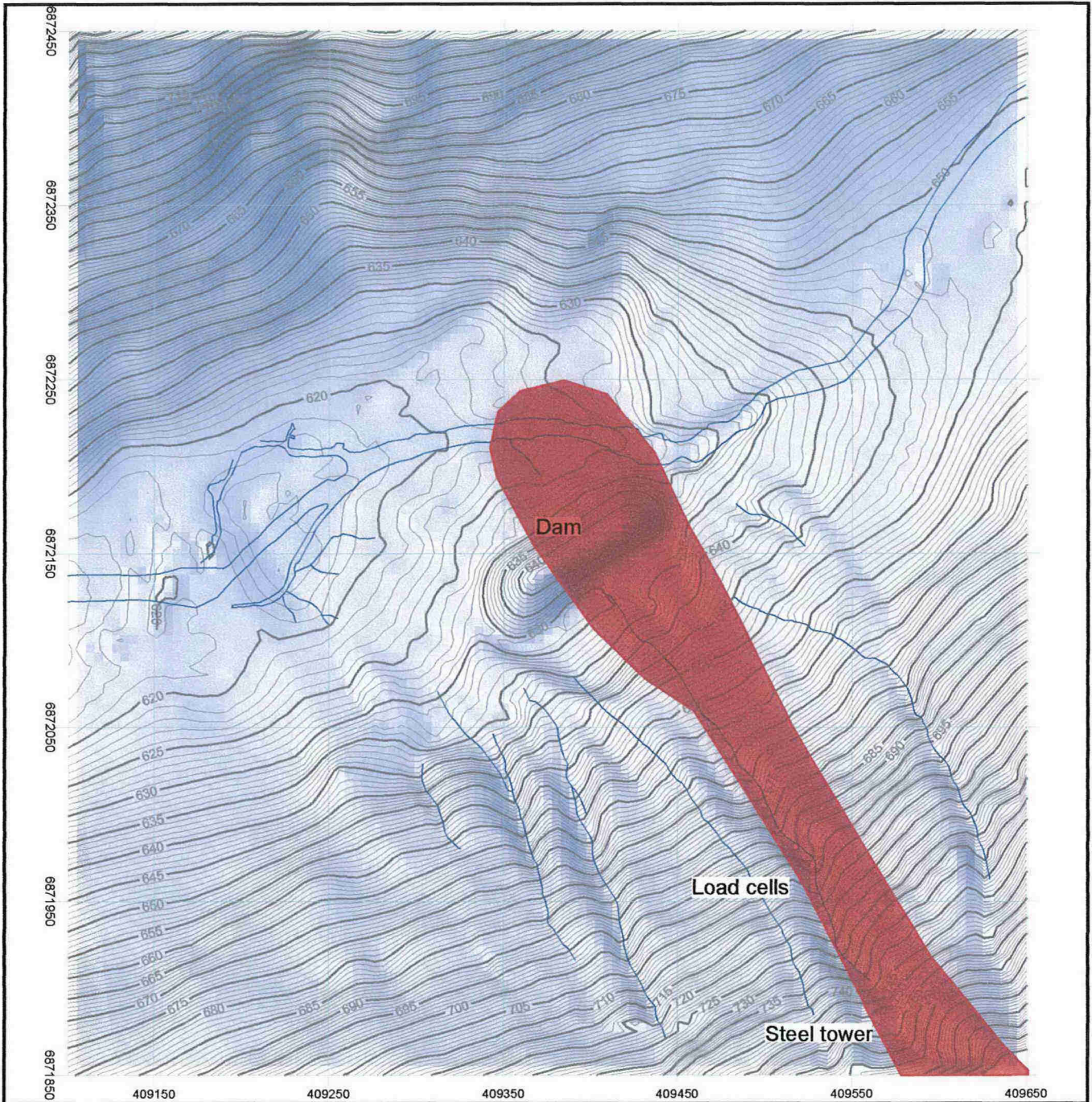
RYGGFONN	Report No. 581200-35	Figure 30
Overview map of avalanche 19881223	Drawn by KKr/TG	Date 02-02-26
	Checked	
	Approved	




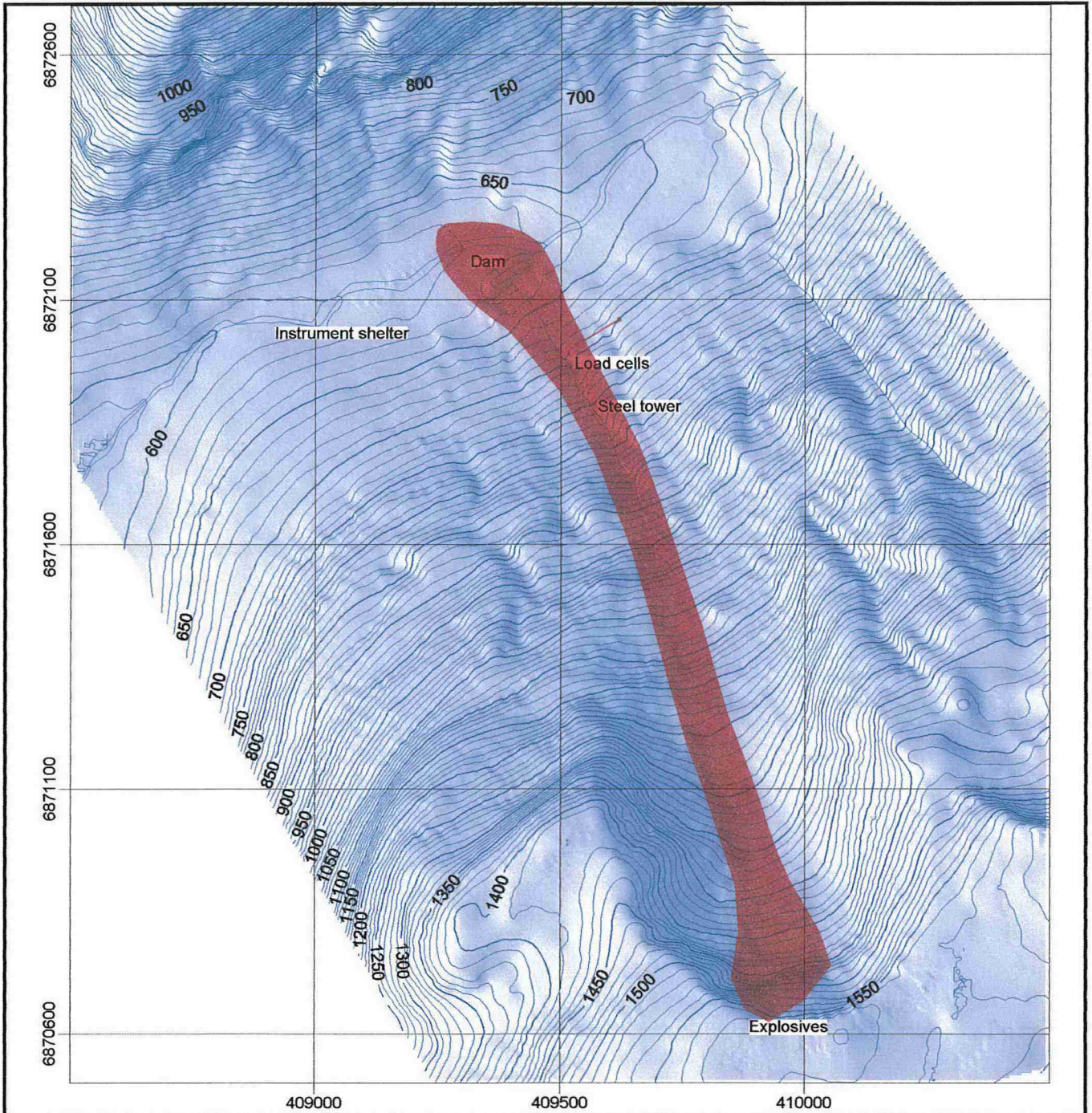
RYGGFONN	Report No. 581200-35	Figure 31
	Drawn by KKr/TG	Date 02-02-26
Detail map of avalanche 19881223	Checked	
	Approved	




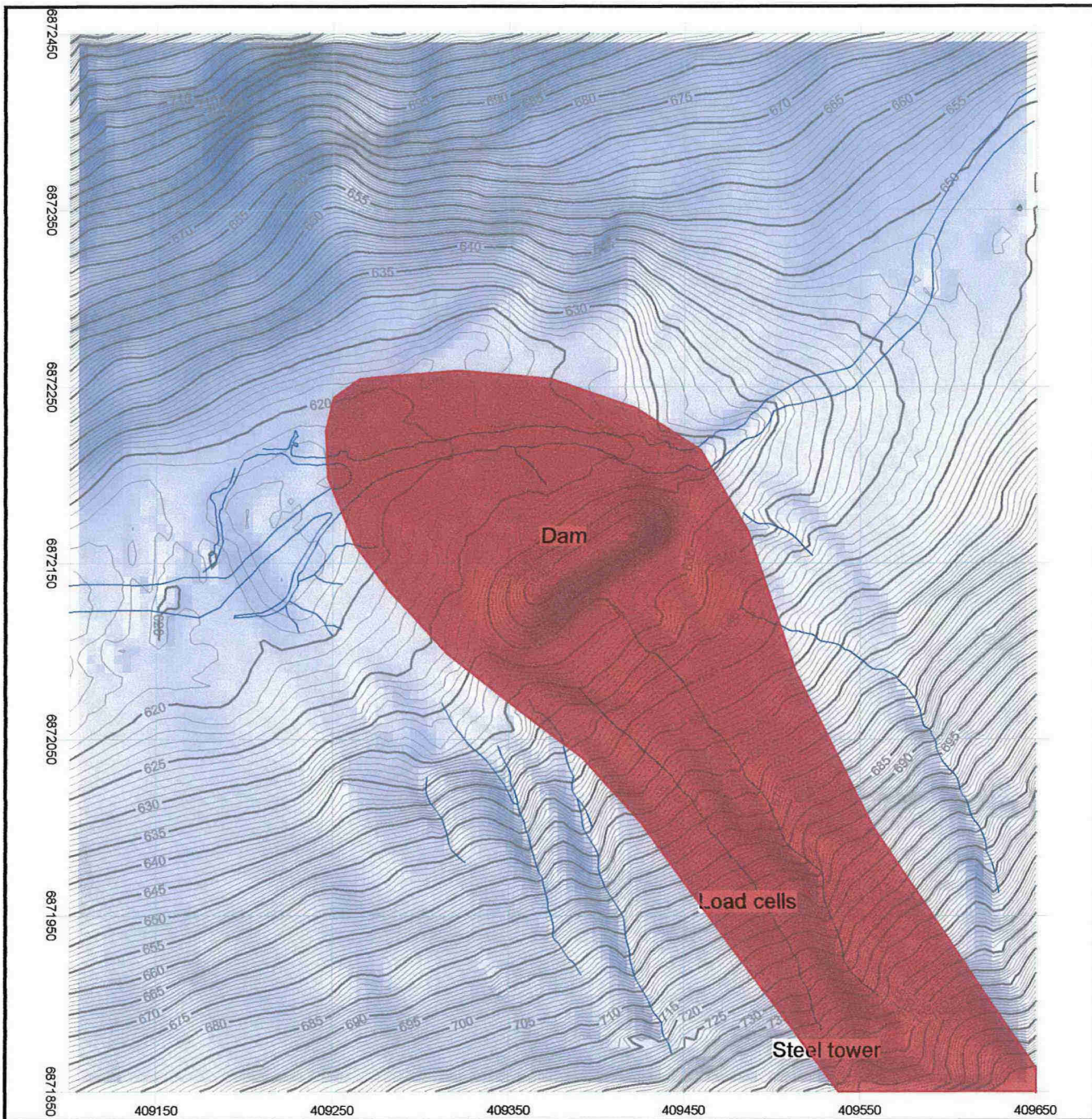
RYGGFONN	Report No. 581200-35	Figure 32
Overview map of avalanche 19900307	Drawn by KKr/TG	Date 02-02-26
	Checked	
	Approved	




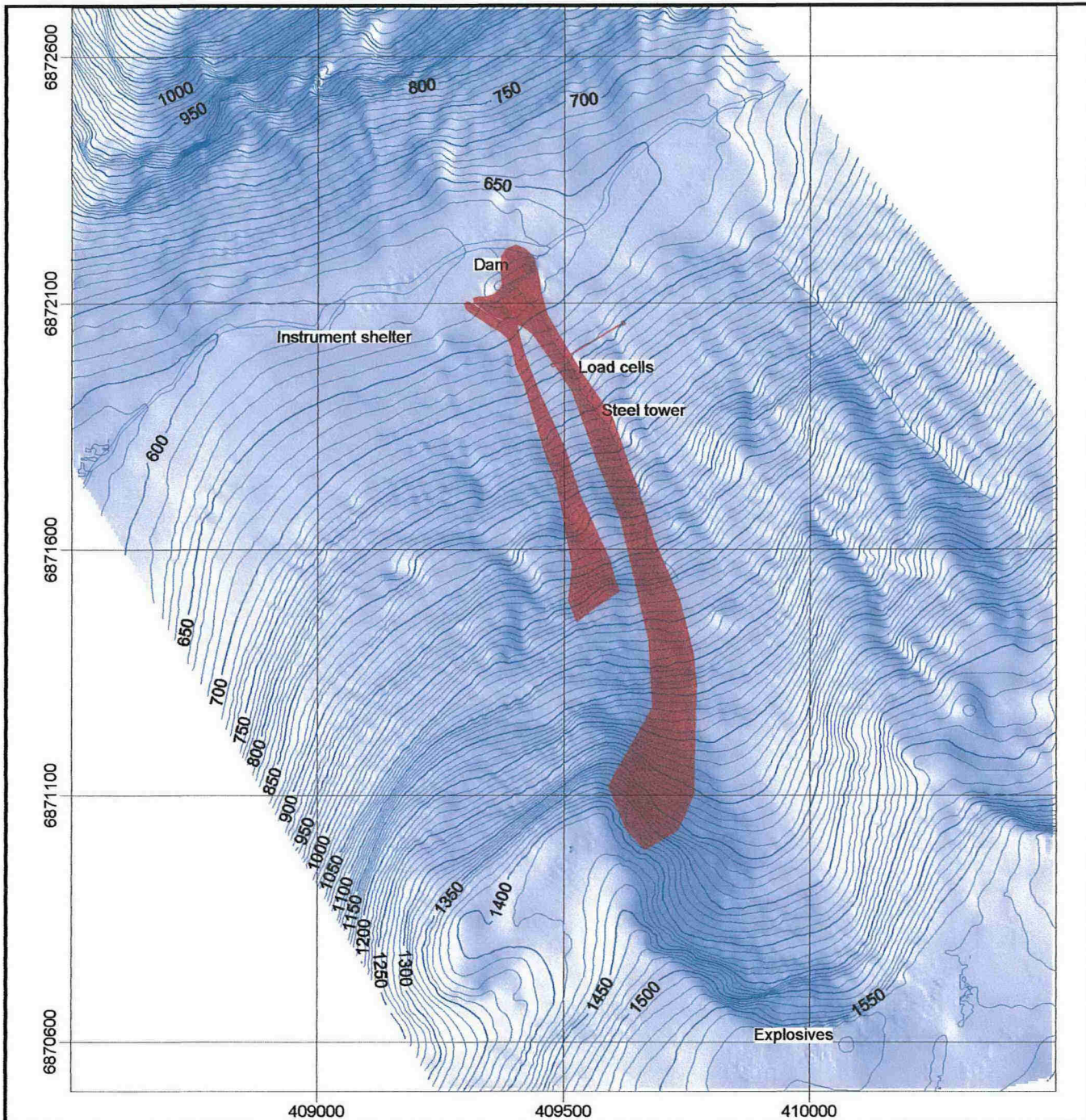
RYGGFONN	Report No. 581200-35	Figure 33
Detail map of avalanche 19900307	Drawn by KKr/TG	Date 02-02-26
	Checked	
	Approved	




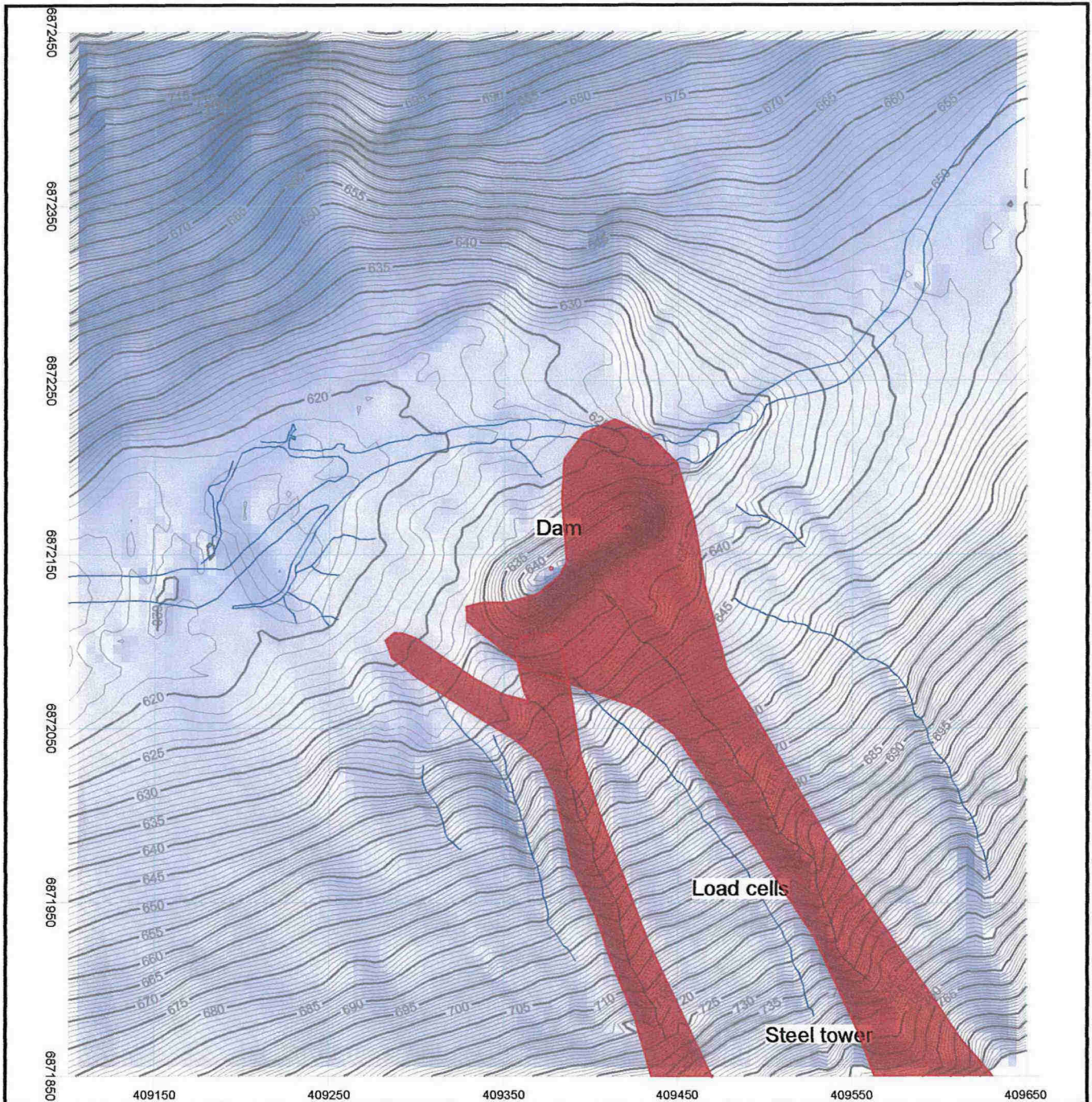
RYGGFONN	Report No. 581200-35	Figure 34
Overview map of avalanche 19930327	Drawn by KKr/TG	Date 02-02-26
	Checked	
	Approved	




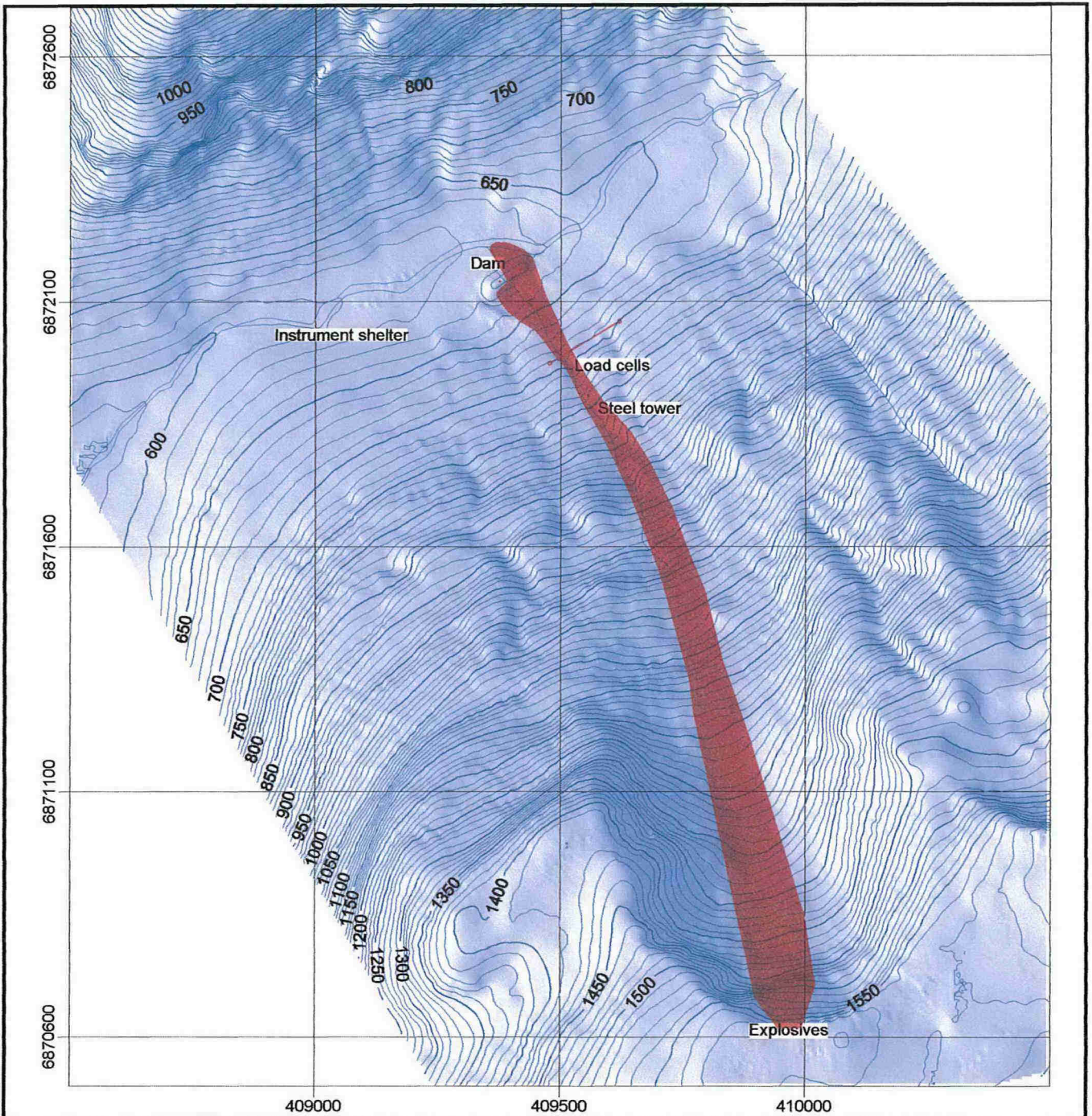
RYGGFONN	Report No. 581200-35	Figure 35
	Drawn by KKr/TG	Date 02-02-26
Detail map of avalanche 19930327	Checked	
	Approved	




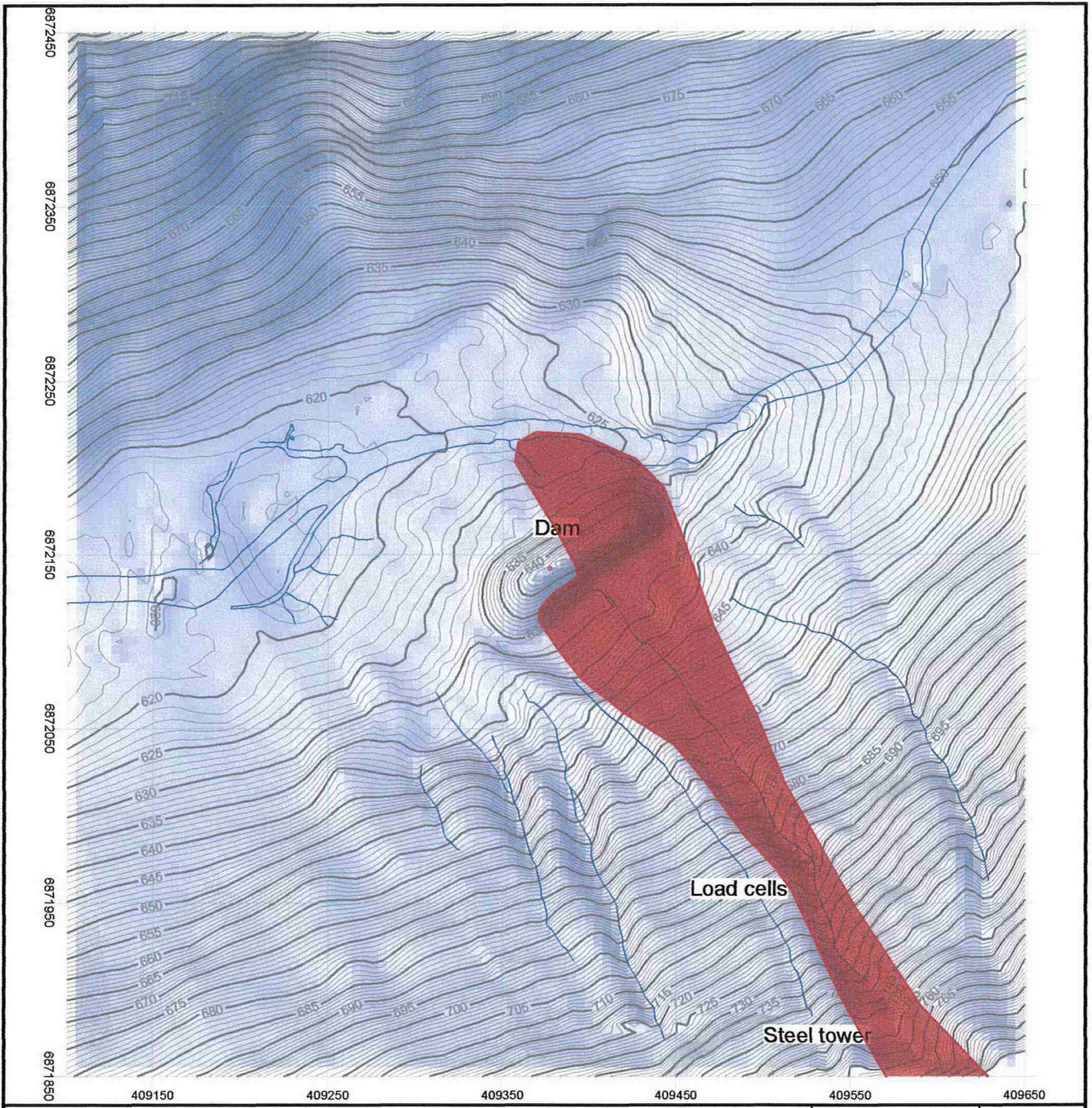
RYGGFONN	Report No. 581200-35	Figure 36
Overview map of avalanche 19940124	Drawn by KKr/TG	Date 02-02-26
	Checked	
	Approved	




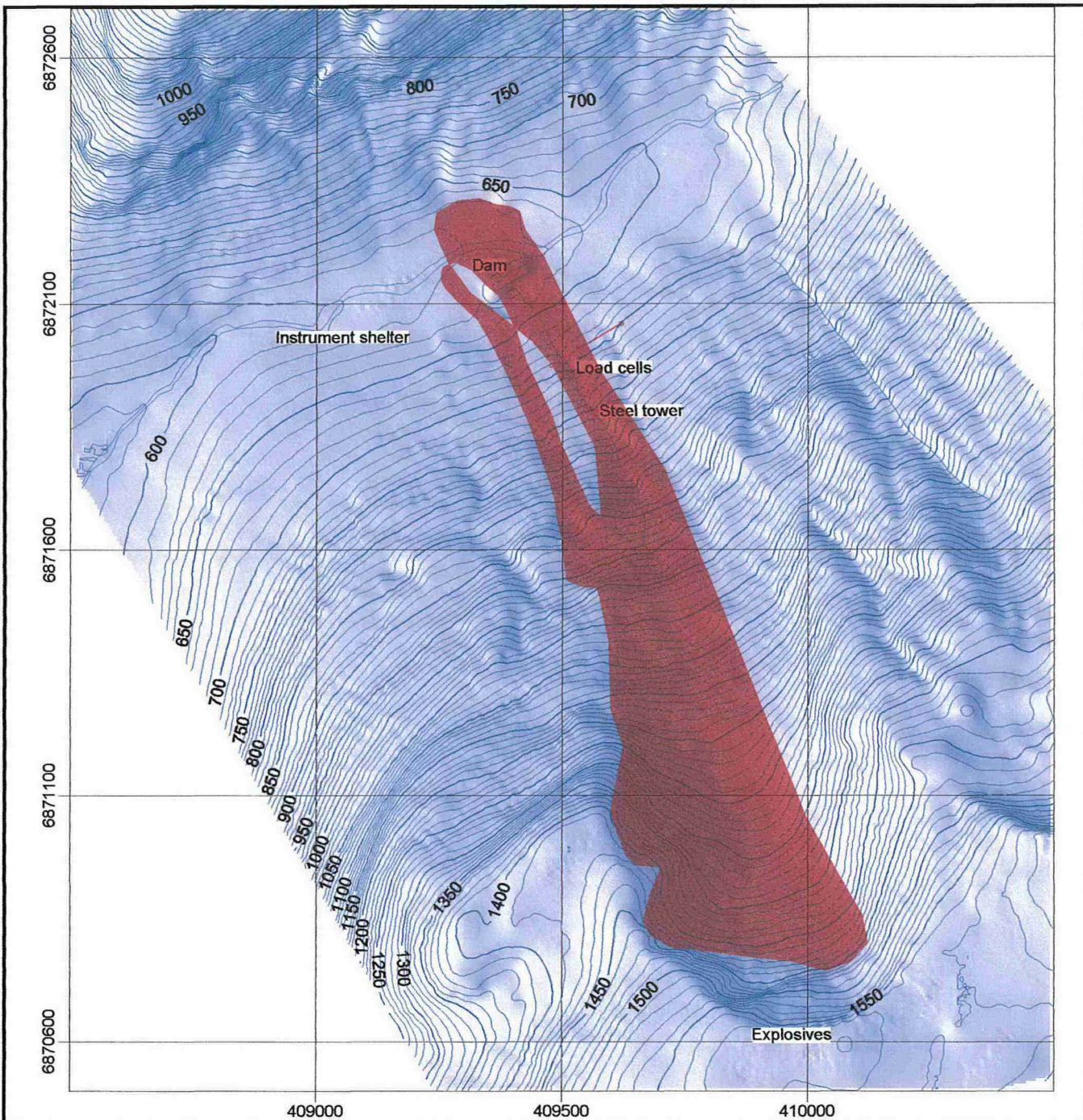
RYGGFONN	Report No. 581200-35	Figure 37
	Drawn by KKr/TG	Date 02-02-26
Detail map of avalanche 19940124	Checked	
	Approved	




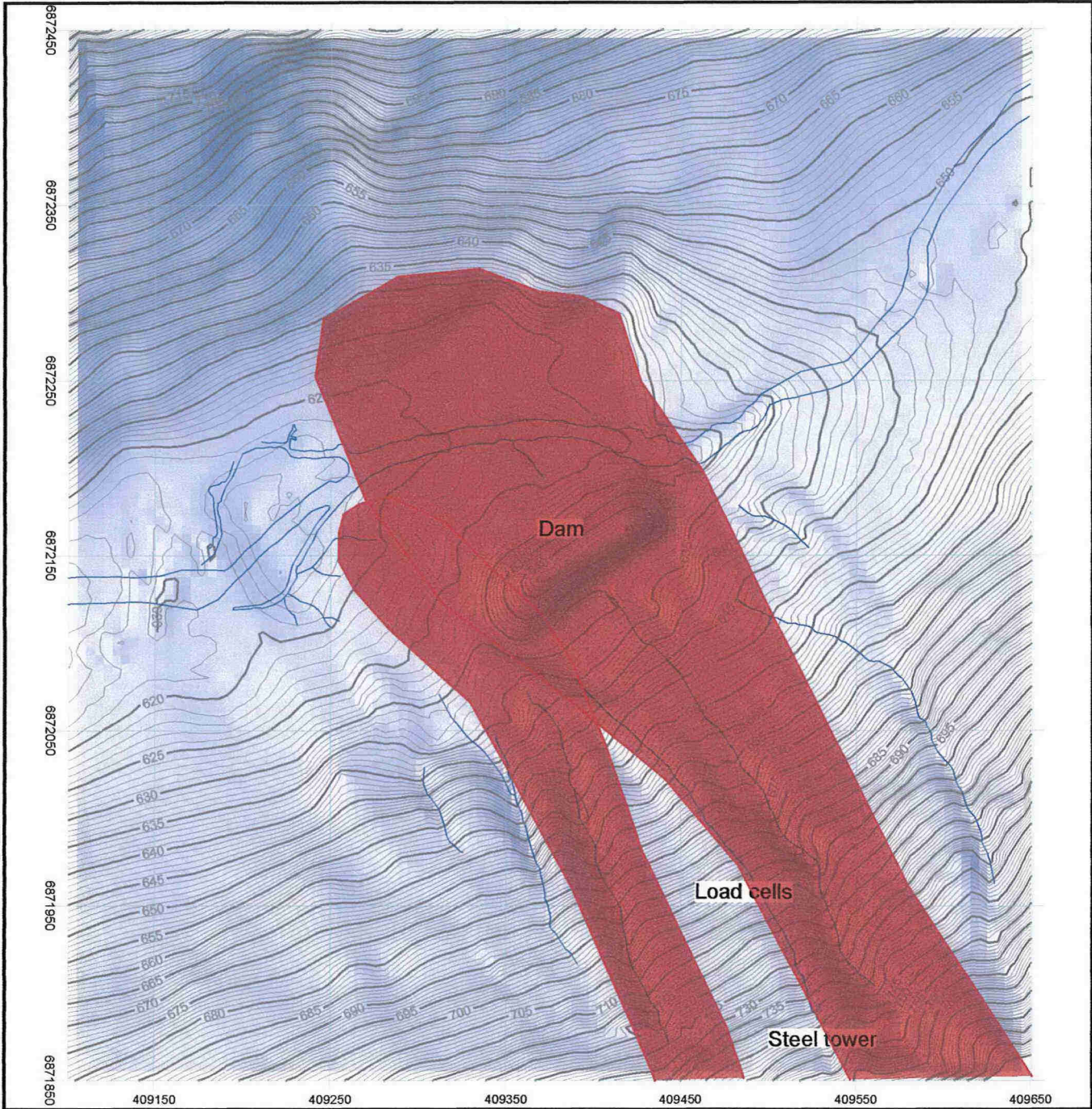
RYGGFONN	Report No. 581200-35	Figure 38
Overview map of avalanche 19950303	Drawn by KKr/TG	Date 02-02-26
	Checked	
	Approved	




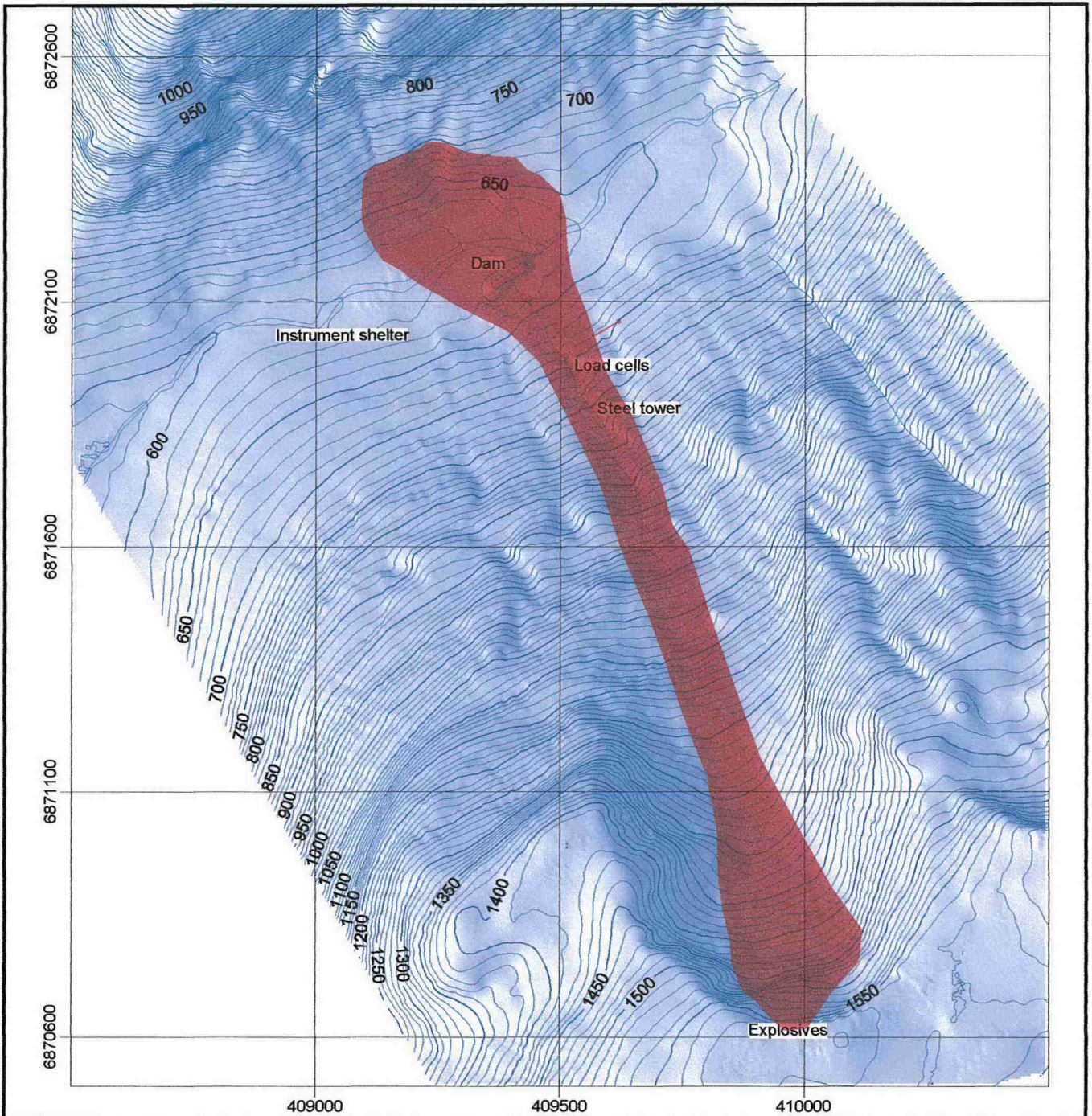
RYGGFONN	Report No. 581200-35	Figure 39
Detail map of avalanche 19950303	Drawn by KKr/TG	Date 02-02-26
	Checked	
	Approved	




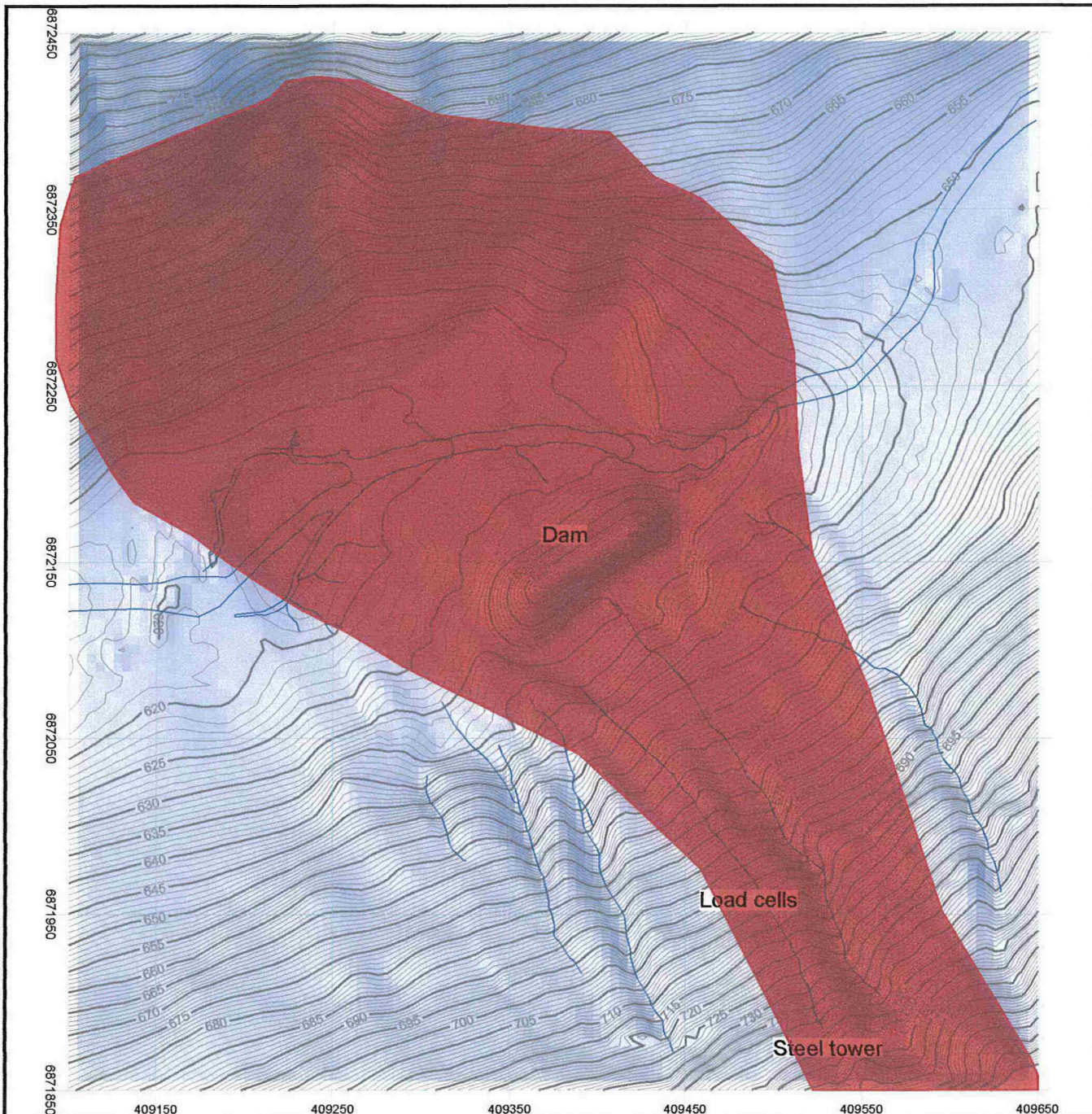
RYGGFONN	Report No. 581200-35	Figure 40
	Drawn by KKr/TG	Date 02-02-26
Overview map of avalanche 19970208	Checked	
	Approved	




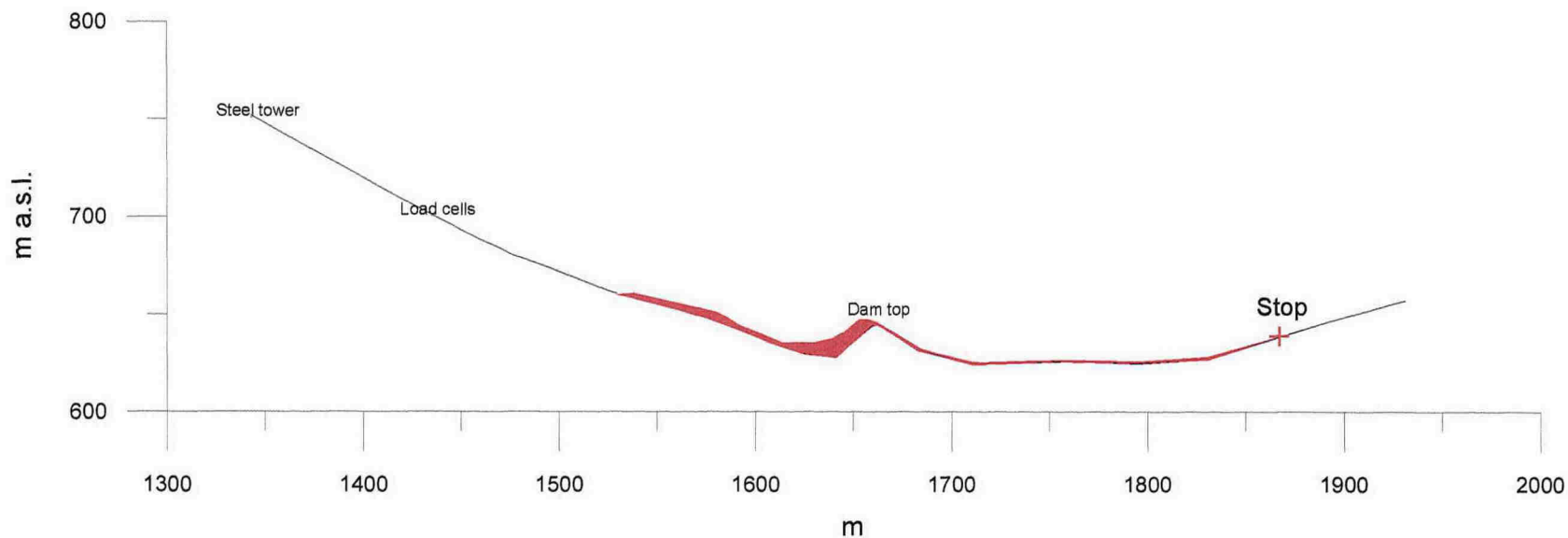
RYGGFONN	Report No. 581200-35	Figure 41
	Drawn by KKr/TG	Date 02-02-26
Detail map of avalanche 19970208	Checked	
	Approved	




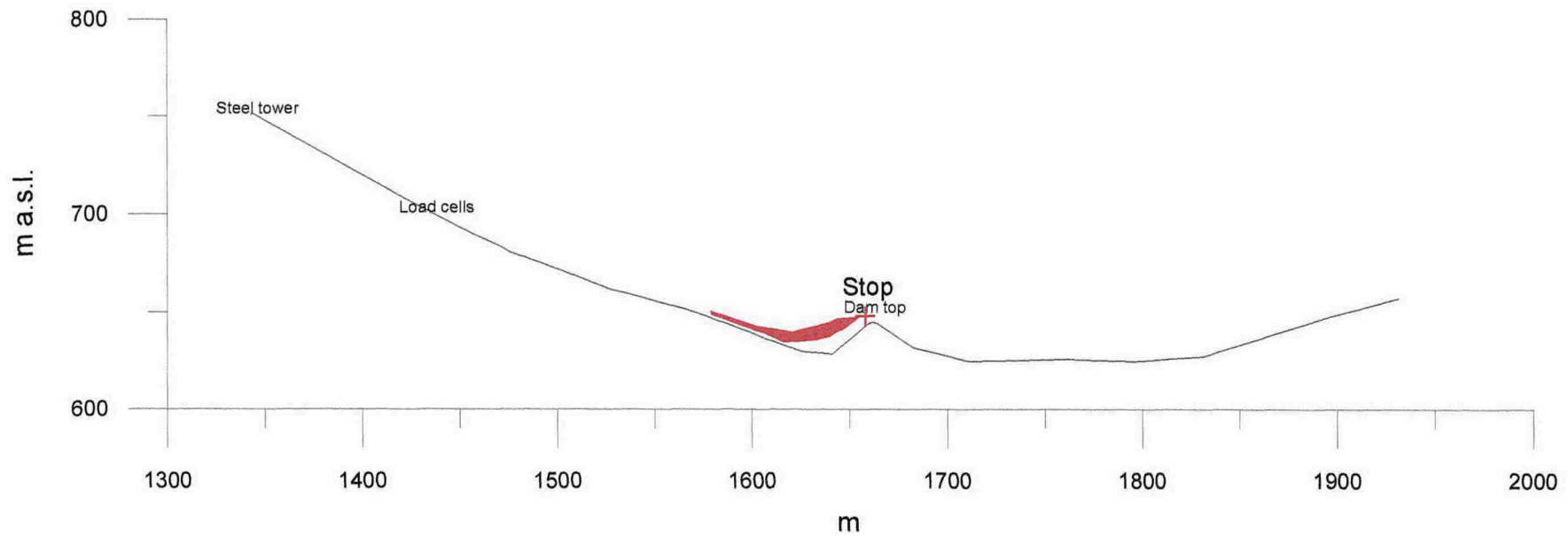
RYGGFONN	Report No. 581200-35	Figure 42
	Drawn by KKr/TG	Date 02-02-26
Overview map of avalanche 20000217	Checked	
	Approved	




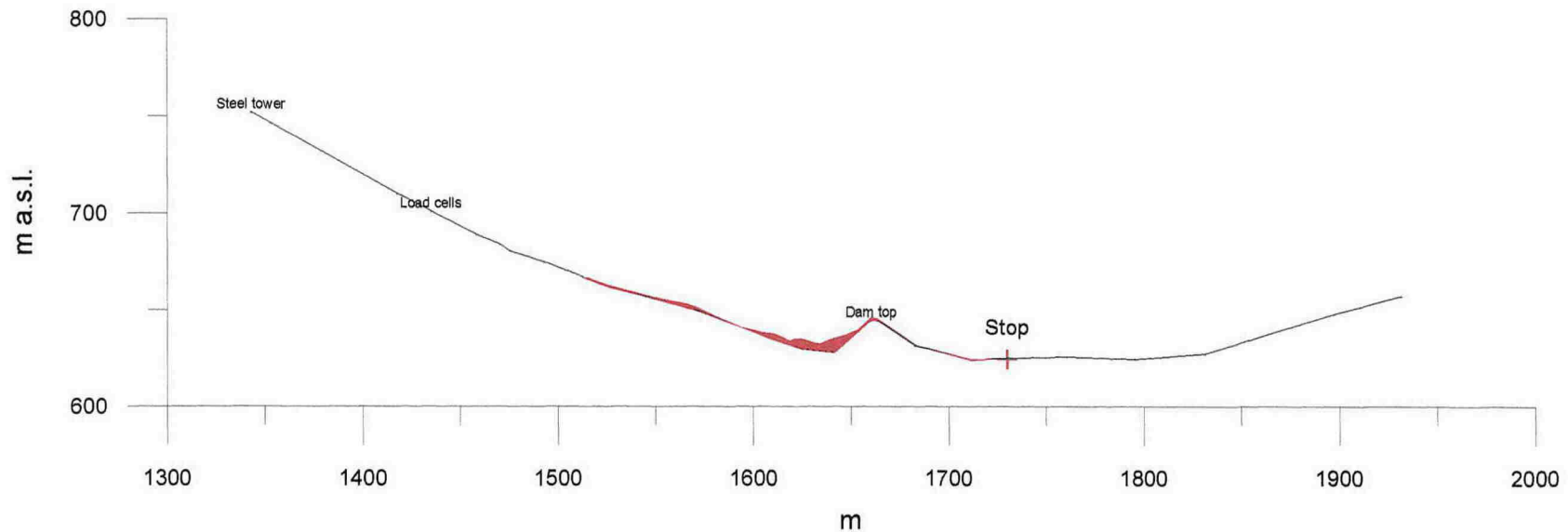
RYGGFONN	Report No. 581200-35	Figure 43
	Drawn by KKr/TG	Date 02-02-26
Detail map of avalanche 20000217	Checked	
	Approved	



RYGGFONN	Report No. 581200-35	Figure 44
19830110 Vertical section of the avalanche deposit.	Drawn by KKr/TG	Date 02-02-26
	Checked	
	Approved	



RYGGFONN	Report No. 581200-35	Figure 45
19830308 Vertical section of the avalanche deposit	Drawn by KKr/TG	Date 02-02-26
	Checked	
	Approved	



RYGGFONN

19850213
Vertical section of the avalanche deposit

Report No.
581200-35

Figure
46

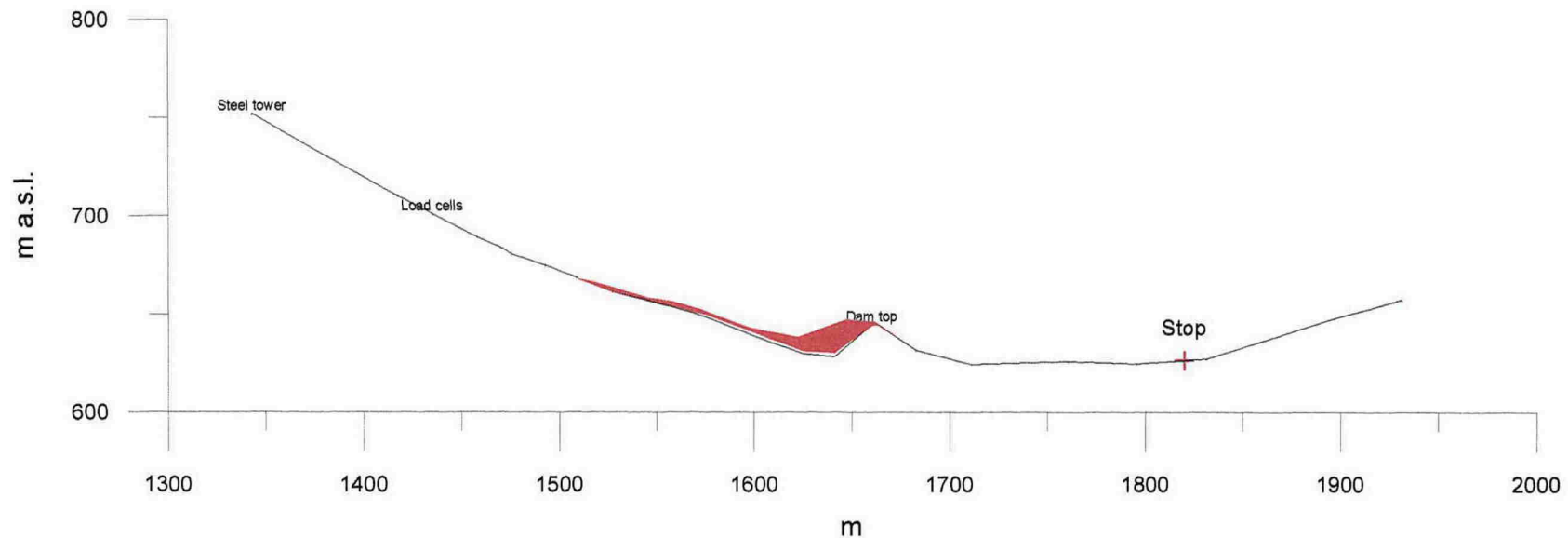
Drawn by
KKr/TG

Date
02-02-26

Checked

Approved





RYGGFONN

19870128
Vertical section of the avalanche deposit

Report No.
581200-35

Figure
47

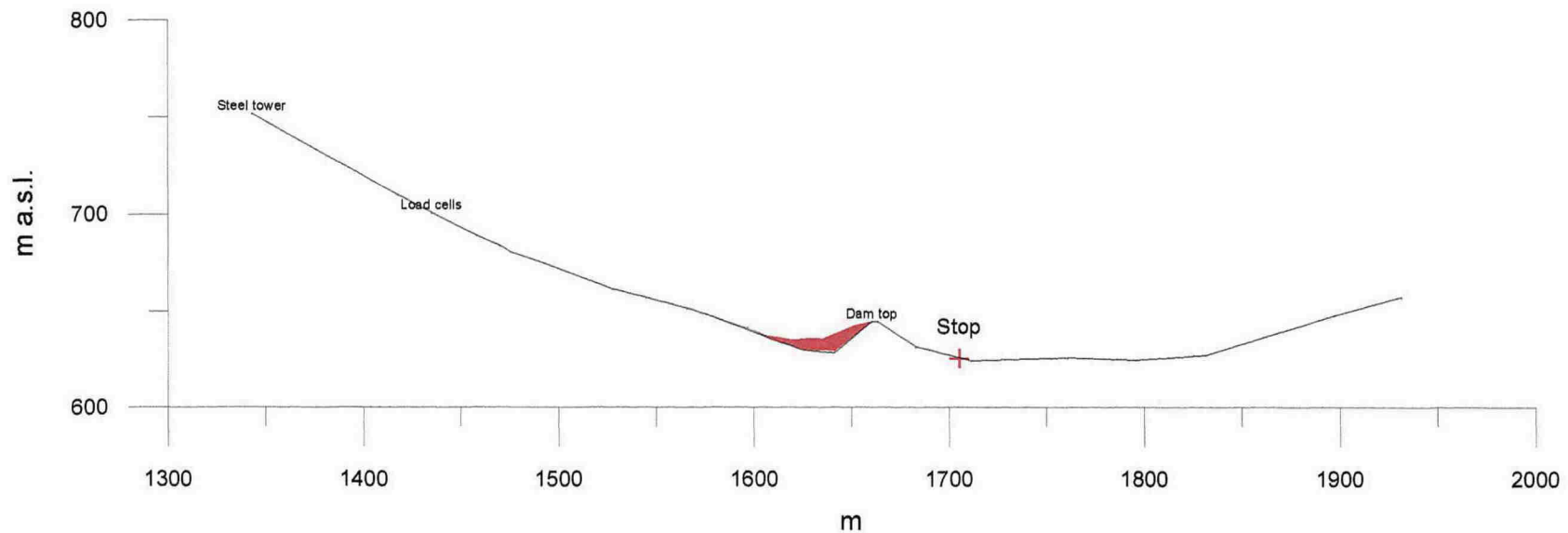
Drawn by
KKr/TG


Date
02-02-26

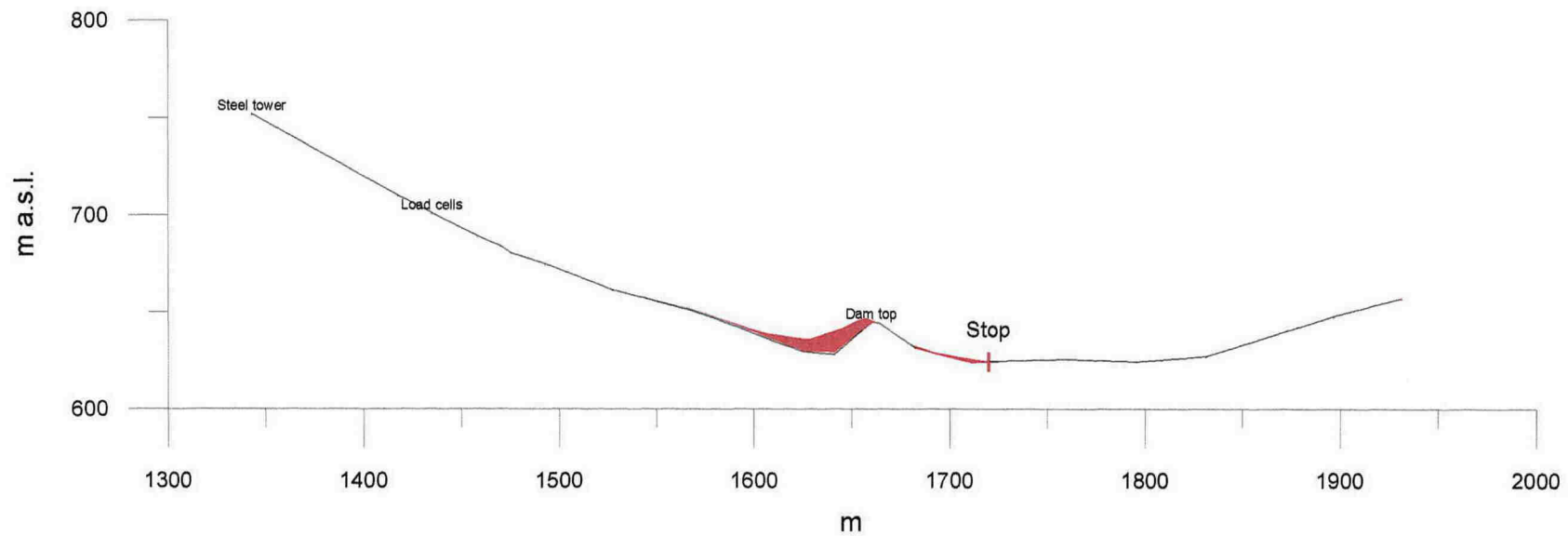
Checked

Approved





RYGGFONN	Report No. 581200-35	Figure 48
19880411 Vertical section of the avalanche deposit	Drawn by KKr/TG	Date 02-02-26
	Checked	
	Approved	



RYGGFONN

19881223
Vertical section of the avalanche deposit

Report No.
581200-35

Figure
49

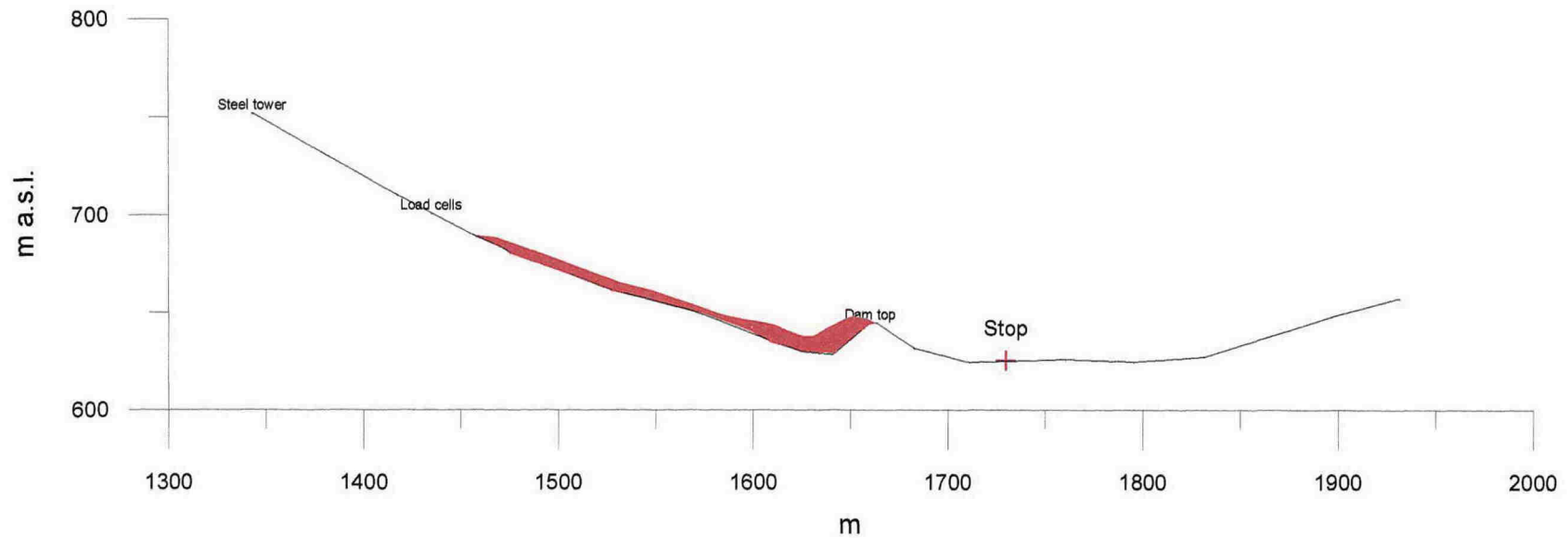
Drawn by
KKr/TG

Date
02-02-26

Checked

Approved





RYGGFONN

19900307
Vertical section of the avalanche deposit

Report No.
581200-35

Figure
50

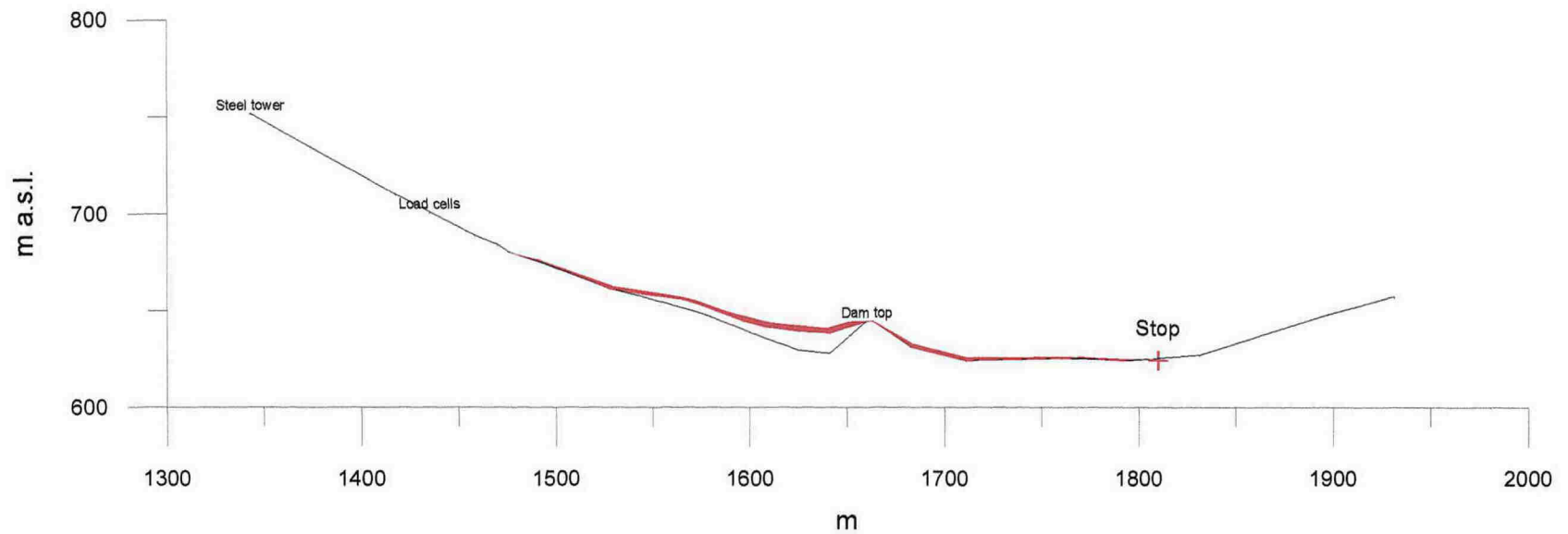
Drawn by
KKr/TG

Date
02-02-26

Checked

Approved





RYGGFONN

19930327
Vertical section of the avalanche deposit

Report No.
581200-35

Figure
51

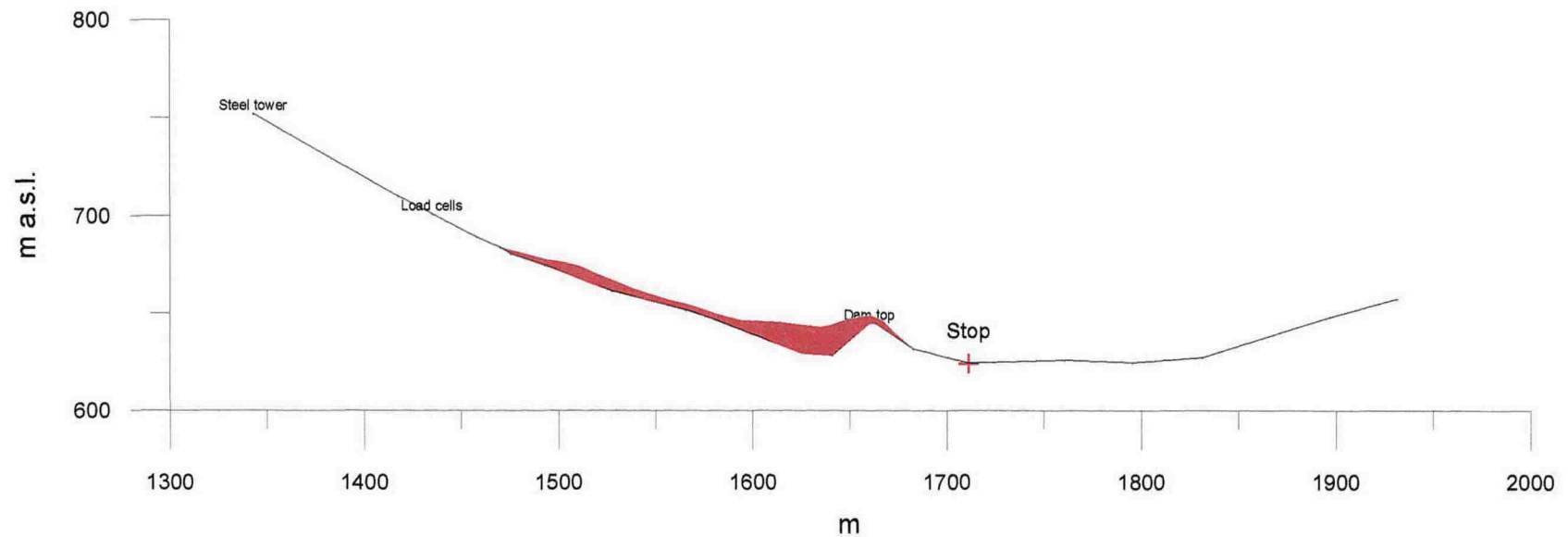
Drawn by
KKr/TG

Date
02-02-26

Checked

Approved





RYGGFONN

19940124
Vertical section of the avalanche deposit

Report No.
581200-35

Figure
52

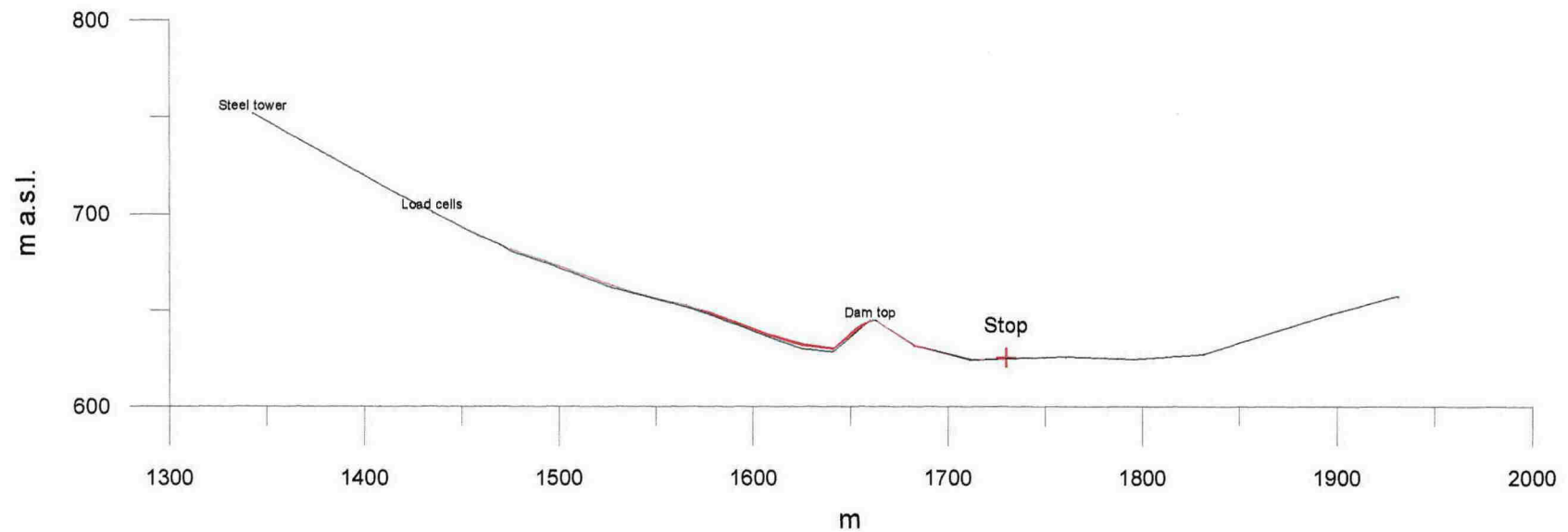
Drawn by
KKr/TG

Date
02-02-26

Checked

Approved





RYGGFONN

19950303
Vertical section of the avalanche deposit

Report No.
581200-35

Figure
53

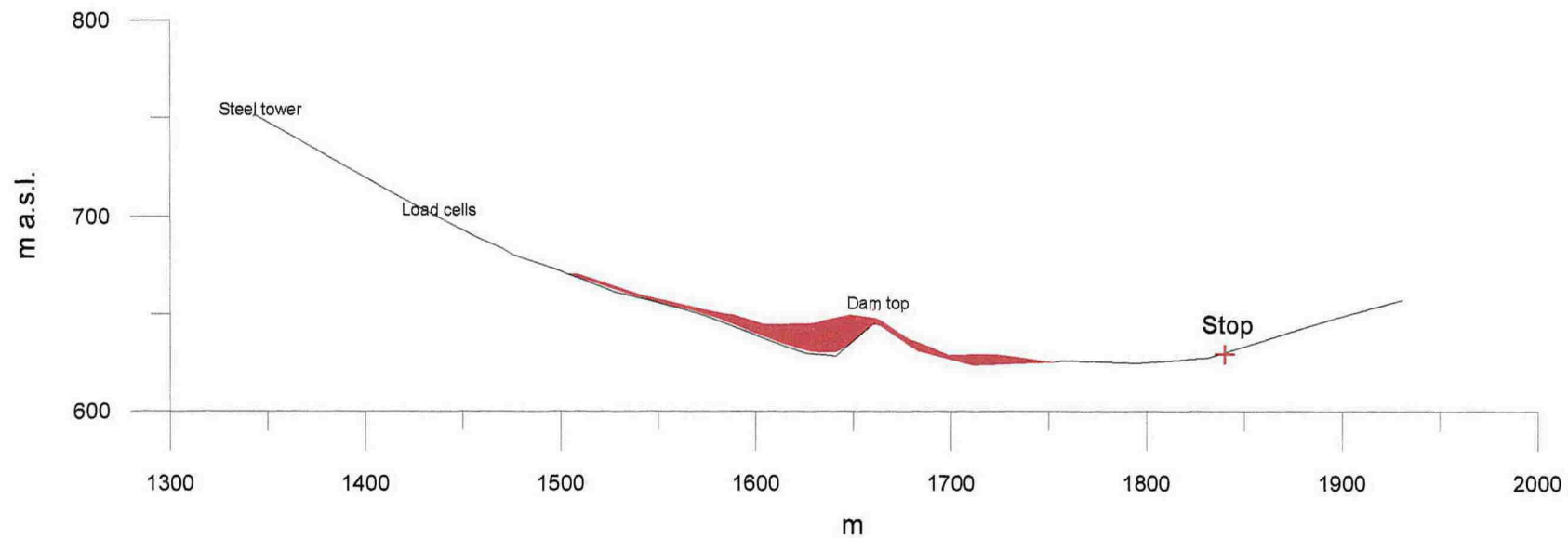
Drawn by
KKr/TG

Date
02-02-26

Checked

Approved





RYGGFONN

Report No.
581200-35

Figure
54

19970208
Vertical section of the avalanche deposit

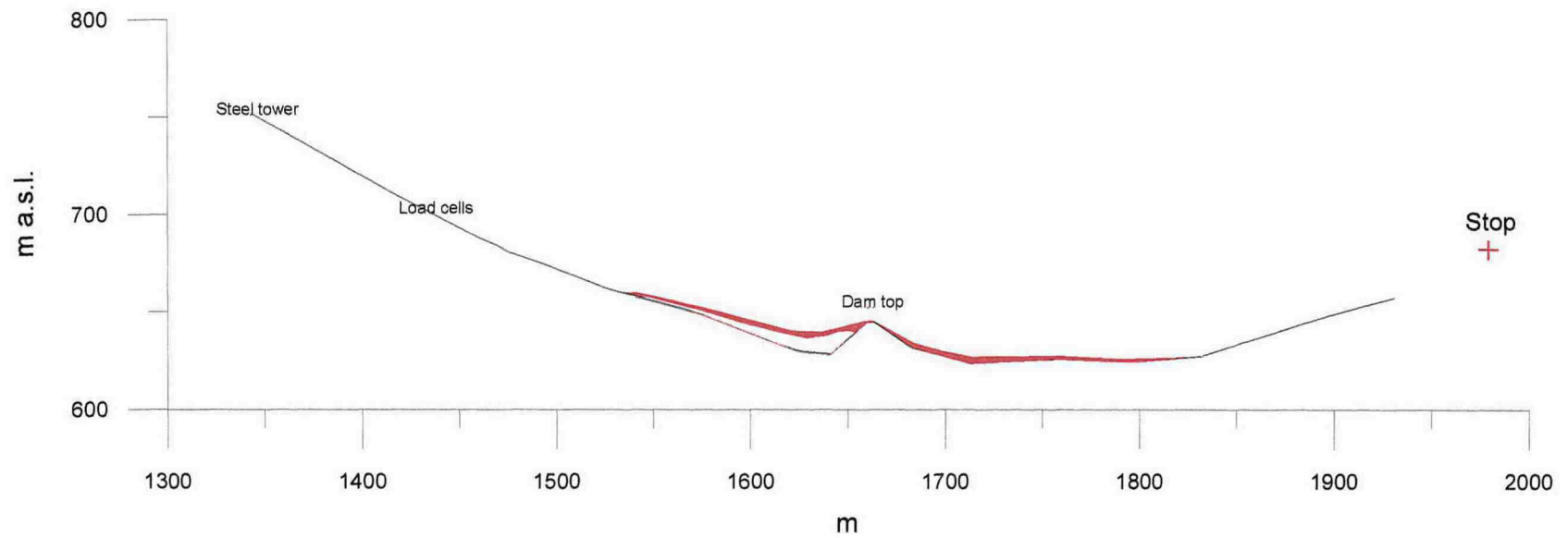
Drawn by
KKr/TG

Date
02-02-26

Checked

Approved





RYGGFONN

Report No.
581200-35

Figure
55

20000217
Vertical section of the avalanche deposit

Drawn by
KKr/TG

Date
02-02-26

Checked

Approved



Kontroll- og referanseside/ Review and reference page



Oppdragsgiver/Client Norwegian Geotechnical Institute	Dokument nr/Document No. 581200-35
Kontraksreferanse/ Contract reference SIP-6	Dato/Date 28 February 2002
Dokumenttittel/Document title Ryggfonn. Full scale avalanche test site and the effect of a catching dam	Distribusjon/Distribution <input checked="" type="checkbox"/> Fri/Unlimited <input type="checkbox"/> Begrenset/Limited <input type="checkbox"/> Ingen/None
Prosjektleder/Project Manager Karstein Lied Utarbeidet av/Prepared by Karstein Lied, Arne Moe, Krister Kristensen, Dieter Issler	
Emneord/Keywords Snow avalanche dynamics, catching dam criteria	
Land, fylke/Country, County Norway Kommune/Municipality Stryn Sted/Location Grasdalen, Ryggfonn Kartblad/Map 1418 IV, Lodalskåpa UTM-koordinater/UTM-coordinates 32VMP094725	Havområde/Offshore area Feltnavn/Field name Sted/Location Felt, blokknr./Field, Block No.

Kvalitetssikring i henhold til/Quality assurance according to NS-EN ISO9001							
Kon- trollert av/ Reviewed by	Kontrolltype/ Type of review	Dokument/Document		Revisjon 1/Revision 1		Revisjon 2/Revision 2	
		Kontrollert/Reviewed		Kontrollert/Reviewed		Kontrollert/Reviewed	
		Dato/Date	Sign.	Dato/Date	Sign.	Dato/Date	Sign.
ArM	Helhetsvurdering/ General Evaluation *	13/3-02	<i>Arne Moe</i>				
ArM	Språk/Style	13/3-02	<i>Arne Moe</i>				
ArM	Teknisk/Technical - Skjønn/Intelligence - Total/Extensive - Tverrfaglig/ Interdisciplinary	13/3-02	<i>Arne Moe</i>				
	Utforming/Layout						
KL	Slutt/Final	13/3-02					
	Kopiering/Copy quality						

* Gjennomlesning av hele rapporten og skjønnsmessig vurdering av innhold og presentasjonsform/
On the basis of an overall evaluation of the report, its technical content and form of presentation

Dokument godkjent for utsendelse/ Document approved for release	Dato/Date <i>13/3-02</i>	Sign. <i>Lied</i>
--	--------------------------	-------------------